



JOHANNES KEPLER
UNIVERSITÄT LINZ

Netzwerk für Forschung, Lehre und Praxis



***Nanomorphology – Efficiency Relationship
in Organic Bulk Heterojunction Plastic Solar Cells***

Dissertation zur Erlangung des akademischen Grades

Doktor rerum naturalium

im Doktoratsstudium der Naturwissenschaften

Angefertigt am Institut für *Physikalische Chemie*

Eingereicht von:

Dipl. Phys. Harald Hoppe

Betreuung:

o. Univ. Prof. Mag. Dr. Niyazi Serdar Sariciftci

Beurteilung:

o. Univ. Prof. Mag. Dr. Niyazi Serdar Sariciftci

ao. Univ. Prof. DI Mag. Dr. Helmut Sitter

Linz, Oktober 2004

Where is the wise man?
Where is the scribe?
Where is the debater of this age?
Has God not made the wisdom of the world foolish?
For since in the wisdom of God
the world by its wisdom did not know God,
God was pleased to save those
who believe by the foolishness of preaching.

1. Corinthians 1: 20-21

Abstract

The relation between the nanoscale morphology and associated device properties in conjugated polymer/fullerene bulk heterojunction “plastic solar cells” is of fundamental interest. To investigate this, complementary measurements on solid state blends of MDMO-PPV (poly-[2-(3,7-dimethyloctyloxy)-5-methyloxy]-para-phenylene-vinylene) and the soluble fullerene C₆₀-derivative PCBM (1-(3-methoxycarbonyl) propyl-1-phenyl [6,6]C₆₁), spin cast from either toluene or chlorobenzene solution, have been performed. The morphological characterization was done with scanning near-field optical microscopy (SNOM), scanning electron microscopy (SEM), transmission electron microscopy (TEM), atomic force microscopy (AFM), and Kelvin probe force microscopy (KPFM), whereas solar cell devices were characterized by means of current-voltage (IV) and spectral photocurrent measurements. In addition the morphology was manipulated via annealing, to provoke further phase separation in the thin film blends and to identify the materials distribution. Photoluminescence measurements indicate a loss mechanism in the coarser phase separated blends and help to identify the demixing of the materials under the thermal treatment. The findings of this study lead to an understanding of the molecular nanomorphology within the solar cell device.

Zusammenfassung

Der Zusammenhang zwischen der Morphologie im Nanometerbereich mit den verbundenen funktionalen Eigenschaften von „Plastiksolarzellen“, welche auf einem im Volumen liegenden konjugierten Polymer/Fullerene Heteroübergang basieren, ist von fundamentalem Interesse. Um dies zu untersuchen, wurden komplementäre Messungen an dünnen Filmen von MDMO-PPV (Poly-[2-(3,7-dimethyloctyloxy)-5-methyloxy]-para-phenylvinyl) mit dem löslichen Fullerene C₆₀-Derivat PCBM (1-(3-methoxycarbonyl) propyl-1-phenyl [6,6]C₆₁) durchgeführt. Diese Filme wurden durch Schleuderbeschichten aus Toluol oder Chlorbenzol Lösungen hergestellt. Zur Untersuchung der Morphologie wurden folgende Meßtechniken herangezogen: rasternde Nahfeldoptikmikroskopie (SNOM), Rasterelektronenmikroskopie (REM), Transmissionselektronenmikroskopie (TEM), Rasterkraftmikroskopie (AFM) und Kelvinsondenkraftmikroskopie (KPFM). Solarzellen wurden mittels von Strom-Spannungskurven und spektralem Photostrom charakterisiert. Des weiteren wurde die Morphologie mittels eines Temperaturschrittes manipuliert, um eine weitere Phasentrennung in den dünnen Mischschichten hervorzurufen und um die Verteilung der Materialien zu ermitteln. Photolumineszenzmessungen deuten auf einen Verlustmechanismus in den gröber phasengetrenten Mischungen hin und bestätigen die Entmischung der Materialien aufgrund der thermischen Behandlung. Die Erkenntnisse aus dieser Arbeit führen zu einem Verständnis der molekularen Nanomorphologie innerhalb der Solarzellen.

Nanomorphology – Efficiency Relationship in Organic Bulk Heterojunction Plastic Solar Cells

1.	Introduction	1
1.1.	Organic Solar Cells	2
1.2.	Materials	5
1.3.	Preparation techniques	8
1.3.1.	Evaporation	9
1.3.2.	Wet Processing	9
1.4.	Basic working principles	10
1.5.	Device architectures	14
1.5.1.	Single layer	14
1.5.2.	Bilayer Heterojunction	15
1.5.3.	Bulk heterojunction	17
1.5.4.	Diffuse Bilayer Heterojunction	18
1.6.	Morphology of Organic Materials	19
1.6.1.	Introduction to Morphology of conjugated Polymer/Fullerene Bulk Heterojunction Solar Cells	23
2.	Experimental	27
2.1.	Materials	27
2.2.	Solar Cell Preparation	28
2.3.	Solar Cell Characterization	29
2.3.1.	Current-Voltage (IV) Measurements	29
2.3.2.	Spectral Photocurrent Measurements	30
2.4.	Morphological Characterization	30
2.4.1.	Atomic Force Microscopy (AFM)	31
2.4.2.	Transmission Electron Microscopy (TEM)	37
2.4.3.	Scanning Electron Microscopy (SEM)	38
2.4.4.	Kelvin Probe Force Microscopy (KPFM)	38
2.4.5.	Scanning Near-Field Optical Microscopy (SNOM)	41
2.5.	Photoluminescence Measurements (PL)	43
3.	Results and Discussion	44
3.1.	Solar Cell Devices	47
3.2.	Nanomorphology	48
3.3.	Identification of Phases	57
3.3.1.	TEM and Electron Diffraction	57
3.3.2.	Annealing of MDMO-PPV:PCBM Blends	59
3.3.3.	Photoluminescence	65
3.3.4.	Percolation and Connectivity	67
4.	Discussion	73
5.	Conclusions	79
6.	References	80
7.	Acknowledgements	96
8.	Appendix	97
8.1.	Curriculum Vitae	97
8.2.	List of Publications	98
8.2.1.	Conference Proceedings	98
8.2.2.	Articles	99

1. Introduction

Photovoltaics deal with the conversion of sunlight into electrical energy. Classic photovoltaic solar cells based on inorganic semiconductors have developed considerably¹ since the first realization of a silicon solar cell in 1954 by Chapin, Fuller and Pearson in the Bell labs.² Today silicon is still the leading technology on the world market of photovoltaic solar cells, with power conversion efficiencies approaching 15 – 20% for mono-crystalline devices. Though the solar energy industry is heavily subsidized throughout many years, the prices of silicon solar cell based power plants or panels are still not competitive with other conventional combustion techniques – except for several niche products. An approach for lowering the manufacturing costs of solar cells is to use organic materials that can be processed under less demanding conditions. Organic photovoltaics has been developed for more than 30 years, however, within the last decade the research field gained considerable in momentum.^{3,4} Organic solar cells can be distinguished by the production technique, the character of the materials and by the device design. The two main production techniques can be distinguished as either wet processing or thermal evaporation. Device architectures are single layer, bilayer heterojunction and bulk heterojunction, with the diffuse bilayer heterojunction as intermediate between the bilayer and the bulk heterojunction. Whereas the single layer comprises of only one active material, the other architectures are based on respectively two kinds of materials: electron donors (D) and electron acceptors (A). The difference of these architectures lays in the charge generation mechanism: single layer devices require generally a Schottky barrier at one contact, which allows to separate photoexcitations in the barrier field. The DA solar cells apply the photoinduced electron transfer⁵ to separate the electron from the hole. The photoinduced electron transfer occurs from the excited state of the donor (lowest unoccupied molecular orbital, LUMO) to the LUMO of the acceptor, which therefore has to be a good electron acceptor with a stronger electron affinity. Subsequent to charge separation both the electron and the hole have to reach the opposite electrodes, the cathode and the anode, respectively. Thus a direct current can be delivered to an outer circuit.

After a rather general introduction, the morphology of solution processed conjugated fullerene/polymer plastic solar cells will be addressed within the scope of this work.

1.1. Organic Solar Cells

Within the past 3 decades there has been a tremendous effort to develop organic photovoltaics,⁶⁻¹⁴ i.e. the conversion of sunlight into electrical energy using organic materials. The field started by the application of small organic molecules (pigments)^{6,7,13,14} and since the development of semiconducting polymers (see e.g.¹⁵⁻¹⁸) these materials were incorporated into organic solar cells resulting in remarkable improvements within the last years.^{8,9,12,19} The potential of semiconducting organic materials to transport electric current and to absorb light in the UV-visible part of the solar spectrum is due to the sp^2 -hybridization of carbon atoms. For example, in conducting polymers the electron in the p_z -orbital of each sp^2 -hybridized carbon atom will form π -bonds with neighboring p_z electrons in a linear chain of sp^2 -hybridized carbon atoms, which leads then to dimerization (an alternating single and double bond structure, i.e. Peierls distortion). Due to the isomeric effect these π -electrons are of a delocalized nature, resulting in high electronic polarizability.

An important difference to inorganic solid-state semiconductors lies in the generally poor (orders of magnitudes lower) charge carrier mobility in these materials,²⁰ which has a large effect on the design and efficiency of organic semiconductor devices. However, organic semiconductors have relatively strong absorption coefficients (usually $\geq 10^5 \text{ cm}^{-1}$), which partly balances low mobilities, giving high absorption in even 100 nm thin devices. Another important difference to crystalline, inorganic semiconductors is the relatively small diffusion length of primary photoexcitations (called excitons) in these rather amorphous and disordered organic materials.^{13,21-29} These excitons are an important intermediate in the solar energy conversion process and usually strong electric fields are required to dissociate them into free charge carriers, which are the desired final products for photovoltaic conversion. This is a consequence of exciton binding energies usually exceeding those of inorganic semiconductors.^{30,31} These features of organic semiconducting materials lead generally to devices with very small layer thicknesses on the order of 100 nm.

Most of the organic semiconductors are hole conductors and have an optical band gap around 2 eV, which is considerably higher than that of silicon and thus limits the harvesting of the solar spectrum to a great extent. Nevertheless, the chemical flexibility for modifications on organic semiconductors via chemical synthesis methods as well as the perspective of low cost, large-scale production drives the research in this field in academia and industry.

The first generation of organic photovoltaic solar cells was based on single organic layers sandwiched between two metal electrodes of different work functions.^{6,7} The rectifying

behavior of single layer devices was attributed to the asymmetry in the electron and hole injection into the molecular π^* and π -orbitals, respectively,³² and to the formation of a Schottky-barrier (e.g.^{7,33-35}) between the p-type (hole conducting) organic layer and the metal with the lower work function. The power conversion efficiencies reported were generally poor (in the range of 10^{-3} - 10^{-2} %), but reached remarkable 0.7% for merocyanine dyes in the early days.^{36,37} In this case, the organic layer was sandwiched between a metal/metal oxide and a metal electrode, thus enhancing the Schottky-barrier effect (metal-insulator-semiconductor (MIS)³⁸ devices). The next breakthrough was achieved by introducing the bilayer heterojunction concept, in which two organic layers with specific electron or hole transporting properties were sandwiched between the electrodes. Tang reported 1986 about 1% power conversion efficiency for two organic materials (a phthalocyanine derivative as p-type semiconductor and a perylene derivative as n-type semiconductor) sandwiched between a transparent conducting oxide and a semitransparent metal electrode.³⁹ This result was for many years the outstanding benchmark and was surmounted only at the turn of the millennium.^{40,41} Hiramoto and coworkers did pioneering work introducing the concept of an organic tandem cell structure by stacking two heterojunction devices.⁴² They also developed a three layer p-i-n like structure with a co-deposited interlayer between the p-type (hole conducting) and n-type (electron conducting) layers.^{43,44} In the mean time the field of conjugated polymers grew mature and first single layer devices based on these newly developed materials were presented.^{35,45-47} But also these polymer single layer devices were showing only power conversion efficiencies of less than 0.1%. The observation of a photoinduced electron transfer from optically excited conjugated polymers to the C_{60} molecule^{5,48} and the observation of highly increased photoconductivities upon C_{60} addition to the conjugated polymers⁴⁹⁻⁵¹ led to the development of polymer-fullerene bilayer heterojunction^{21,52,53} and bulk heterojunction^{54,55} devices incorporating C_{60} and C_{60} -derivatives with enhanced solubility⁵⁶. The photoinduced electron transfer occurs when it is energetically favorable for the electron in the S_1 -excited state of the polymer to be transferred to the much more electronegative C_{60} , thus resulting in an effective quenching of the excitonic photoluminescence of the polymer.⁵ Since the electron is transferred from a p-type hole conducting polymer onto the rather n-type electron conducting C_{60} molecule the notation of donor (D) and acceptor (A) with respect to the electron transfer was introduced. The photoinduced charge transfer is depicted schematically in Fig. 1.1 together with the energetic description.

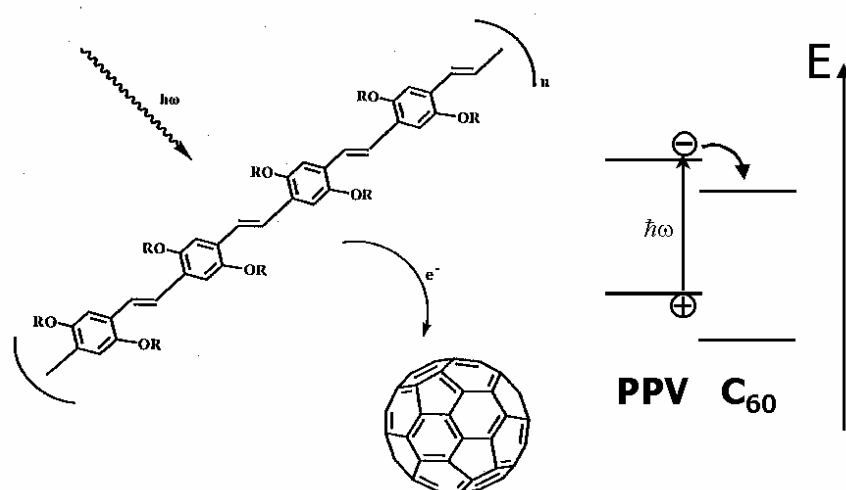


Fig. 1.1: Illustration of the photoinduced charge transfer (left) with a sketch of the energy level scheme (right). After excitation in the PPV polymer the electron is transferred to the C₆₀ due to its higher electron affinity.

The bulk heterojunction concept, similar to the co-evaporated molecular structures of Hiramoto,^{43,44} was introduced by blending two polymers having donor (D) and acceptor (A) properties in solution.⁵⁷⁻⁵⁹ Spin cast films from such binary solutions then resulted in solid-state mixtures of both polymers. A further approach was lamination of two polymer layers, leading to a diffusive interface between D and A moieties, and calculated power conversion efficiencies approaching 2% were reported.⁶⁰

The organic solar cell development gained momentum in the last years: Conversion efficiencies between 1.5 and 4% have been achieved for evaporated bilayer devices,^{61,62} bulk heterojunction polymer-fullerene devices,⁶³⁻⁷⁰ co-evaporated molecular devices^{14,71-73} and in organic-inorganic hybrid devices.⁷⁴⁻⁷⁶

Conceptually similar to the bulk heterojunction, there is a wide research field of dye sensitized, electrochemical solar cells. The early steps in the development⁷⁷⁻⁸² were largely improved by the Graetzel group.⁸³ To review this field of electrochemical photovoltaic cells the interested reader is advised to the literature in this research area (e.g.⁸⁴⁻⁸⁶). However, in the recent years, by the introduction of organic hole conductors^{24,74,75,87-94} as replacement for the liquid electrolytes in electrochemical solar cells and by the exchange of the electron conducting acceptor materials in organic heterojunction devices with inorganic

nanocrystals,^{76,95-100} electrochemical and organic photovoltaic research directions are gradually merging together.

For practical application not only the power conversion efficiency but also the lifetime of the photovoltaic device is of importance. The stability of organic solar cells is mainly affected by photodegradation of the active materials.^{64,101,102} However, encapsulation techniques as applied in organic LED's can provide an efficient sealing against oxidizing agents, but still a high intrinsic photostability of the organic materials is required.

In the next section, commonly used materials are briefly introduced, followed by a section discussing the main preparation techniques for organic solar cell devices. Thereafter, basic operation principles of photovoltaic light conversion are reviewed, followed by a section presenting the different types of devices. Finally, a section on morphology effects will introduce to the conceptual formulation of this work.

1.2. Materials

Plants use the natural process of photosynthesis to convert sunlight into chemical energy, where the first step in this process is the absorption of light by the chlorophyll molecule. Interestingly chlorophyll pigments were also directly applied in a single layer solar cell.¹⁰³ Besides the absorption of sunlight and (subsequent) creation of photogenerated charge carriers, a second requirement for solar cell materials is the ability to transport these charge carriers. Both properties are commonly found for materials that have an extended delocalized π -electron system. Phthalocyanine is a representative of the p-type, hole-conducting materials that work as electron donor. The perylene and its derivatives show an n-type, electron-conducting behavior and they serve as electron acceptor material. Both of these molecules were often incorporated into evaporated solar cells. Since the optical band-gap of most organic materials is around 2 eV, the thermally excited, intrinsic charge carrier concentrations are rather low. Due to disorder and limited overlap of electronic wavefunctions (van-der-Waals interactions) also the charge carrier mobilities of organic materials are relatively small and hence they can nearly be regarded as insulators. However, there are possibilities to increase the charge carrier concentration, mostly done via molecular or electrochemical doping. Donor type materials show a doping effect, when exposed to oxygen or other strong oxidizing agents such as iodine.^{6,7,104} This doping is achieved by transferring an electron from the ground state S_0 of the organic semiconductor to the oxidizing agent, resulting in

increased charge carrier concentrations in the hole conductor. As an example for n-type doping, perylene was doped upon exposition to hydrogen.¹⁰⁴ Due to these doping effects the formerly rather insulating materials possess free charge carriers and bilayer devices can work like classical p-n junctions.^{105,106} However, doping with gases is not very well controllable. A more controlled approach of doping is achieved by the co-evaporation of both materials, matrix and dopant.^{14,107-109} Among others the buckminster fullerene C₆₀ (and derivatives) is a strong electron acceptor.¹¹⁰ Blended with hole-conducting materials it does not improve charge transport in the dark, but leads to a large increase in photoconductivity under illumination.⁴⁹⁻⁵¹ This is a result of the photoinduced charge transfer,⁵ and hence this process can be viewed as “photodoping”.¹¹¹ The chemical structures of some molecular materials are depicted in Fig. 1.2.1 (ZnPc (Zinc-phthalocyanine), MePtcdi (perylene-3,4,9,10, tetracarboxylic-N,N'-dimethyl-diimide) and C₆₀).

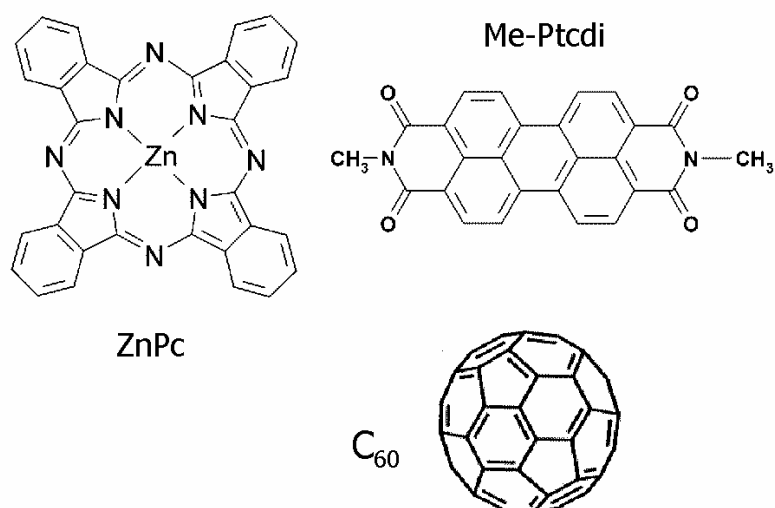


Fig. 1.2.1: Some organic molecules commonly applied in evaporated organic solar cells: ZnPc (Zinc-phthalocyanine), Me-Ptcdi (perylene-3,4,9,10, tetracarboxylic-N,N'-dimethyl-diimide) and the buckminster fullerene C₆₀.

In Fig. 1.2.2 some commonly used conjugated polymers are shown. Three important representatives of hole-conducting donor type polymers are MDMO-PPV (poly[2-methoxy-5-(3,7-dimethyloctyloxy)]-1,4-phenylenevinylene), P3HT (poly(3-hexylthiophene-2,5-diyl)) and PFB (poly(9,9'-dioctylfluorene-co-bis-N,N'-(4-butylphenyl)-bis-N,N'-phenyl-1,4-phenylenediamine)). They are shown together with electron-conducting acceptor polymers like

CN-MEH-PPV (poly-[2-methoxy-5-(2'-ethylhexyloxy)-1,4-(1-cyanovinylene)-phenylene] and F8TB (poly(9,9'-dioctylfluorene-co-benzothiadiazole), and a soluble derivative of C₆₀, namely PCBM (1-(3-methoxycarbonyl) propyl-1-phenyl[6,6]C₆₁). All of these materials are solution processible due to their side chain solubilization and the polymers show photo- and electroluminescence.¹¹²⁻¹¹⁴ For the construction of donor-acceptor solar cells, the donor polymers can be either combined with an acceptor polymer or with fullerenes either in planar or diffuse bilayer structures or in blends (compare section 4).

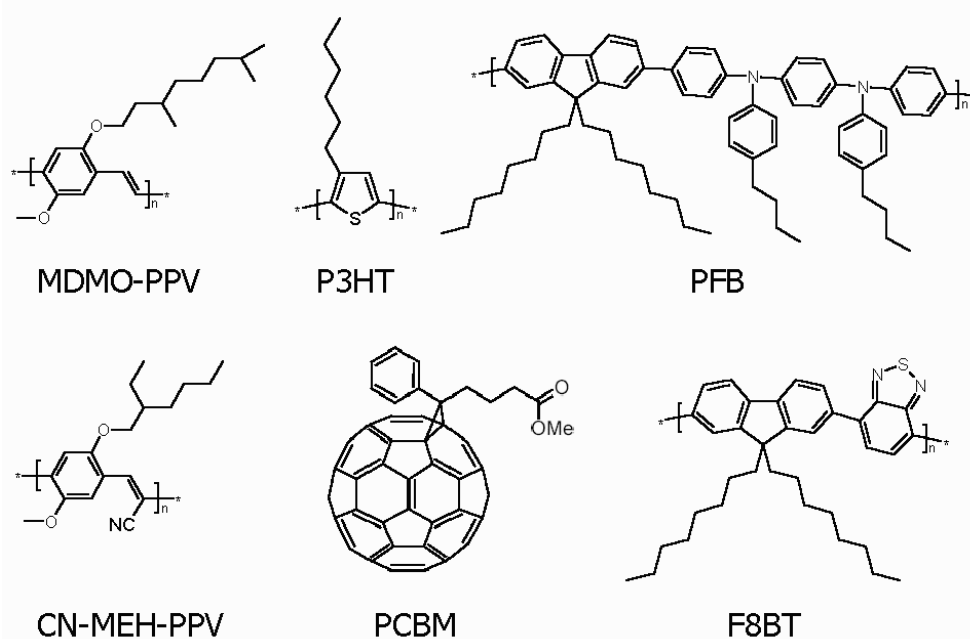


Fig. 1.2.2: Several solution processible conjugated polymers and a fullerene derivative used in organic solar cells. Upper row: the p-type hole-conducting donor polymers MDMO-PPV (poly[2-methoxy-5-(3,7-dimethyloctyloxy)]-1,4-phenylenevinylene), P3HT (poly(3-hexylthiophene-2,5-diyl) and PFB (poly(9,9'-dioctylfluorene-co-bis-*N,N'*-(4-butylphenyl)-bis-*N,N'*-phenyl-1,4-phenylenediamine). Lower row: the electron-conducting acceptor polymers CN-MEH-PPV (poly-[2-methoxy-5-(2'-ethylhexyloxy)-1,4-(1-cyanovinylene)-phenylene] and F8TB (poly(9,9'-dioctylfluorene-co-benzothiadiazole), and a soluble derivative of C₆₀, PCBM (1-(3-methoxycarbonyl) propyl-1-phenyl[6,6]C₆₁).

To display the fraction of the sunlight, which can contribute to energy conversion in these materials, absorption coefficients of films of some materials are shown in comparison with the AM 1.5 solar spectrum in Fig. 1.2.3. While the silicon absorption spectrum extends up to 1100 nm, the organic materials use only the blue side of the solar spectrum.

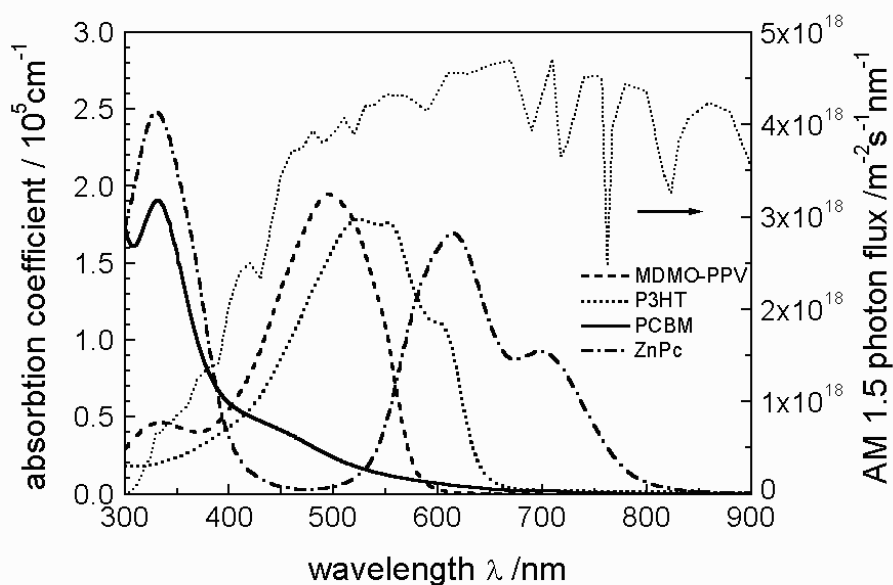


Fig. 1.2.3: Absorption coefficients of films of commonly used materials are depicted in comparison with the standard AM 1.5 terrestrial solar spectrum. The overlap is generally small.

Charge carrier mobilities in films of molecules and conjugated polymers often depend on the nanoscopic order, which can be manipulated by the preparation conditions.¹¹⁵⁻¹¹⁹ For example, a preferential orientation of polymer backbones parallel to the substrate^{120,121} gives rise to an anisotropic charge transport.^{118,119} An overview on some materials used for organic field effect transistors (FET's) is reported by Dimitrakopoulos.²⁰ However, charge transport in FETs is in lateral direction (parallel to the substrate) contrary to solar cells and most LEDs. For bulk heterojunction solar cells it was observed that the charge transport in such blend structures is a sensitive function of the nanomorphology of the mixture.¹²²⁻¹²⁵

1.3. Preparation techniques

The two most common techniques for thin film production are in a way complementary for the choice of materials. While for evaporation thermal stability is required, materials for solution processing need to be soluble. Small molecules may be thermally more stable but less soluble than polymers, where solubility often is achieved by side-chain-solubilization. Polymers will decompose under excessive heat and have a too large molar mass for

evaporation. Hence for small molecules evaporation is the best choice, while semiconducting polymers are mainly processed from solution. However, less soluble molecules like C₆₀ may become soluble when modified by attaching solubilizing groups (e.g. PCBM) and short polymers or oligomers may also be evaporated.^{71,126}

1.3.1. Evaporation

To grow films by thermal evaporation, usually a vacuum of $<10^{-5}$ mbar is applied. Thus the mean free path of the evaporated molecule is longer than the distance between the evaporation source and the sample holder. In addition, contaminants like oxygen and water are reduced and can be eliminated further by ultra high vacuum (UHV, $<10^{-9}$ mbar) or evaporation inside of a glove box with inert atmosphere. To create interpenetrating donor-acceptor networks or to achieve molecular doping, co-evaporation techniques can be applied.^{14,43,71,107,127}

1.3.2. Wet Processing

Common to all wet processing techniques is the solving of organic materials in an appropriate solvent like water or any other polar or non-polar organic solvent. A special case is the solution processing of a soluble monomer coupled with a polymerization reaction during (for example electrochemical polymerization) or after (e.g. via heat treatment, UV curing etc.) the film forming process (precursor route). This has the advantage, that after preparation the resulting polymers are insoluble and another film can be deposited from solution on top of them. If polymers or polymer/polymer or polymer/molecule blends are directly processed from solution, several common techniques are applied: a.) spin coating, b.) doctor blading, c.) screen-printing, d.) inkjet printing and many more. For example screen-printing was applied to a MDMO-PPV:PCBM blend (Fig. 1.3.2.1).¹²⁸ This exploitation of existing printing techniques assures an easy upscaling of the production and low energy consumption during production of solar cells, which is important for the energy amortization (energy delivered by a solar cell during its lifetime as compared to the energy needed to produce the solar cell itself).

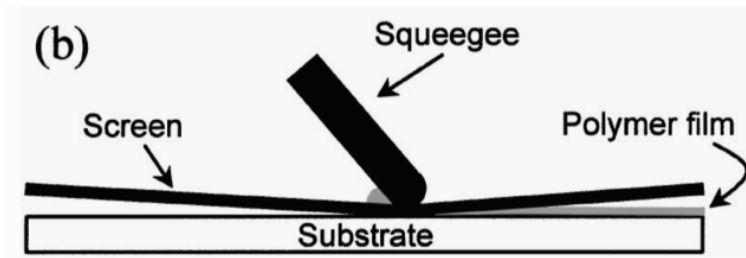


Fig. 1.3.2.1: Schematic of the screen-printing of a polymer/fullerene based organic solar cell. Reprinted from¹²⁸, Copyright 2001, American Institute of Physics.

1.4. Basic working principles

The process of converting light into electric current in an organic photovoltaic cell is accomplished by four consecutive steps:

- 1.) Absorption of a photon leading to the formation of an excited state, the electron-hole pair (exciton).
- 2.) Exciton diffusion to a region, where
- 3.) the charge separation occurs.
- 4.) Finally the charge transport to the anode (holes) and cathode (electrons), in order to supply a direct current for the consumer load.

The potential energy stored within one pair of separated positive and negative charges is equivalent to the difference in their respective quasi-Fermi levels, or in other words it corresponds to the difference in the electrochemical potentials.³¹ The larger the quasi-Fermi level splitting remains during charge transport through the interfaces at the contacts, the larger will be the photovoltage. While for ideal (ohmic) contacts no loss is expected, energy level offsets or band bending at non-ideal contacts (that undergo energy-level-alignments due to Fermi-level differences) can lead to a decrease in the photovoltage.

The electric current that a photovoltaic solar cell delivers corresponds to the number of created charges that are collected at the electrodes. This number depends on the fraction of photons absorbed (η_{abs}), the fraction of electron-hole pairs that are dissociated (η_{diss}) and finally the fraction of (separated) charges that reach the electrodes (η_{out}) determining the overall photocurrent efficiency (η_j):

$$\eta_j = \eta_{\text{abs}} * \eta_{\text{diss}} * \eta_{\text{out}}$$

The fraction of absorbed photons is a function of the absorption spectrum, the absorption coefficient, the absorbing layer thickness and of internal multiple reflections at e.g. metallic electrodes. The fraction of dissociated electron-hole pairs on the other hand is determined by

whether they diffuse into a region where charge separation occurs and on the charge separation probability there.¹²⁹

In order to reach the electrodes, the charge carriers need a net driving force, which generally results from a gradient in the electrochemical potentials of electrons and holes. Two “forces” contribute to this: internal electric fields and concentration gradients of the respective charge carrier species. The first leads to a field induced drift and the other to a diffusion current. Though a detailed analysis requires the knowledge of charge carrier distributions over film depth, thin film devices (~ 100 nm) are mostly field drift dominated whereas thick devices, having effective screening of the electrical fields inside the bulk, are more dominated by the diffusion of charge carriers in concentration gradients at the selective contacts.

To understand the rectifying behavior of an intrinsic (non-doped) semiconductor device in the dark, the MIM (metal-insulator-metal) model³⁸ is useful. In Fig. 1.4.1, a semiconductor, sandwiched between two metal electrodes with different work functions, is depicted for several situations. The metals are represented by their Fermi levels, while for the semiconductor the valence and conduction bands, corresponding to the molecular LUMO (Lowest Unoccupied Molecular Orbital) and the HOMO (Highest Occupied Molecular Orbital) levels, are shown.

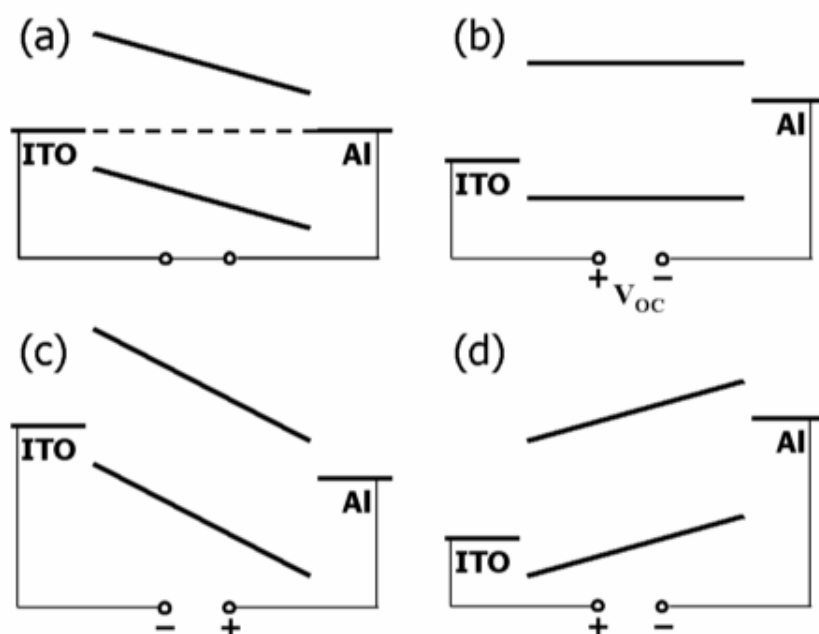


Fig. 1.4.1: Metal-insulator-metal (MIM) picture of organic diode device function. (a) closed circuit condition: under illumination photogenerated charges drift towards the contacts. (b) flat band or open circuit condition: the current becomes zero. (c) reversed bias: photogenerated charges drift in strong electric fields, the diode operates as a photodetector. (d) forward bias larger than V_{oc} : the injection increases and the diode opens up.

In Fig. 1.4.1(a) there is no voltage applied, i.e. short circuit conditions. Hence there is no net current flowing in the dark and the built-in electric field resulting from the difference in the metals' work functions is evenly distributed throughout the device. Under illumination, separated charge carriers can drift in this electric field to the respective contacts: the electrons move to the lower work function metal and the holes to the opposite. The device then works as a solar cell. In Fig 1.4.1 (b) the situation is shown for open circuit conditions, also known as “flat band condition”. The applied voltage is called the open circuit voltage V_{OC} , which corresponds in this case to the difference in the metals' work functions and balances the built-in field. As there is no net driving force for the charge carriers, the current is zero. In Fig. 1.4.1 (c) the situation is shown for an applied reverse bias and only a very small injected dark current j_0 can flow. Under illumination, the generated charge carriers drift under strong electric fields to the respective electrodes and the diode works as a photodetector. If a forward bias larger than the open circuit voltage is applied (Fig. 1.4.1 (d)), the contacts can efficiently inject charges into the semiconductor. If these can recombine radiatively, the device works as a light emitting diode (LED). The asymmetric diode behavior results basically from the different injection of the two metals into the HOMO and LUMO levels, respectively, which depends exponentially on the energy barrier between them.³²

In Fig. 1.4.2 the current-voltage characteristics are shown for a solar cell in the dark and under illumination. In the dark, there is almost no current flowing, until the contacts start to inject heavily at forward bias for voltages larger than the open circuit voltage. Under illumination, the current flows in the opposite direction than the injected currents. At (a) the maximum generated photocurrent flows under short circuit conditions, at (b) the photogenerated current is balanced to zero (flat band condition). Between (a) and (b), in the fourth quadrant, the device generates power, i.e. current \times voltage. At a certain point, denoted as Maximum Power Point (MPP), the product between current and voltage and hence the power output is largest.

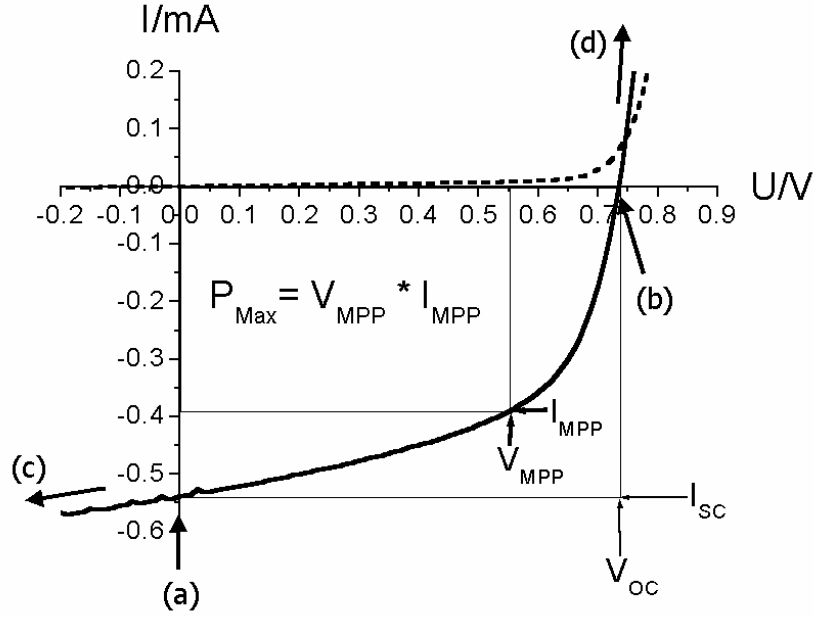


Fig. 1.4.2: Current-voltage (IV) curves of an organic solar cell (dark: dashed, illuminated: full line). The characteristic intersections with the abscissa and the ordinate are the open circuit voltage (V_{OC}) and the short circuit current (I_{SC}), respectively. The largest power output (P_{Max}) is determined by the point where the product of voltage and current is maximized. Division of P_{Max} by the product of I_{SC} and V_{OC} yields the fill factor FF. The letters (a-d) correspond to Fig. 1.4.1.

To determine the efficiency of a solar cell, this power needs to be compared with the incident light intensity. Generally the fill factor is calculated as $FF = V_{MPP} \cdot I_{MPP} / (V_{OC} \cdot I_{SC})$ to denote the part of the product of V_{OC} and I_{SC} , that can be used. With this, the power conversion efficiency can be written as:

$$\eta_{POWER} = \frac{P_{OUT}}{P_{IN}} = \frac{I_{MPP} \cdot V_{MPP}}{P_{IN}} = \frac{FF \cdot I_{SC} \cdot V_{OC}}{P_{IN}} \quad (1)$$

Generally the I-V characteristics of a photovoltaic device can be described by:

$$I = I_0 \cdot \left\{ \exp\left(\frac{e}{nkT}(U - IR_S)\right) - 1 \right\} + \frac{U - IR_S}{R_{SH}} - I_{PH} \quad (2)$$

where I_0 is the dark current, e the elementary charge, n the diode ideality factor, U the applied voltage, R_S the series and R_{SH} the shunt resistance and I_{PH} is the photocurrent. The

corresponding equivalent circuit is depicted in Fig. 1.4.3. For a high FF two things are required: a.) that the shunt resistance is very large in order to prevent leakage currents and b.) that the series resistance is very low in order to get a sharp rise in the forward current. The series resistance simply adds up from all series resistance contributions in the device, i.e. from bulk transport, from interface transfer and from transport through the contacts.

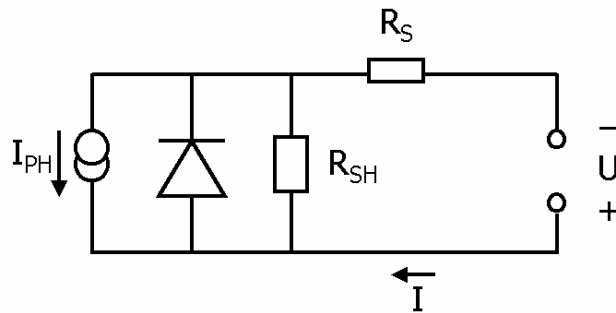


Fig. 1.4.3: Equivalent circuit for a solar cell, described by equation (2).

1.5. Device architectures

As the exciton binding energy in organic semiconductors is generally large (0.1– 1eV) compared to silicon,^{30,31,130} the built in electric fields (on the order of $10^6 - 10^7$ V/m) are usually not high enough to dissociate the excitons directly. Hence, a process has to be introduced that efficiently separates the bound electron-hole pairs. This is possible at the sharp drop of potential at donor-acceptor (D-A) as well as semiconductor/metal interfaces. In the following, the most basic device architectures are reviewed and the individual advantages and disadvantages are discussed. Their main difference lays in the exciton dissociation or charge separation process, which occurs at different locations within the photoactive layer. A second issue is the consecutive charge transport to the electrodes.

1.5.1. Single layer

The first organic solar cells were based on single thermally evaporated molecular organic layers sandwiched between two metal electrodes of different workfunctions. The rectifying behavior of these devices can be explained by the MIM-model (for insulators) or by the formation of a Schottky barrier (for doped materials) between the metal with the lower work function and the p-type organic layer.³⁸ In Fig. 1.5.1.1 the situation is depicted for the case of

a Schottky junction at the aluminum contact. Close to the contact, in the depletion region W , a resulting band bending from the Schottky contact is depicted. This corresponds to an electric field in which excitons can be dissociated.

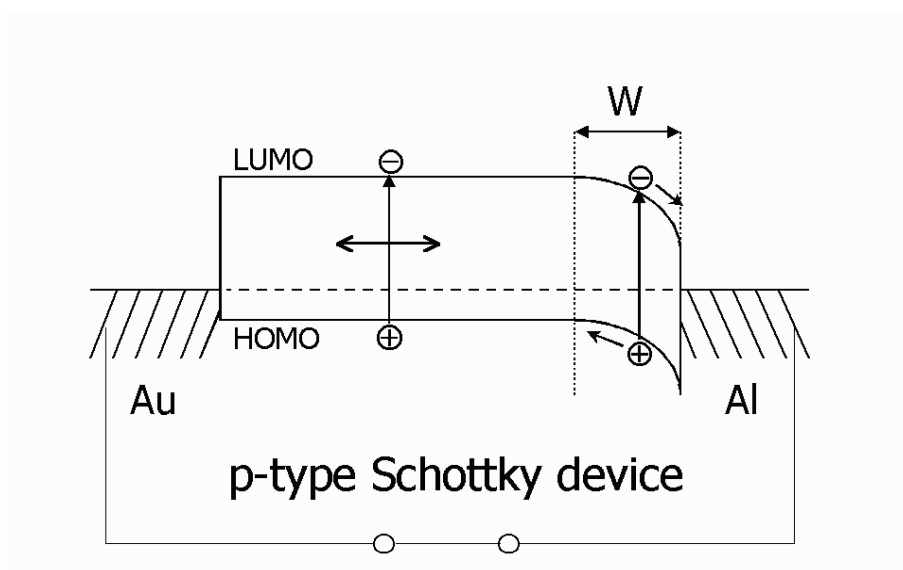


Fig. 1.5.1.1: Schematic of a single layer device with an Schottky contact at the aluminum contact. Photogenerated excitons can only be dissociated in a thin depletion layer W and thus the device is exciton diffusion limited.

Therefore illumination from the two different semi-transparent metal contacts can lead to sybatic (proportional to the absorption coefficient) and anti-batic behavior of the spectral photocurrent.^{7,34,103} Since the exciton diffusion length for most organic solar cell materials is below 20 nm, only those excitons generated in a small region within ≤ 20 nm from the contacts contribute to the photocurrent. Due to the high series resistances these materials show a low FF and a field dependent charge carrier collection. These thin film devices can work well as photodetectors, since under a high reverse bias the electric field drives the created charges to the electrodes. The illumination intensity dependence of the short circuit photocurrent was sublinear, as expected for bimolecular recombination, since the probability for recombination is proportional to both electron and hole concentrations.

1.5.2. Bilayer Heterojunction

In a bilayer device, a donor and an acceptor material are stacked together with a planar interface. There the charge separation occurs,^{13,26,39,106} which is mediated by a large potential drop between donor and acceptor. The bilayer is sandwiched between two electrodes matching the donor HOMO and the acceptor LUMO, for efficient extraction of the

corresponding charge carriers. The bilayer device structure is schematically depicted in Fig. 1.5.2.1, neglecting all kinds of possible band bending due to energy level alignments.

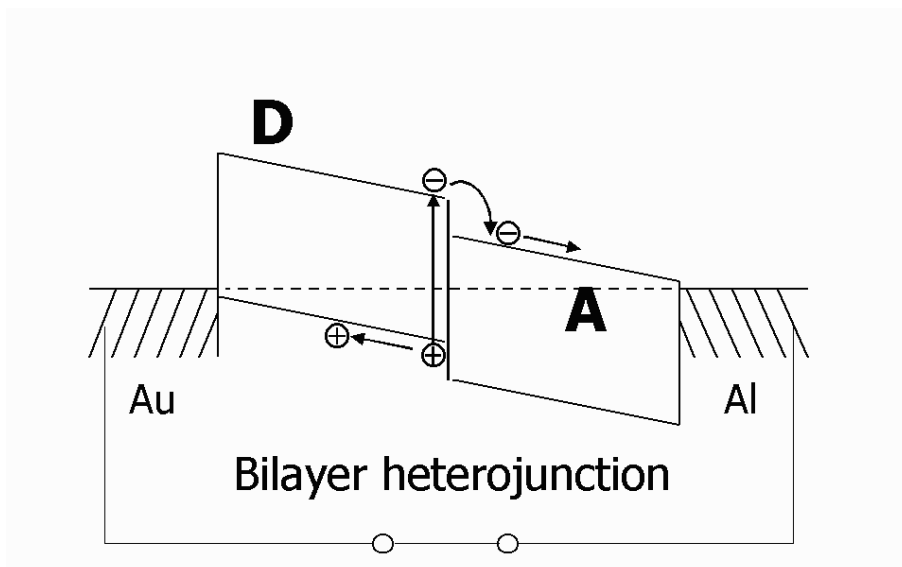


Fig. 1.5.2.1: Schematic of a bilayer heterojunction device. The donor (D) contacts the higher and the acceptor (A) the lower work function metal, to achieve good hole and electron collection respectively. Photogenerated excitons can only be dissociated in a thin layer at the heterojunction and thus the device is exciton diffusion limited.

While the formation of a classical p/n-junction requires doped semiconductors with free charge carriers to form the electric field in the depleted region, the charge transfer in bilayer heterojunction between undoped donor and acceptor materials is due to the differences in the ionization potential and electron affinity of the adjacent materials (compare Fig. 1.1). Upon photon absorption in the donor D, the electron is excited from the HOMO to the LUMO ($S^0 \rightarrow S^1$). If now an acceptor molecule A is in close proximity, the electron may be transferred to the LUMO of A, which is energetically preferential when

$$I_{D^*} - A_A - U_C < 0,$$

where I_{D^*} is the ionization potential of the excited state (D^*) of the donor, A_A the electron affinity of the acceptor and U_C the effective Coulomb interaction, respectively.⁵

The release in electron energy may then be used to separate electron and hole from their coulomb potential. It is noteworthy that this photoinduced charge transfer (CT) only occurs under illumination, since it needs the excitation energy of the electron in the donor to reach the LUMO in the acceptor. There are experimental indications¹³¹⁻¹³³ supported by

theoretical considerations¹³⁴ for the formation of an interfacial dipole between the donor and acceptor phases, independent of illumination. This can stabilize the charge-separated state by a repulsive interaction between the interface and the free charges.¹³⁴ Therefore, the success of the D-A concept lays to a great extent in the relative stability of the charge separated state: the recombination rate between holes in D and electrons in A is several orders of magnitude smaller than the forward charge transfer rate.^{111,135,136}

A big advantage over the single layer device is the monomolecular charge transport. After the excitons are dissociated at the materials interface the electrons travel within the n-type acceptor and the holes travel within the p-type donor material. Hence holes and electrons are effectively separated from each other and thus charge recombination is greatly reduced and depends more on trap densities. As a consequence, the photocurrent dependency on illumination intensity can be linear,^{13,26,34,52,106} and for thinner layers larger filling factors can be achieved.³⁹

Bilayer devices can be either produced by sequential thermal deposition of pigments,^{13,34,39,104,106} by solution casting of one soluble material and evaporation of a second layer^{21,22,52,53,137} or by sequential solution casting applying a polymer precursor route.¹³⁸ Power conversion efficiencies of about 3.6% under AM 1.5 solar illumination with this geometry were reported with an evaporated bilayer device using copper phthalocyanine and C₆₀.^{61,62}

1.5.3. Bulk heterojunction

The essence of the bulk heterojunction is to intimately mix the donor and acceptor components in a bulk volume so that each donor-acceptor interface is within a distance less than the exciton diffusion length of each absorbing site. In Fig. 1.5.3.1 the situation is schematically shown for a bulk heterojunction device, again neglecting all kinds of energy level alignments and interface effects. The bulk heterojunction device is similar to the bilayer device with respect to the D-A concept, but it exhibits a largely increased interfacial area where charge separation occurs. Due to the interface being dispersed throughout the bulk, no loss due to too small exciton diffusion lengths is expected, because ideally all excitons will be dissociated within their lifetime. In this conception the charges are also separated within the different phases and hence recombination is reduced to a large extent and the photocurrent often follows the light intensity linearly^{67,73,139} or slightly sublinearly^{54,140,141}.

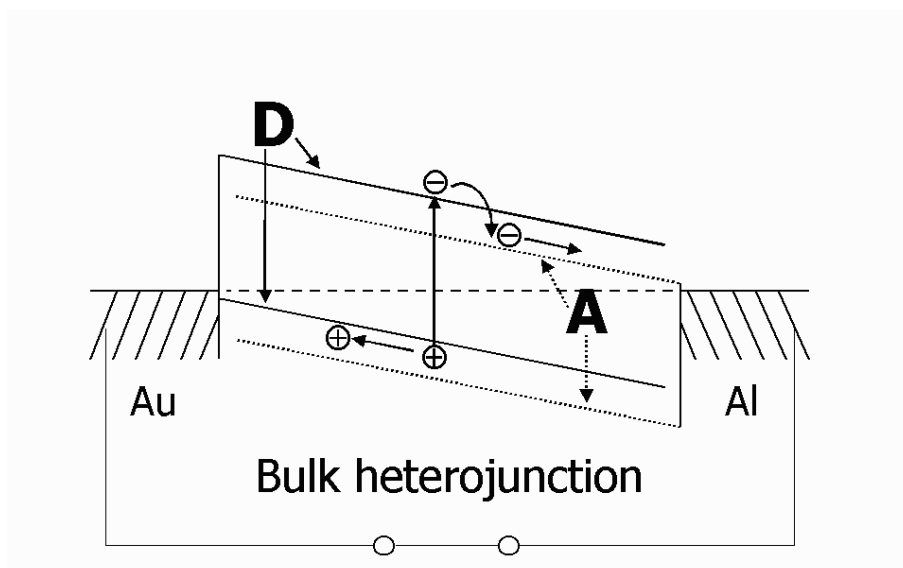


Fig. 11: Schematic of a bulk heterojunction device. The donor (D) is blended with the acceptor (A) throughout the whole film. Thus photogenerated excitons can be dissociated into charges at any place.

While in the bilayer heterojunction the donor and acceptor phase contact the anode and cathode selectively, the bulk heterojunction requires percolated pathways for the hole and electron transporting phases to the contacts. In other words, the donor and acceptor phases have to form a bicontinuous and interpenetrating network. Therefore, the bulk heterojunction devices are much more sensitive to the nanoscale morphology in the blend, which will be discussed in more detail below.

Generally, bulk heterojunctions may be achieved by co-deposition of donor and acceptor pigments^{43,71,72,108} or solution casting of either polymer/polymer⁵⁷⁻⁵⁹, polymer/molecule^{22,54,55,142,143} or molecule/molecule^{144,145} donor-acceptor blends. The most efficient devices today are based on solution cast P3HT:PCBM blends yielding above 3.5% power conversion efficiency under AM 1.5.⁶⁸

1.5.4. Diffuse Bilayer Heterojunction

Another device architecture, which is conceptually in between the bilayer and the bulk heterojunction device, is the diffuse bilayer heterojunction device. This device structure is aiming to adapt the advantages of both concepts, an enlarged donor-acceptor interface and an spatially uninterrupted pathway for the opposite charge carriers to their corresponding electrodes. The diffuse interface is achieved in different ways:

If processed from solution, two thin polymer films can be pressed together in a lamination procedure applying moderate pressure and elevated temperatures.⁶⁰ Another way to achieve a diffuse interface is to spin coat the second layer from a solvent that partially dissolves the underlying polymer layer.^{146,147} Finally, also the controlled interdiffusion between an acceptor fullerene and a donor polymer by annealing of a bilayer device¹⁴⁸ results in an intermixed interfacial region.

Calculated power conversion efficiencies approaching 2% were reported for the laminated polymer:polymer device for simulated AM 1.5 conditions.⁶⁰

1.6. Morphology of Organic Materials

The morphology (greek: “morphe” – form and “logos” – word, thought) of organic materials deals with the structural order on a supermolecular scale. For example it is well known that in the class of semiconducting organic materials smaller molecules tend to crystallize.¹⁴⁹⁻¹⁵¹ The binding energy of these organic crystals originates from intermolecular van der Waals attractions and is thus less strong than in inorganic materials, where crystals are made out of covalent bonds between atoms or coulombic attractions between ions in salts.

Morphology has a profound effect on materials properties such as charge carrier mobilities, optical absorption and mechanical qualities. For optoelectronic devices based on organic thin films, mainly the former two features are of importance, as the films are usually deposited onto substrates that provide the mechanical necessities. For composites of organic materials the arrangement of these materials plays a major role. Based on the fact that the molecular structure can be regarded as primary structure, the intermolecular order can be viewed as secondary structure whereas the composite structure may be understood as tertiary structure. Finally interactions between the organic materials with the substrate may influence the interfacial film structure.

The geometry of organic thin films gives the interface between the organic material and the substrate a special importance. The interfacial and possibly also subsequent layers are influenced by interactions between the substrate and the organic molecules.¹⁵¹⁻¹⁵³ Crystalline substrates even offer the possibility of epitaxial growth, so that the molecules arrange in a very defined way with respect to molecular axes and substrate lattice. Thus the epitaxy of organic thin films can lead to highly oriented growth even with respect to lateral dimensions (compare Fig. 1.6.1).^{154,155}

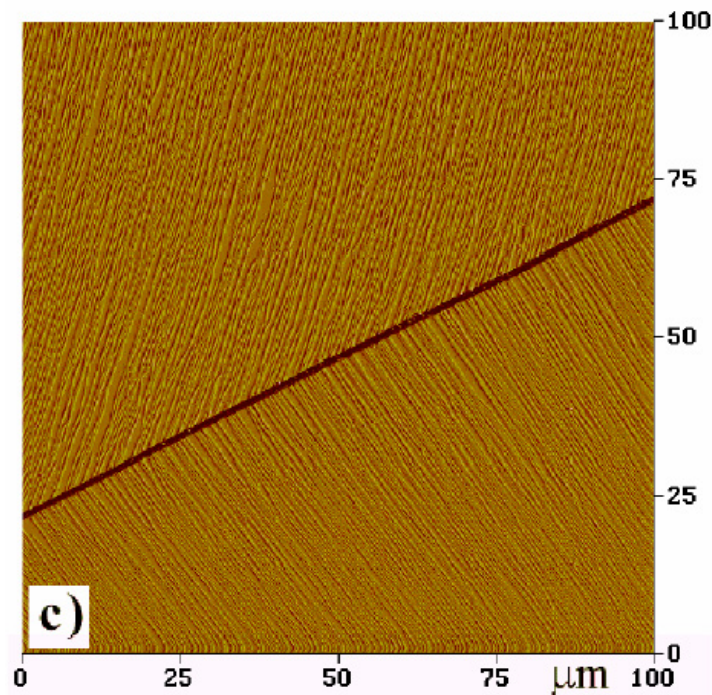


Fig. 1.6.1: AFM images characterizing the needle-like morphology of PSP films on cleaved (001)-oriented mica. The image shows the deflection or error signal of the AFM-feedback at a big cleavage step of the mica.¹⁵⁴

In general and for non-crystalline substrates only the orientation of the molecule with respect to the substrate normal is caused by specific interactions. For example hydrophilic substrates (as glass or SiO₂) can cause repulsion to organic conjugated molecules, whereas hydrophobic substrates like HF treated silicon are attractive for the same molecules. The former will often lead to upright standing oligomers and the latter to flat lying molecules. In general, a certain equilibrium angle between the long axis of the molecule and the substrate normal will be the case.

The orientation and following growth of crystalline domains has a profound effect on organic field effect transistors.²⁰ Especially the charge carrier mobility is determined by the quality or mean size of organic crystallites formed at the substrate interface. The mean crystallite size as well as molecular orientation are a function of substrate temperature during deposition, the evaporation rate and of fundamental substrate molecule interactions favoring oriented growth.^{116,151,154-156} Finally the application of Langmuir-Blodgett or chemical grafting techniques offer the ultimate control in growing molecular mono- or multilayers.¹⁵⁷

Whereas the planar structure of conjugated molecules often forces the growth of crystallites, dendrimers¹⁵⁸⁻¹⁶⁰ and polymers often resist crystallization and favor amorphous structures. However, certain polymers exhibiting high order in the side-group orientation (e.g. regio-

regular P3HT) can result in a nematic liquid-crystalline order. For example it was found that asymmetric substitution of the side chains of a PPV-derivative resulted in a coiled polymer structure, whereas symmetric substitution yielded linear orientation.¹⁶¹ In general the shape of a polymer in solution is coiled like a ball of wool.¹⁶²⁻¹⁶⁴ The size of the single polymer coils (characterized by a hydrodynamic radius) can thus be determined by light-scattering; better solvents lead to larger hydrodynamic radii.¹⁶⁵ While at lower solution concentrations polymers are separated single molecules, higher concentrations will cause some overlap of polymer coils resulting in entanglement. The concentration and solvent dependent conformation of polymers directly result in different conjugation lengths and possibly aggregation, which has a strong impact on polymer light emitting diodes.¹⁶⁵⁻¹⁶⁸

Crystalline order has been detected in films of P3HT, where the backbone of the polymer was usually found to be parallel to the substrate plane, but the orientation of the sidegroups was either perpendicular or parallel to the substrate (compare Fig. 1.6.2).^{118,120,169,170} The preferential parallel orientation of the polymer main chain will lead to an anisotropic optical behavior of the polymer films.

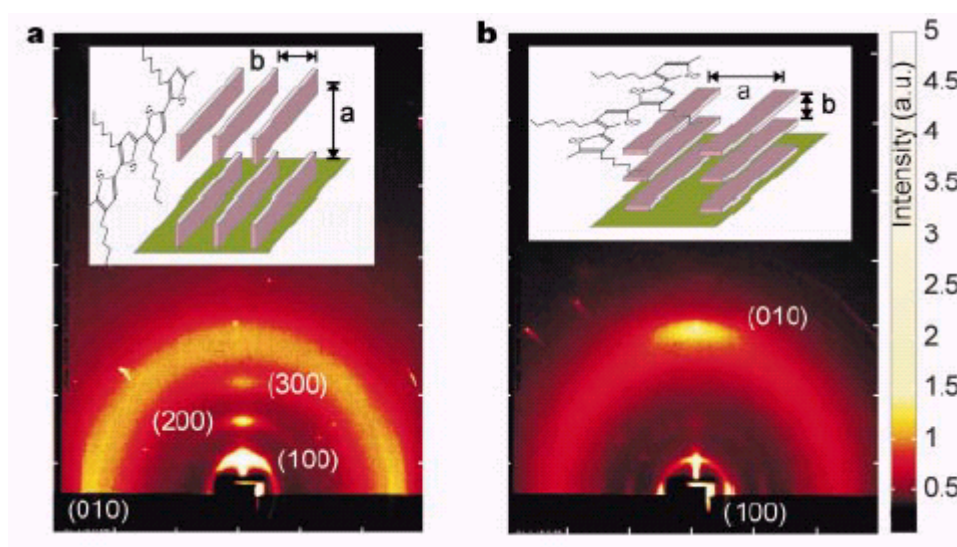


Fig. 1.6.2: Two different orientations of ordered P3HT domains with respect to the FET substrate. **a**, **b**, The wide-angle X-ray scattering images are a colour representation of the two-dimensional distribution of scattered Cu Ka X-ray intensity from spin-coated, 70–100 nm thick P3HT films with regioregularity of 96% (**a**) and 81% (**b**) on SiO₂/Si substrates. The vertical (horizontal) axes correspond to scattering normal (parallel) to the plane of the film. The insets show schematically the different orientations of the microcrystalline grains with respect to the substrate. (reproduced from Sirringhaus et. al¹¹⁸)

A systematic study of the optical anisotropy of regioregular P3OT films revealed that the parallel order is present mainly at the interface to the substrate but levels off towards the bulk of the film.¹²¹ Here it was found that neither solution concentration nor spin frequency but the film thickness is the decisive parameter for the anisotropy over the range of parameters studied. Furthermore it was revealed that spin casting did not yield higher anisotropy than drop casting – even contrary, since the longer drying time of drop cast samples allowed for a better alignment of the polymer chains.¹²¹ However, via HF treatment the parallel orientation of P3OT could be increased and thus the substrate polymer interaction determines to a high extent the degree of order.¹²¹

Similarly, the compatibility of silicon substrates with a native SiO₂ layer with organic semiconductors could be raised via the insertion of interface layers, which was applied in the production of organic field effect transistors.¹⁷¹ Since the charge carrier mobility along the backbone of the conjugated polymer is in general the highest,¹⁷² also a lateral orientation of polymers on pre-structured substrates has been applied for organic field effect transistors.^{119,173,174}

Due to the highly reduced entropy of mixing in polymer blends when compared to molecular blends, the free energy of mixing will usually favor demixing, even for chemically almost identical polymers. Spin cast films present in general a quenched state of the solution, which allows to produce blend polymer films, even if they are thermodynamically not favorable. Demixing or spinodal decomposition will then occur at significantly higher temperatures than the glass transition temperature of the compounds. In the presence of preferential segregation of one component towards interfaces, quite complicated demixing scenarios can occur.¹⁷⁵ A comprehensive review on the link between morphology of conjugated polymer blends and device function of light emitting diodes and photodiodes is given by Moons.¹⁷⁶

1.6.1. Introduction to Morphology of conjugated Polymer/Fullerene Bulk Heterojunction Solar Cells

Already in the first study on conjugated polymer/fullerene D/A bulk heterojunction solar cells it was reported, that the limited solubility of C₆₀ in organic solvents and its tendency to crystallize during film formation prevents the use of high concentration blends.⁵⁴ This limitation was overcome by the application of soluble C₆₀ derivatives, developed previously.⁵⁶ The soluble PPV derivative used was poly(2-methoxy-5(2'-ethyl-hexyloxy)-1,4-phenylene-vinylene) (MEH-PPV).¹⁷⁷ On changing the solvent from xylene to 1,2-dichlorobenzene “high-quality” spin cast MEH-PPV:PCBM films with weight ratio compositions of up to 1:4 were achieved.⁵⁴ These devices outperformed pristine MEH-PPV devices with a by two orders of magnitude increased photocurrent at 430 nm 20mW/cm² monochromatic laser illumination. The first morphology study dedicated to the MEH-PPV:C₆₀ system applying transmission electron microscopy was reported by Yang and Heeger.⁵⁵ They selectively dissolved the fullerene from thin blend films using decahydronaphthalene, and observed both isolated and connected regions with characteristic size of about 10 nm, corresponding to the C₆₀ phase. For increasing C₆₀ content the authors reported increasing percolation and bicontinuous network formation of the C₆₀ phase within the MEH-PPV network. Furthermore, the application of electron diffraction on MEH-PPV:C₆₀ blends with weight ratio of approximately 1:4 revealed a crystalline organization of the C₆₀. The authors concluded the C₆₀ to be present in the blend in the form of nanocrystallites having sizes of roughly 10 nm.⁵⁵ A following study on the same system reported on the composition dependence of short circuit current and open circuit voltage of solar cell devices.¹⁷⁸

Shaheen et al. achieved the next major step in the development of the polymer/fullerene bulk heterojunction solar cell, reporting an AM 1.5 solar power conversion efficiency of 2.5%.⁶³ The authors reported a strong dependence of the performance on the solvent used: whereas toluene cast devices yielded power conversion efficiencies of only 0.9% the use of chlorobenzene almost trebled the efficiency. This increase was mainly due to an increase of the short circuit current (compare Fig. 1.6.1.1) and the authors attributed this to a finer film morphology, revealed by atomic force microscopy (AFM).⁶³

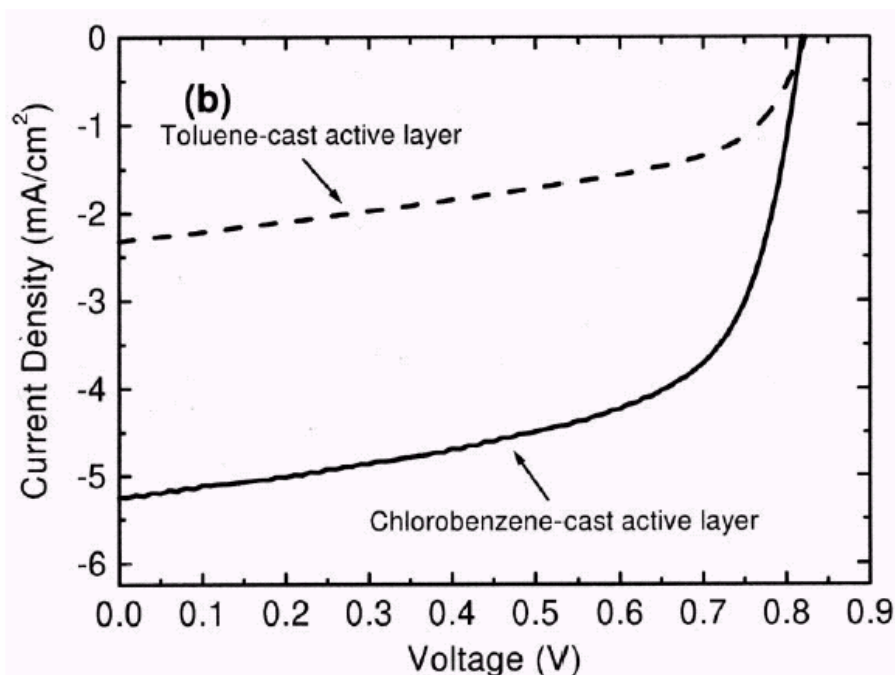


Fig. 1.6.1.1: Effect on photocurrent of the solvent used for spin casting the active layer, a blend of MDMO-PPV/PCBM 1:4 by weight.⁶³

In another study on the MEH-PPV:C₆₀ system, Liu et al. correlated the solar cell device parameters with the different solvents (xylene, chlorobenzene, 1,2-dichlorobenzene, chloroform and tetrahydrofuran) used. They claimed that non-aromatic solvents prevent an intimate contact between the MEH-PPV backbone and C₆₀, thus reducing the charge transfer efficiency and subsequently the photocurrent, but increasing the photovoltage. Also by AFM measurements they found the tetrahydrofuran based devices to exhibit a larger phase separation. Furthermore the authors used the phase image of the AFM scans to determine the ratio of C₆₀ and MEH-PPV exposed to the surface of the film and correlated this to the observed open circuit voltages with a simple linear combination.

Gebeyehu et al. compared also the morphology and performance of poly(3-octylthiophene) (P3OT)/ fullerene blends.¹⁷⁹ Here the authors reported that blends with C₆₀ yielded more homogeneous films than when PCBM or multiple substituted C₆₀ was used. To overcome the large-scale phase separation in P3OT/C₆₀ blends, Camaioni et al. applied plasticizers (e.g. PL1: a poly(3-butyl-co-3,4-dibutylthiophene) copolymer with 50:50 ratio between 3-butyl and 3,4-dibutyl thiophenes), to increase the compatibility between the two components.¹⁸⁰ Indeed the size of the C₆₀ crystallites was reduced to a large extent and more homogeneous blends resulted. Fig. 1.6.1.2 displays the change in morphology from P3OT/C₆₀ (1:1) to P3OT/PL1/C₆₀ (1.5:0.5:2), obtained by TEM.

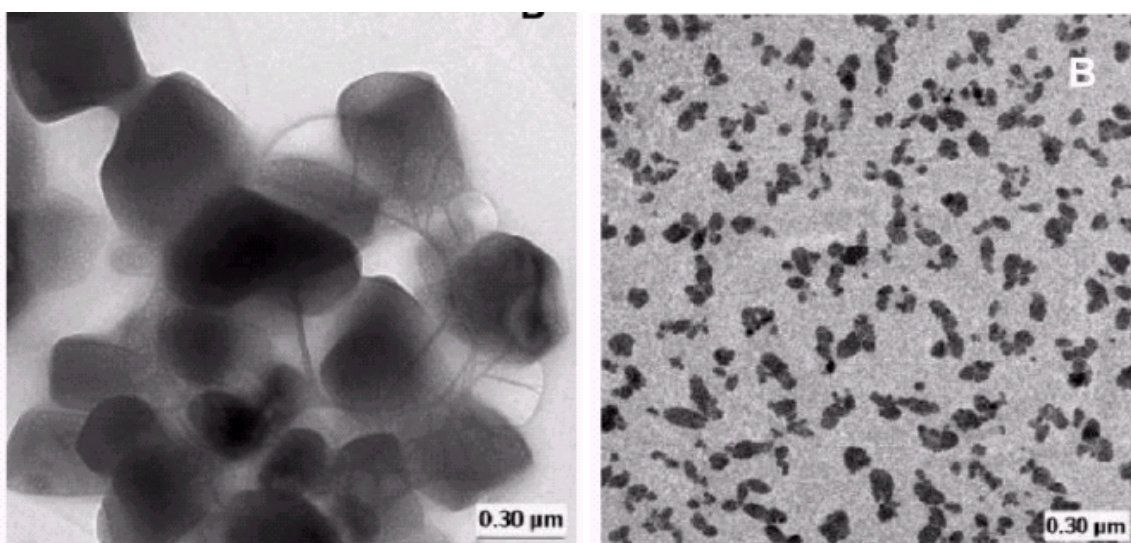


Fig. 1.6.1.2: Transmission electron micrographs of P3OT/C₆₀ (1:1) (left) and P3OT/plasticizer/C₆₀ (1.5:0.5:2) (right) blends. Due to the plasticizer the average C₆₀ domain decreased drastically in size.¹⁸⁰

More recently Rispen et al. have compared the surface topography of MDMO-PPV:PCBM devices by varying the solvent from xylene (X) over chlorobenzene (CB) to 1,2-dichlorobenzene (DCB). The authors found a decrease in phase separation from X over CB to DCB.¹⁸¹ Furthermore they proposed a certain crystal packing of the PCBM molecules, inserting even solvent molecules into the crystal. These data were based on crystals grown from solution.¹⁸¹

Martens et al. have comparatively investigated the nanostructure of MDMO-PPV:PCBM bulk heterojunction by applying transmission electron microscopy (TEM) on films and cross sections of films spin cast from toluene and chlorobenzene.¹⁸²⁻¹⁸⁴ On increasing the PCBM concentration in the blends, the authors observed increasing dark clusters and attributed these to the fullerene-rich phase. Since for the ratio 1:1 (1:2) of MDMO-PPV:PCBM for toluene (chlorobenzene) cast films there was no phase separation visible, it was concluded that a homogeneous blend of PCBM and MDMO-PPV exists around the PCBM clusters. Systematically the PCBM clusters in the toluene cast films are larger in size (up to several 100 nm) as compared to chlorobenzene cast films (less than 100 nm). In the TEM cross-sections of films spin cast on PET the fullerene-rich clusters are again visible as darker regions (compare Fig. 1.6.1.3).

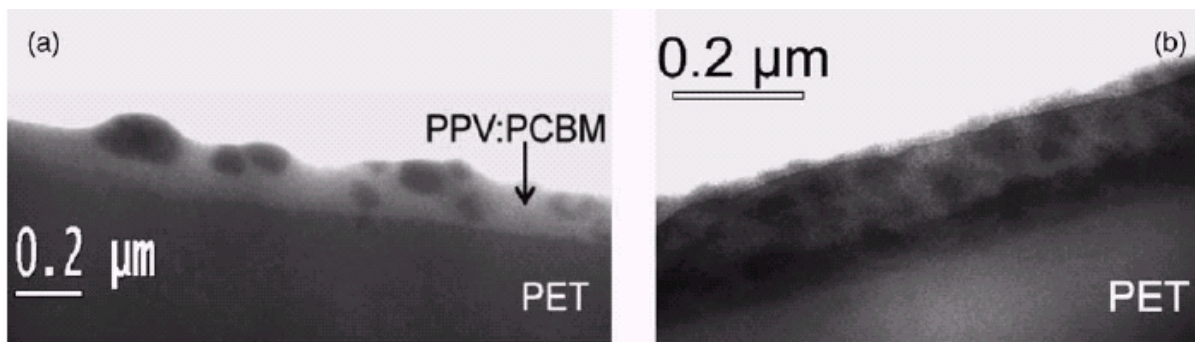


Fig. 1.6.1.3: TEM cross-sectional view of 1:4 MDMO-PPV:PCBM films spin cast from toluene (a) and chlorobenzene (b) on a PET substrate. The darker regions were attributed to PCBM rich regions.¹⁸⁴

Furthermore Martens has shown by AFM, that the drying time is an important parameter for the size of the phase-separated structures. By introducing a hot air flow over an drying film, the drying time could be decreased and consequently the extent of phase separation was reduced.¹⁸³ Here the film thickness was kept constant for comparability, by a first fast thickness determining step, which was applied prior to the drying.

More recently it has been shown by electron diffraction that PCBM is capable to organize in crystalline order in pristine PCBM films.¹⁸⁵ In a more comprehensive study again MDMO-PPV:PCBM blends have been studied and in all blends with varying composition diffraction fringes were detected. Hence it was concluded, that PCBM evolves in nanosized crystallites in the blend. Furthermore the authors have shown that upon annealing the PCBM will organize in larger crystals – thereby destroying the original blend morphology. As a conclusion, the morphological instability at elevated temperatures was drawn.¹⁸⁶

Very recently van Duren et al. reported a comprehensive study relating the morphology of MDMO-PPV:PCBM blends cast from chlorobenzene to solar cell performance.¹⁸⁷ The authors applied a variety of techniques including AFM, TEM, photoluminescence (PL), depth profiling with Time-of-Flight Secondary Ion Mass Spectrometry (TOF-SIMS) and standard solar cell characterization. The compositions between MDMO-PPV and PCBM were spanned over a wide range. After a rather homogeneous mixing for PCBM contents less than 50%, the authors claim a rather abrupt improvement in the device properties with the observed onset of phase separation around 67% PCBM content. By labeling of PCBM with deuterium, the composition of the fullerene could be followed by TOF-SIMS throughout the depth of the active layer with the result of a rather even distribution. PL measurements revealed that only a small addition of PCBM to MDMO-PPV yields an effective quenching though a small signal

could always be recorded. On the other hand, the addition of a small fraction of MDMO-PPV to PCBM resulted only in a gradual quenching of the PCBM PL signal, indicating the relatively large PCBM domains to be “rather pure”.

The motivation of the present study is triggered by the findings of Shaheen et al.⁶³ and aims towards the decoding of the phase distribution within MDMO-PPV:PCBM blends cast from both, toluene and chlorobenzene. In addition the reasons for the difference in conversion efficiency caused by these morphologies should be identified.

2. Experimental

In this section the material system (2.1) as well as the preparation (2.2) and characterization (2.3) of conjugated polymer/fullerene bulk heterojunction organic plastic solar cells is described. Furthermore a variety of experimental measurement techniques for studying the nanoscale morphology are introduced (2.4). Finally the setup for the photoluminescence measurements is given (2.5).

2.1. Materials

The main material system under investigation consisted of photovoltaically active blends of MDMO-PPV (poly-[2-(3,7-dimethyloctyloxy)-5-methoxy]-para-phenylene-vinylene) and PCBM (1-(3-methoxycarbonyl) propyl-1-phenyl [6,6]C₆₁). The chemical structure of the two is depicted in Fig. 2.1.1.

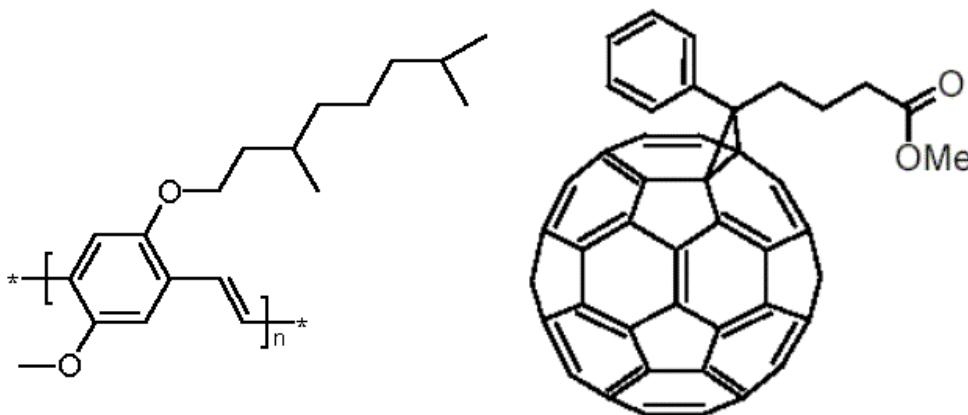


Fig. 2.1.1: Chemical structure of MDMO-PPV and PCBM.

MDMO-PPV had a molecular weight of about 10^6 (M_W 1.150.000 g/mol / M_N = 170.000 g/mol), a glass transition temperature of about 65 °C and was provided by Covion (Germany).¹⁸⁸ PCBM of purity better than 99.5% was purchased from J. C. Hummelen (Univ. of Groningen, The Netherlands). PEDOT:PSS (poly[3,4-(ethylenedioxy) thiophene] : poly(styrene sulfonate)) (Baytron P or PH) was purchased from Bayer (Germany) and its structure is shown in Fig. 2.1.2. ITO covered glass was purchased from MERCK (Germany).

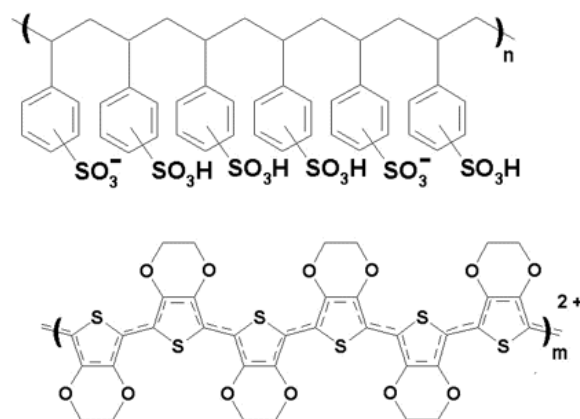


Fig. 2.1.2: Chemical structure of PEDOT (bottom) and PSS (top).

2.2. Solar Cell Preparation

The construction of organic bulk heterojunction solar cells based on conjugated polymer/fullerene blends is done with several consecutive steps. As transparent conducting substrate ITO-covered glass is chosen. The ITO layer serves thereby as anode in the solar cell configuration. Part of the ITO anode layer is etched away using the following formulation: concentrated HCl : concentrated HNO₃ : H₂O in the volume ratios 4.6 : 0.4 : 5. This allows contacting the back contact or cathode without shortcircuiting the thin film device. Next a thin layer of PEDOT:PSS in the formulation Baytron P or PH is spin cast on top of the ITO layer at a spin frequency of 1500 rpm. The standard spin program also used for casting of the active layers consisted of two steps, one at 1500 rpm (40 sec) and one at 2000 rpm (20 sec), with a rising spin speed for a few seconds (~5 sec) before each step. A part of the PEDOT:PSS layer is then removed by wiping with water or water/alcohol mixtures to allow for a good contact of the anode. After some time (at least 30 min) of drying in the ante-chamber of the glove-box, the active layer is spin cast from a MDMO-PPV:PCBM blend solution. Again a part of the active layer is removed by wiping with toluene to enable a good anodic contact. Another drying step is introduced before the thermal evaporation of the back contact, which consists of

aluminum (>50 nm) or an LiF/aluminum (~0.6 nm/>50 nm) combination. The evaporation step is done in a vacuum chamber inside the glove-box at a pressure better than 10^{-5} mbar. A schematic of the solar cell structure is presented in Fig. 2.2.1.

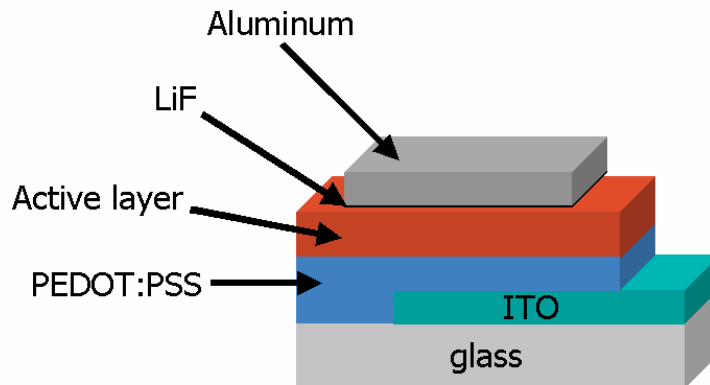


Fig. 2.2.1: Schematic of the thin film solar cell design.

Commonly a quadratic substrate geometry with side length of 15 mm was chosen, and this process yields three separate solar cells with active areas between 10 to 20 mm² defined by the evaporation mask and the edge of the ITO layer.

2.3. Solar Cell Characterization

To characterize the performance of the solar cell devices current-voltage (IV) and spectral photocurrent measurements were applied. The IV curves allow determining the maximum power output and thus the power conversion efficiency, whereas the spectral photocurrent measurements yield the number of collected electrons (fraction of one) per incident photon. Hence the latter is also called Incident Photon to Collected Electron (IPCE) measurement.

2.3.1. Current-Voltage (IV) Measurements

In the IV measurements a voltage, usually in the range between -2 to 2 Volts, is applied to the solar cell diode and the resulting current is measured. To apply the voltage and measure the resulting current a Keithley 2400 or 236 digital source meter in combination with a computer program was used, whereby the voltage range was swept through in little steps of 10 mV. The measurements tool place inside the argon glove-box system. IV-curves were measured in the dark or under simulated AM 1.5 solar irradiation using a solar simulator (Steuernagel 575) attached to the glove-box. The light intensity used varied between 80 and 100 mW/cm².

2.3.2. Spectral Photocurrent Measurements

Spectral photocurrent was recorded under illumination of a monochromatized Xenon-lamp with a typical illumination density of 5-10 μW . The incident beam was chopped with a mechanical chopper, the photocurrent was detected with a lock-in-amplifier. The Xe-lamp spectrum was measured with a calibrated Si-diode. The IPCE spectrum is calculated as the ratio between the number of extracted electrons and the number of incident photons:

$$IPCE(\%) = \frac{\# electrons_{out}}{\# photons_{in}} \cdot 100 = \frac{1240eV \cdot I_{SC}}{\lambda[nm] \cdot P_{in}},$$

where P_{in} denotes the incident light power in W/cm^2 , I_{SC} the short circuit photocurrent in $\mu\text{A}/\text{cm}^2$ and $1240/\lambda$ is the photon energy in eV at the wavelength λ .

2.4. Morphological Characterization

Optical microscopy is generally limited to resolutions of the light wavelength used (Abbe criterion). In good case this yields a resolution of about 0.5 μm . Therefore other imaging techniques are required, if the nanoscopic regime needs to be entered.

Conceptually similar to the optical microscope, electron microscopes can be used, yielding to resolutions below one nanometer depending on the acceleration voltage of the electron beam. The ratio of the Planck's constant h over the momentum p of the electron determines the de Broglie wavelength of electrons. Note that for acceleration voltages larger than 100keV ($v \geq 0.55c$) the relativistic description of the electron momentum is required, thus $\lambda = h/m_e v = 1.225 \text{ nm}/[E(\text{eV})]^{1/2}$ ($U < 100\text{kV}$) and $\lambda_{rel} = h/[2m_{0,e} \cdot E(1 + E/2m_{0,e} \cdot c^2)]^{1/2}$ ($U > 100\text{kV}$).

Electrons likewise as X-rays can also be used for scattering experiments to investigate crystalline structures applying the Bragg condition.

Besides electron optics, many locally probing techniques have been developed since the early 1980ies. Here local interactions between a very sharp tip and the sample are observed in order to probe the surface topography of a film or another property of the film. These techniques are altogether Scanning Probe Microscopes (SPMs), which apply very sensitive piezo-scanners to raster the surface.

In the following, techniques applied in the context of this study are briefly introduced.

2.4.1. Atomic Force Microscopy (AFM)

The Atomic Force Microscope (AFM) or Scanning Force Microscope (SFM) was firstly realized by Binnig, Quate, and Gerber in the year 1986.¹⁸⁹ It is based on the earlier (1982) developed Scanning Tunneling Microscope (STM),¹⁹⁰⁻¹⁹² for which Binnig and Rohrer were awarded with half of the Nobel Prize in Physics in 1986.

These microscopes are used to image the surface topography of a sample down to the sub-nanometer scale. In the case of the STM a tunneling current is controlled between a relatively sharp tip and the sample and thus conducting samples and/or substrates are required. The AFM however requires no conductivity; here tip sample interactions are based on mechanic short or long-range forces. Especially the STM allows imaging at sub-atomic resolutions and it is used to even visualize amplitudes of electronic wave functions.

The basic setup of an AFM/STM consists of a measuring unit, a controller and a computer, which is collecting the data. To accomplish a full image, the sample is scanned line-by-line over a rectangular area with typically some few hundred lines using a sharp tip.

There are three basic measurement modes for the AFM: Contact mode, non-contact mode and tapping mode. The difference of which lies in the different tip sample interactions used to control a constant distance between tip and sample. In the contact mode the tip is touching the sample with a certain pressure, leading to a bending of the cantilever at which end the tip is mounted. Both the non-contact and tapping mode use extended tip sample interactions via van der Waals long-range forces over several nm distance. However, it is believed that in the case of the tapping mode the tip indeed “taps” (even through a possible the adsorbed fluid over layer) onto the film investigated.

Fig. 2.4.1.1 shows the basic SPM setup, consisting of the vibration-isolated microscope, a controller, the computer and the control and image monitors.

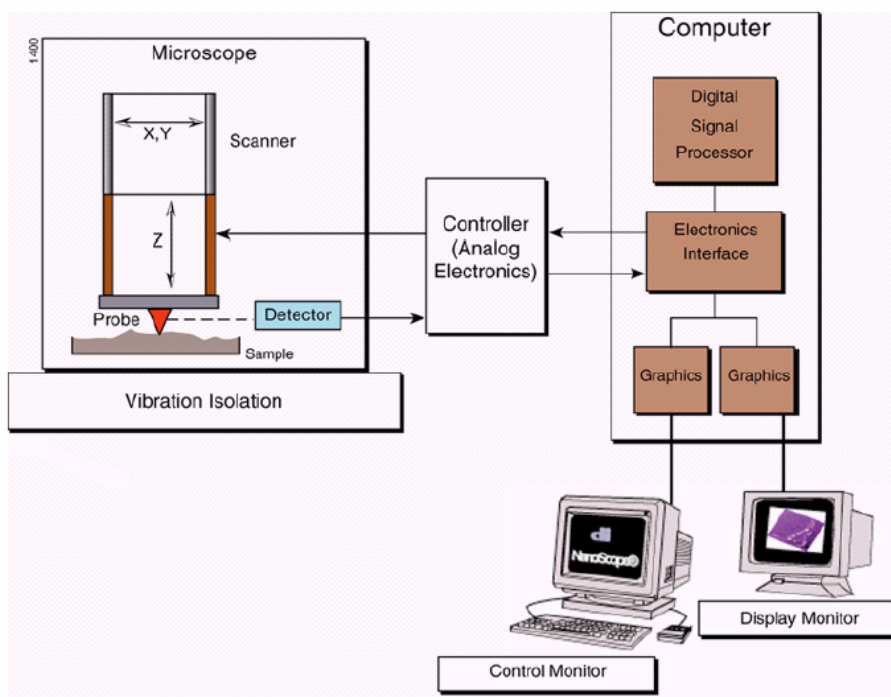


Fig. 2.4.1.1: Basic SPM setup, consisting of the vibration-isolated microscope, a controller, the computer and the control and image monitors.

For soft organic materials the tapping mode offers destruction less measurements at high resolutions. In the case of tapping or non-contact mode, a quartz piezo is used to excite the cantilever to oscillations. The amplitude of these oscillations is depending on the interactions with the sample surface and is basically the more damped the closer the tip approaches to the surface. To keep a constant distance to the surface, the feed back loop maintains a constant amplitude of the cantilever oscillation, which lies typically between 20 and 100 nm for the tapping mode and less for the non-contact mode. The amplitude is detected via a reflected laser spot unto a split photodiode detector, and the controller electronics applies a corresponding correction signal to the z-piezo of the scanner (compare Fig. 2.4.1.2).

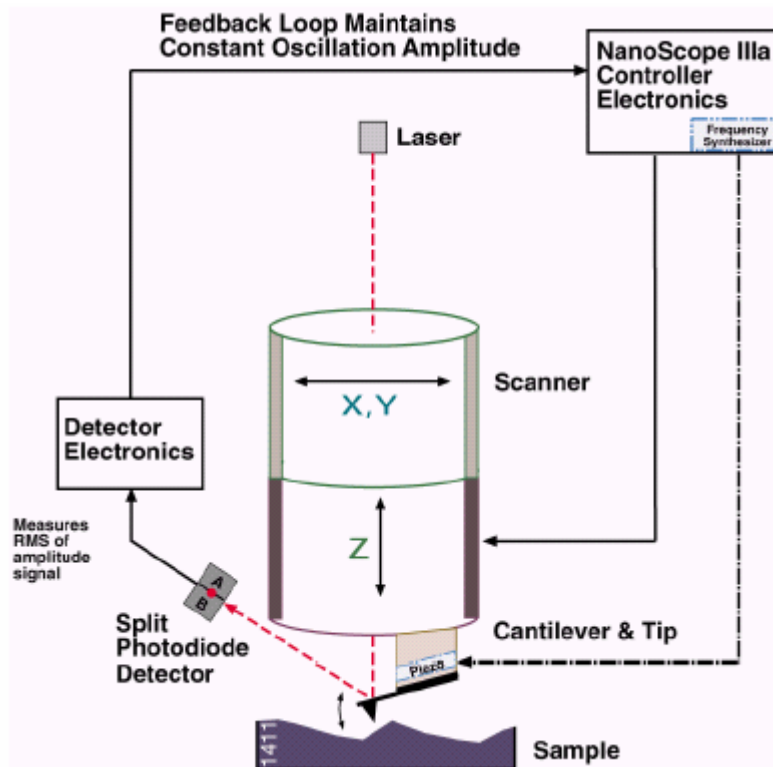


Fig. 2.4.1.2: Feedback loop controlled scanning of the sample topography for (non-contact and) tapping mode.

Fig. 2.4.1.3 shows in detail how the amplitude of the cantilever is detected. The amplitude is calculated from the root-mean-square (RMS) of the oscillation on the split photodiode detector. Fig. 2.4.1.4 displays the layout of the tube-piezo scanner. It consists of a part to control Z-movements, and respectively two parts to control movements in the X and Y direction. The extension or contraction of these piezos is performed by the application of some high voltages in the range -220 to $+220$ Volts. Fig. 2.4.1.5 shows in the left the design of the cantilever body part attached to the scanning head at the piezo-tube, whereas the right image displays an SEM image of the cantilever itself. Finally in Fig. 2.4.1.6 the shape of the actual tip, used for most measurements in this study, is displayed.

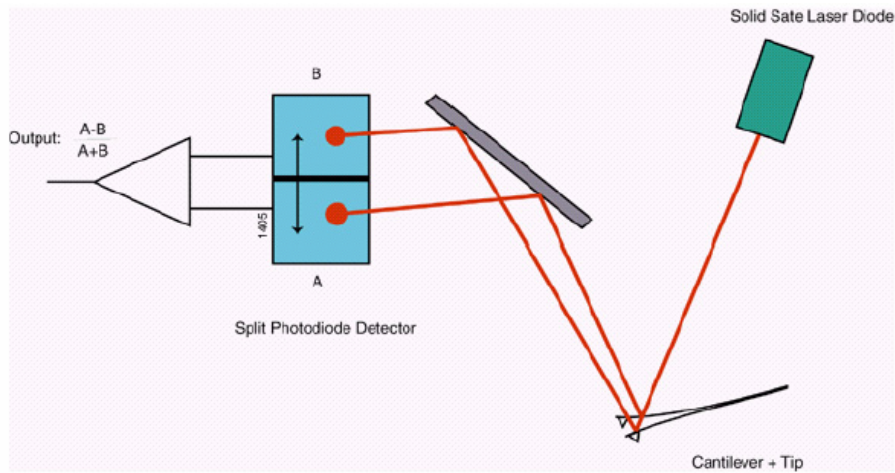


Fig. 2.4.1.3: Schematic of the detection of the cantilever amplitude.

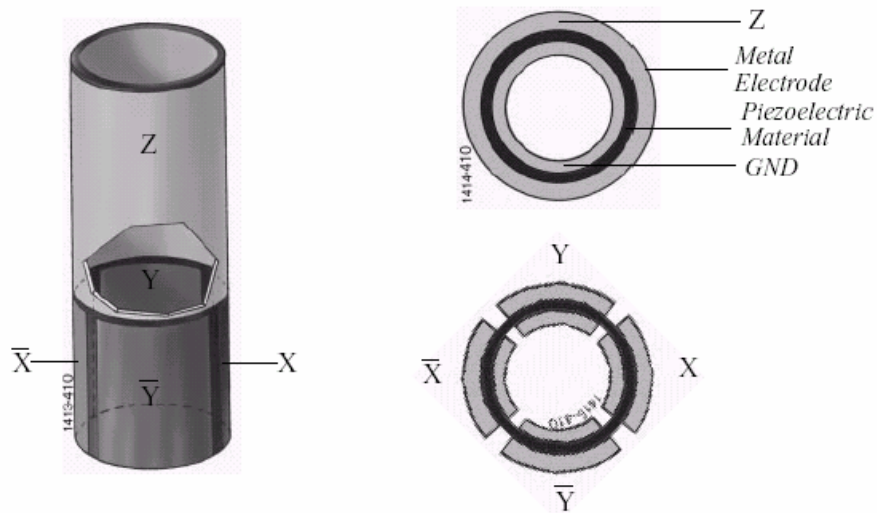


Fig. 2.4.1.4: Schematic of the scanner piezo tube. Indicated are the z, x, and y piezos, enabling movements in 3 dimensions.

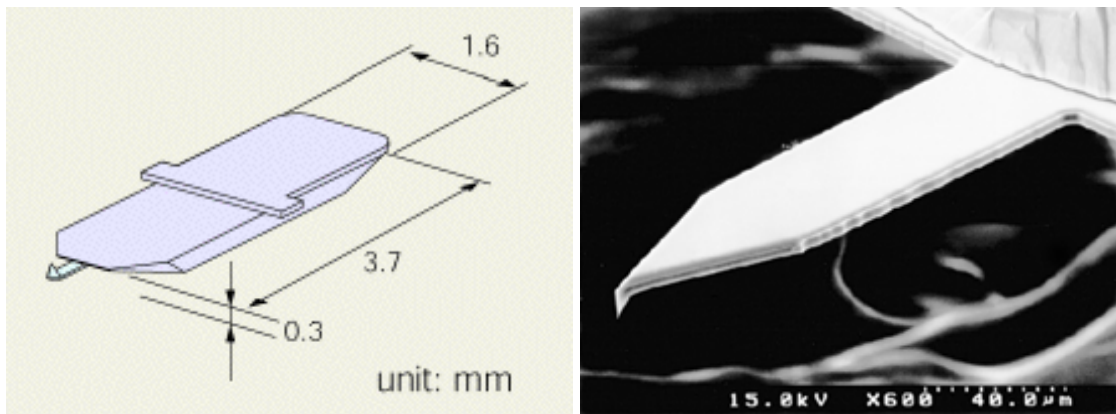


Fig. 2.4.1.5: Sketch of a tapping mode cantilever (Olympus AC160TS).

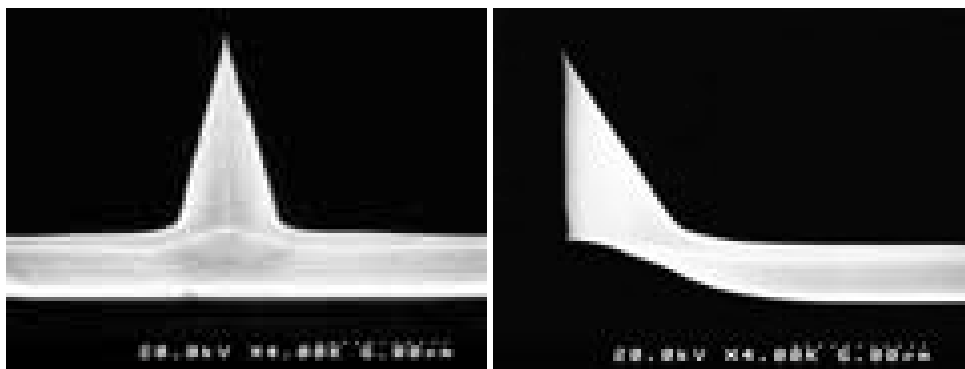


Fig. 2.4.1.6: Shape of a tapping mode tip (Olympus AC160TS).

Figures 2.4.1.7 to 2.4.1.9 demonstrate effects of the tip shape on the measured topography signal. While the geometry of the tip edges limit the obtainable steepness of the slope (Fig. 2.4.1.7), the sharpness of the tip end expressed by the radius of curvature limits the lateral resolution (Fig. 2.4.1.8). An ultimate limit for the lateral resolution is found in the radius of curvature of the tip itself, since the tip describes in the scanning motion around any feature in the topography at least a partial circle with its own tip radius.

For the case of thin organic films mainly the effects resulting from the tip sharpness have to be considered for the interpretation of the results, whereas maximum slopes are rather low and unimportant.

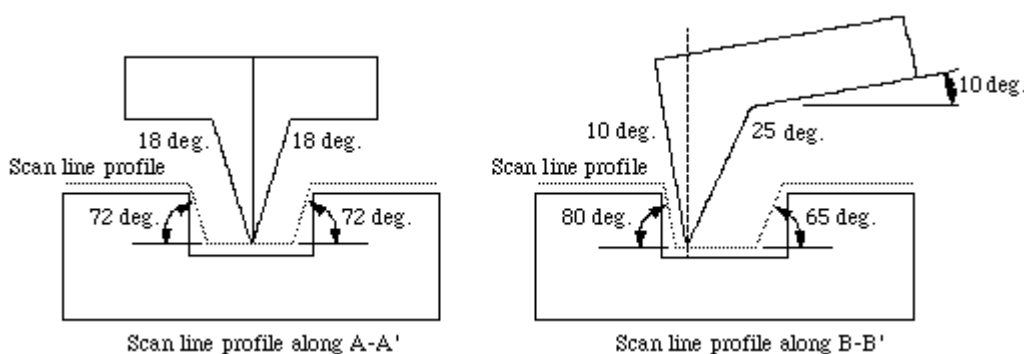


Fig. 2.4.1.7: Influence of tip apex angles on maximal scanning angles (Olympus AC160TS).

The system used for all AFM measurements was the Digital Instruments DI 3100 with a NanoScope IIIa controller (Digital Instruments, Santa Barbara, CA). Operation was done in tapping mode, for which OMCL-AC160TS tips were commonly used (Olympus, Tokyo, Japan).

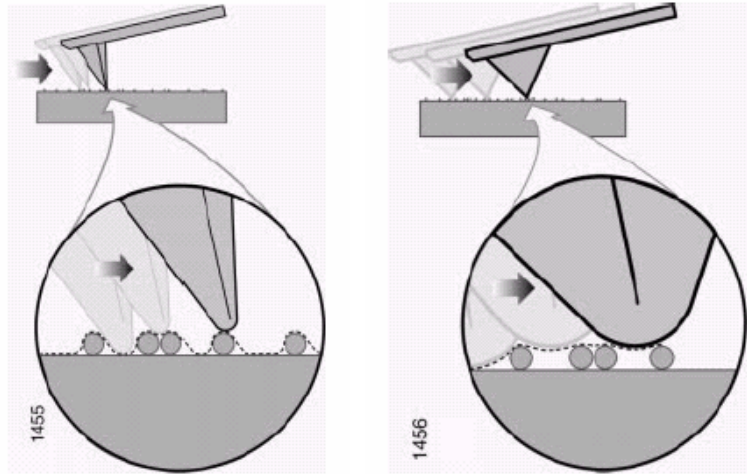


Fig. 2.4.1.8: Influence of the tip shape on achievable lateral resolutions. A smaller radius of curvature results in a higher resolution.

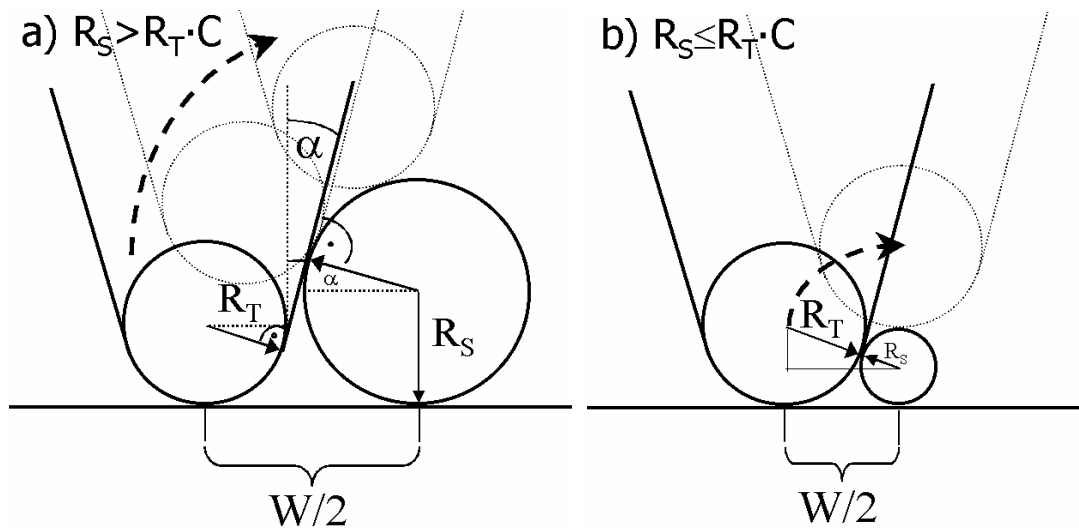


Fig. 2.4.1.9: The lateral resolution is generally limited by the finite tip radius of curvature (R_T) and apex angle α , and any (e.g. spherical) particle will appear enlarged.

From construction 2.4.1.9 (a) and (b) the apparent width W of a spherical sample is calculated as:

$$W/2 = (R_T + R_S)\cos\alpha + \tan\alpha[(R_T + R_S)\sin\alpha + (R_S - R_T)] \quad \text{for } R_S > R_T \cdot C,$$

$$\text{and } W/2 = [(R_T + R_S)^2 - (R_T - R_S)^2]^{1/2} \quad \text{for } R_S \leq R_T \cdot C,$$

with $C = (1 - \sin\alpha)/(1 + \sin\alpha) \leq 1$.

E.g. for a tip radius of 5 nm with an apex angle $\alpha=20^\circ$ and a spherical particle of 10 nm radius, the apparent width is obtained as $W = 35.6$ nm.

2.4.1.1. Light Microscopy (LM)

An optical microscope is included in the Dimension 3100 system for alignment issues. Images with a maximal resolution of about 2 μm can be digitalized for displaying larger areas than can be scanned in the AFM operation.

2.4.2. Transmission Electron Microscopy (TEM)

Ernst Ruska received the other half of the Nobel Prize in Physics in 1986 for developing the Transmission Electron Microscope (TEM) in the early 1930s.¹⁹³ The working principle of a TEM is principally very similar to that of an optical microscope. A parallel beam of accelerated electrons is transmitted through a specimen and a system of magnetic lenses is used to achieve the magnification of the image. The image is recorded with a CCD camera or with a conventional photo camera. By changing the focal length of one of the magnetic lenses, the electron diffraction pattern is readily yielded. This crystallographic information can now be restricted to a certain smaller area of the specimen by using an aperture. This technique is called Selected Area Electron Diffraction (SAED).

As electron source either a bent tungsten filament or a sharpened LaB₆ crystal is used in thermal electron emitters. The current density J of thermal electron emitters depends mainly on the work function of the material and the applied temperature:

$$J = A \cdot T^2 \cdot \exp\left\{-\frac{\Phi}{k_B T}\right\},$$

where T is the temperature in Kelvin, k_B is the Boltzmann constant, Φ is the work function of the material and A is the Richardson materials constant. The emitted electrons are bundled with a Wehnelt cylinder and accelerated behind it with an anode plate at a high voltage. This system is also called triode or thermionic gun.

Since only very thin samples can be investigated, a special sample preparation was necessary: Thin films were spin cast onto sodium metaphosphate (Victawet, SPI Supplies) covered glass slides under argon atmosphere. Then films were floated off the substrate by submerging the glass slide in deionized water and transferred onto Cu TEM grids. After drying films overnight in a N₂ flow box, the films were studied by Wolfgang Schwinger at the JKU in a JEM 2011 FasTEM (JEOL Ltd., Tokyo, Japan), used in transmission and diffraction mode.

2.4.3. Scanning Electron Microscopy (SEM)

Likewise the TEM the Scanning Electron Microscope (SEM) applies a parallelized electron beam for imaging of samples. However, in the case of SEM not primary electrons but secondary electrons, which are hit out of the sample, are detected. In contrast to the parallel image acquisition of TEM, the SEM image is generated sequentially by scanning the specimen with a highly focused electron beam. The first instrument was realized by Manfred von Ardenne in 1938.

Besides thermal electron emitters, often (cold) field emission guns are used to create an electron beam. By the application of high electric fields the potential barrier for electron emission is lowered considerably and electrons may tunnel through it. Since the electric field F depends like:

$$F = \frac{U}{r},$$

on the voltage U and the radius of curvature r , very sharp tungsten tips are applied to maximize the electron current density. The current density in the case of Fowler-Nordheim tunneling becomes:

$$J_t \sim F^2 \exp\left\{-C \frac{\Phi^{\frac{3}{2}}}{F}\right\},$$

where F is the electric field, C a constant and Φ is the work function of the tip material.

SEM measurements were performed by Michael Niggeman at the Fraunhofer Institute for Solar Energy (ISE, Freiburg, Germany) using a Cold Field Emission Scanning Electron Microscope Hitachi S-4700. Prior to imaging, the samples were covered by sputtering a thin platinum layer on their broken edge or on their top. Cross respectively break sections of films were achieved by scratching the ITO substrate with a diamond cutter and subsequent breaking of the substrate at room or liquid nitrogen temperature.

2.4.4. Kelvin Probe Force Microscopy (KPFM)

Kelvin Probe Force Microscopy (KPFM) applies the Kelvin Probe technique in combination with non-contact (NC) Atomic Force Microscopy (AFM) to determine the local electronic work function of a sample.¹⁹⁴⁻¹⁹⁷ Similar to the tapping mode, the NC mode uses an oscillating cantilever for scanning over the sample surface. A constant distance between tip and sample surface is here controlled by a constant frequency shift from the resonance frequency, by which a damped oscillation is accompanied (compare: damped driven harmonic

oscillator). Generally long-range interactions like van der Waals, electrostatic and magnetic forces determine the tip sample interaction. Here the frequency shift is approximately proportional to the force gradient.¹⁹⁸ Since no magnetic samples were investigated, the magnetic force will be omitted. For a tip radius of curvature of r , a Hamaker constant C_H between sample and tip, the van der Waals force is calculated as¹⁹⁹

$$F_{vdW} = -\frac{C_H r}{6z_{\min}^2},$$

with z_{\min} being the minimal tip-sample distance.

If actually there is a voltage U applied between tip and sample, the resulting electrostatic force can be written as:¹⁹⁹

$$F_{es} = -\frac{1}{2} \frac{\partial C}{\partial z} U^2,$$

where C denotes the capacitance and z the tip-sample distance.

If two materials are brought into contact with each other, a contact potential U_{CP} between them will result from their difference in work functions ($\Phi_1 - \Phi_2$):

$$U_{CP} = \frac{1}{e} (\Phi_2 - \Phi_1) = \frac{\Delta\Phi}{e},$$

where e is the elementary charge and Φ_1, Φ_2 the work functions of these materials.

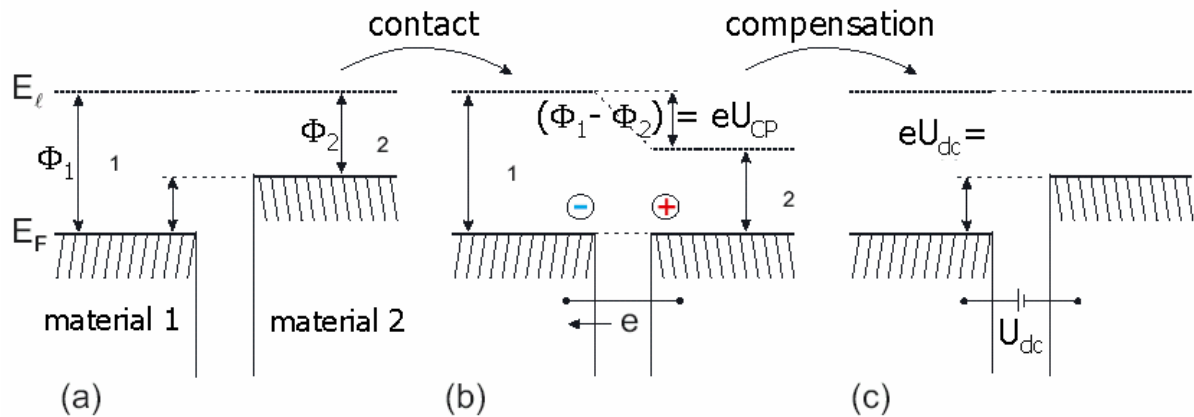


Fig. 2.4.4.1: If two materials 1 and 2 having work functions Φ_1 and Φ_2 (a) are brought into contact, the Fermi levels will equilibrate, and the contact potential is expressed by difference in the local vacuum potential (b). This potential difference can be compensated by application of a dc-voltage U_{dc} between the materials.(reproduced from Glatzel¹⁹⁹)

Introducing an external voltage U_{dc} between these two materials can compensate this contact potential, as illustrated in Fig. 2.4.4.1. This effect is used in conventional experiments, where a Kelvin probe is placed closely to the surface of the investigated sample. Vibrating this probe with a certain frequency ω_p to vary the distance results in a displacement current $I(t)$ according to:

$$I(t) = (U_{dc} - U_{CP}) \Delta C \cos(\omega_p t),$$

with ΔC being the capacitance change due to the distance variation. Cancellation of this current to zero by varying the externally applied bias voltage U_{dc} allows to determine the actual contact potential U_{CP} .

Though the NC-AFM exhibits already the distance variation *per se*, an additional ac-voltage U_{ac} is applied between tip and sample to detect the electrostatic forces independently of the van der Waals forces, which are used for the distance control. Thus the potential difference between tip and sample becomes:

$$U(t) = (U_{dc} - U_{CP}) + U_{ac} \sin(\omega_{ac} t).$$

With that the electrostatic force adds up to:¹⁹⁹

$$F_{es} = -\frac{1}{2} \frac{\partial C}{\partial z} U^2(t) = F_{dc} + F_{\omega_{ac}} + F_{2\omega_{ac}}, \text{ with}$$

$$F_{dc} = -\frac{\partial C}{\partial z} \left[\frac{1}{2} (U_{dc} - U_{CP})^2 + \frac{1}{4} U_{ac}^2 \right],$$

$$F_{\omega_{ac}} = -\frac{\partial C}{\partial z} (U_{dc} - U_{CP}) U_{ac} \sin(\omega_{ac} t),$$

$$F_{2\omega_{ac}} = +\frac{\partial C}{\partial z} \frac{1}{4} U_{ac}^2 \cos(2\omega_{ac} t),$$

with ΔC being the capacitance gradient between tip and sample.

Once the contact potential is compensated ($U_{dc} = U_{CP}$), the first harmonic term $F_{\omega_{ac}}$ is canceled to zero. F_{dc} causes an additional force resulting in a permanent shift of $\Delta\omega$ and a static bending of the cantilever, whereas $F_{2\omega_{ac}}$ can be used for capacitance spectroscopy at $2\omega_{ac}$.^{199,200}

The first harmonic can now be followed by the application of lock-in detection at the frequency ω_{ac} . In the amplitude modulation (AM) detection,^{195,197,201,202} the frequency ω_{ac} is chosen to be the second harmonic excitation of the cantilever. This results in a very sensitive resonant detection and only small amplitudes U_{ac} of roughly 100 meV are required.^{195,203}

The experiments have been performed by Thilo Glatzel at the Hahn-Meitner-Institute (Berlin, Germany). The KPFM is based on a commercially available omicron AFM/STM, which is operated in UHV at pressures lower than 10^{-10} mbar. The topographic signal is detected using the frequency modulation (FM) technique (shift of resonance frequency), whereas the contact potential is measured by AM-KPFM (see above). The work function of the cantilever is calibrated using Highly Oriented Pyrolytic Graphite (HOPG) as sample. The HOPG sample itself was calibrated in comparison with several metals. Thus the work function of the cantilever is known and hence the work function of the evaluated sample can be determined by adding the cantilevers work function and the contact potential U_{CP} .

2.4.5. Scanning Near-Field Optical Microscopy (SNOM)

The Scanning Near-Field Optical Microscope (SNOM) applies a tapered drawn optical fiber as scanning probe for local illumination of areas smaller than the optical wavelength of the light. SNOMs can be operated in many different modes, e.g. the fiber is used for both purposes light emission and collection, but here only one possible configuration, the aperture SNOM, will be discussed. The system used for investigations was the Aurora II from ThermoMicroscopes (Sunnyvale, CA). The commercially available tips are covered with a thin aluminum over-layer, so that no light was emitted through the sidewalls at the tapered end of the tip. A schematic of the light out-coupling is shown in Fig. 4.4.5.1.

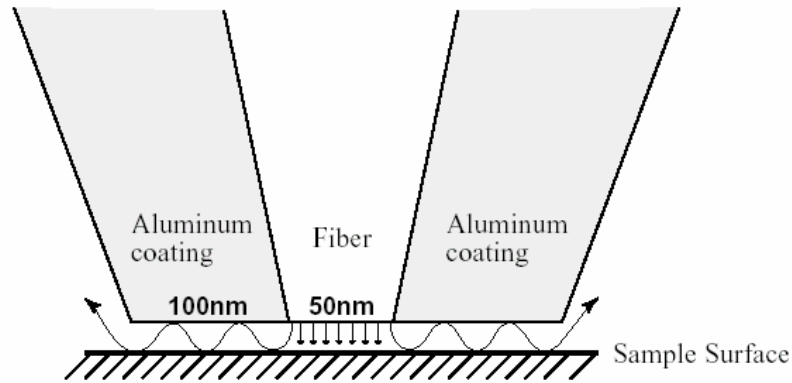


Fig. 2.4.5.1: Tapered end of optical fiber used for illumination of sub-wavelength regions. The distance between tip and sample has to be only a few nm, so that the evanescent wave of the light may couple from the tip to the sample.

Classically light having a wavelength of 500 nm can not be transferred through a hole of only 50 nm, but if the exponentially decaying evanescent wave of the light is used, the light may couple to a very closely adjacent medium. This effect belongs to the near-field optics, giving the instruments name.

To control a constant tip sample distance, the tip is oscillated parallel to the substrate – unlike NC or tapping mode, where the oscillation is orthogonal to the sample surface. This technology is called tuning fork and is illustrated in Fig. 4.4.5.2.

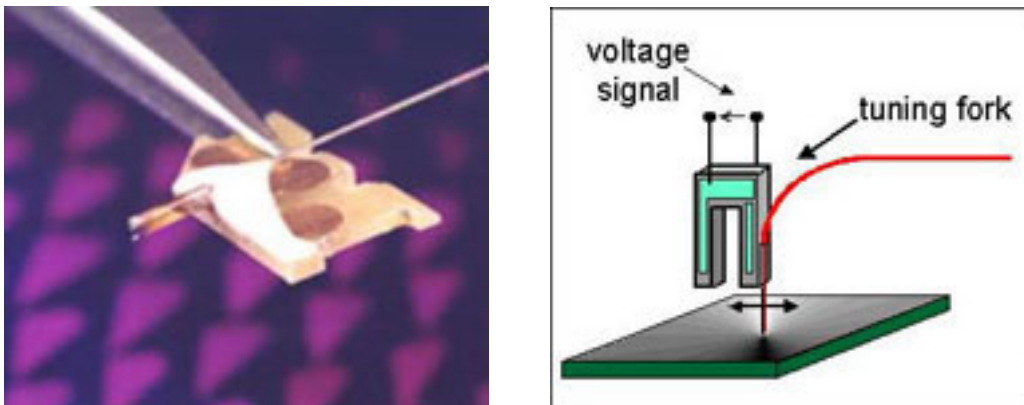


Fig. 2.4.5.2: The fiber tip is mounted onto a quartz tuning fork (left). The voltage signal generated by the quartz tuning fork is directly related to the amplitude of fiber tip oscillation (right).

Usual tip-sample distances are about 5 nm and the lateral amplitude of oscillation extends through some few nm. Since the lateral amplitude remains considerably smaller than the

aperture of the tip, the resolution of collected information corresponds well to the aperture size, typically between 50 – 100 nm.

In the present configuration the SNOM can be driven in two modes: transmission and reflection, where the respective light is collected by far-field collection lenses. A schematic of the optical setup of the Aurora II system is presented in Fig. 2.4.5.3.

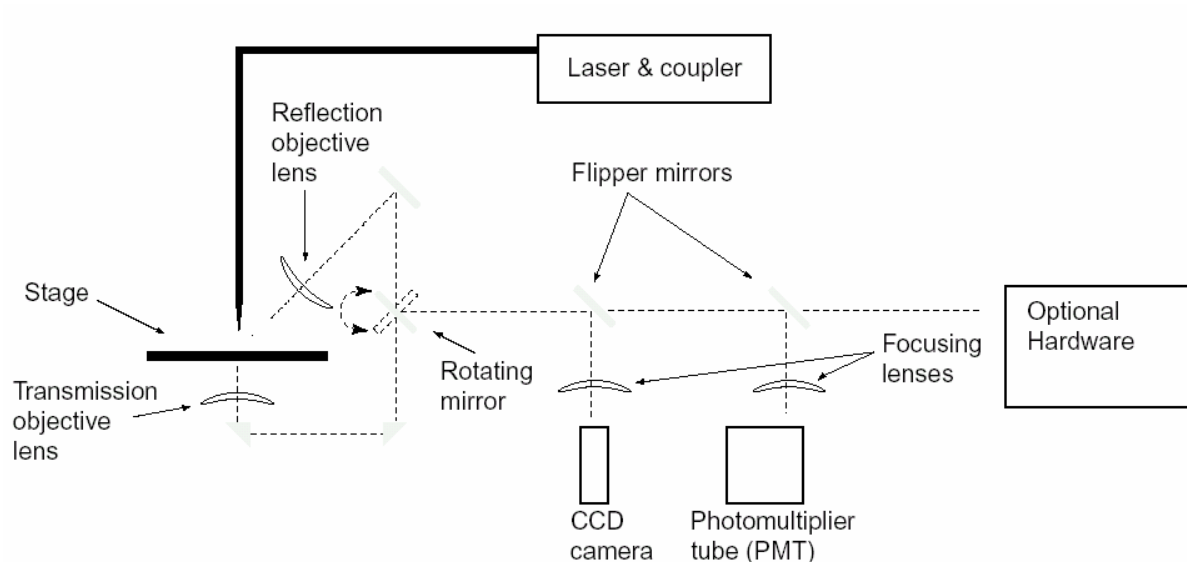


Fig. 2.4.5.3: Optical light path of the Aurora II system. As light source an Argon-ion laser at 488 nm was used at typically 150 – 250 mW output power. Two modes of operation, transmission and reflection, are implemented. The alignment of the system is done with a CCD camera, whereas a photomultiplier tube (PMT) is used for light collection.

As light source an Argon-ion laser at 488 nm with approximately 150 – 250 mW output was used commonly. The collection of the transmitted or reflected light in the measurement was done with a photomultiplier tube. The system allows the simultaneous collection of topography and SNOM data.

2.5. Photoluminescence Measurements (PL)

Photoluminescence spectra of thin films on glass were measured at room temperature at a dynamic vacuum ($p < 10^{-5}$ mbar). The samples were excited with an Ar^+ laser at 476 nm with 40 mW on a spot size of ~ 4 mm in diameter. The excitation beam was chopped with a frequency of 41 Hz. The reflected PL signal was dispersed by a monochromator, detected by a corrected silicon detector and readout by a lock-in-amplifier.

3. Results and Discussion

The jump up in power conversion efficiency of MDMO-PPV:PCBM based plastic solar cells on changing the casting solvent from toluene to chlorobenzene, reported by Shaheen et al.,⁶³ has triggered the present study on differences in the underlying nanomorphology inside these photoactive blends. The scope of this study aims for the ultimate discrimination between MDMO-PPV and PCBM based phases inside the solid-state blend and the molecular order therein. As a first step to differentiate between chlorobenzene and toluene cast blends, AFM tapping mode measurements were performed to study the film topography. The results of which are presented in Fig. 3.1.

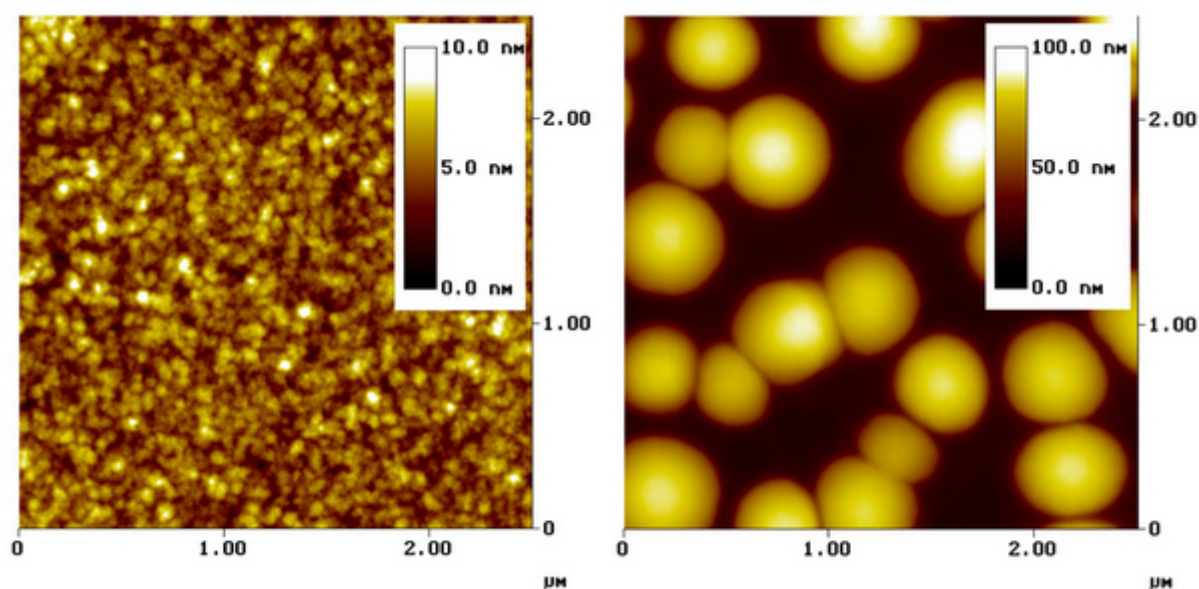


Fig. 3.1: AFM topography scans of MDMO-PPV:PCBM 1:4 (by weight) blended films, spin cast from chlorobenzene (left, 1.4 wt.-%) and from toluene solution (right, 1wt.-%). The toluene cast film shows a tenfold increased height variation as compared to the chlorobenzene cast one. Features of a few hundred nanometers in width are visible in the right, while features at the left are well below 100 nm. The scan size is 2.5 μm in both cases.

It should be pointed out that the height variation profile increases from 10 nm for chlorobenzene up to more than 100 nm for toluene spin cast films. In the case of toluene cast films the average grain reaches a width of a few hundred nanometers, whereas features in the chlorobenzene cast film are well below 100 nm in size. As will be shown below, these grains are PCBM clusters, and their size strongly depends on the ratio of PCBM to MDMO-PPV and on the solution concentration.

By means of scanning near-field optical microscopy (SNOM or NSOM), the topographical features of the chlorobenzene and toluene cast blends could be reproduced (compare Fig. 3.2b & d). However, since the tip radius of curvature is about one order of magnitude larger than for AFM, features were increased in the lateral extension for chlorobenzene cast blend films.

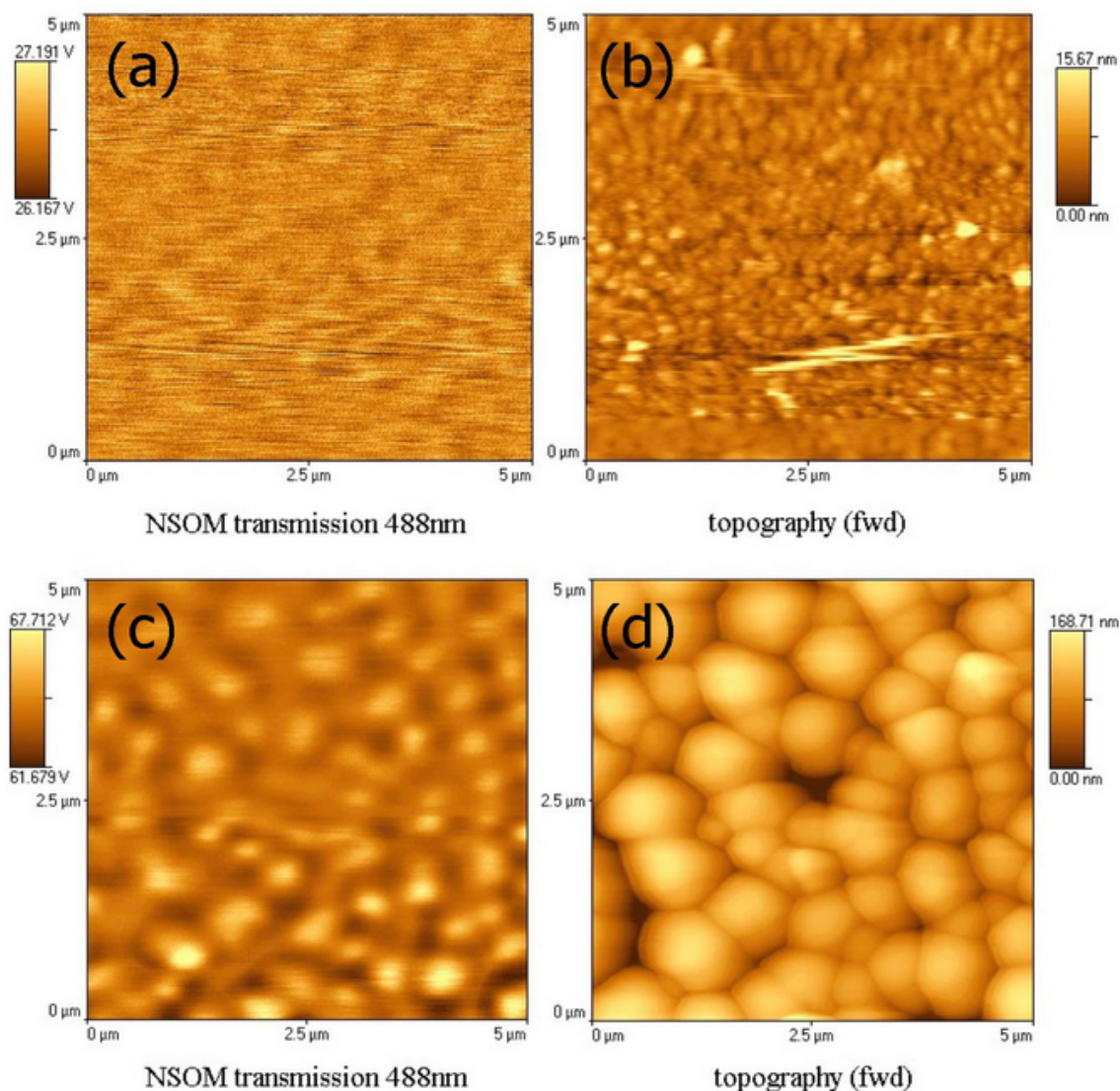


Fig. 3.2: Near-field scanning optical microscopy (NSOM) on chlorobenzene (a, b) and toluene (c, d) spin cast MDMO-PPV:PCBM 1:4 (1.5wt.-%) solar cell blends. The NSOM transmission data is on the left (a, c), whereas the topographical images are on the right (b, d).

The NSOM transmission signal correlates well with the topography of the toluene cast film, but exhibits no clear features for the chlorobenzene cast film. This can be attributed to the limited resolution of the NSOM-tip, as the features in chlorobenzene cast films are of comparable size or even smaller than the tip aperture. Interestingly the NSOM transmission is

not only increased on top of the fullerene clusters using 488 nm laser light, but also by using 690 nm (compare Fig. 3.3). Whereas MDMO-PPV absorbs stronger at 488 nm than PCBM, at 690 nm the situation is reversed. Therefore the same behavior of the NSOM transmission at both wavelengths does not allow discriminating the underlying material and it is indicated that the increased transmission should be due to artifacts. The reflection NSOM-signal reproduced basically the topographical image (Fig. 3.4), which again points to artifacts in the signal.

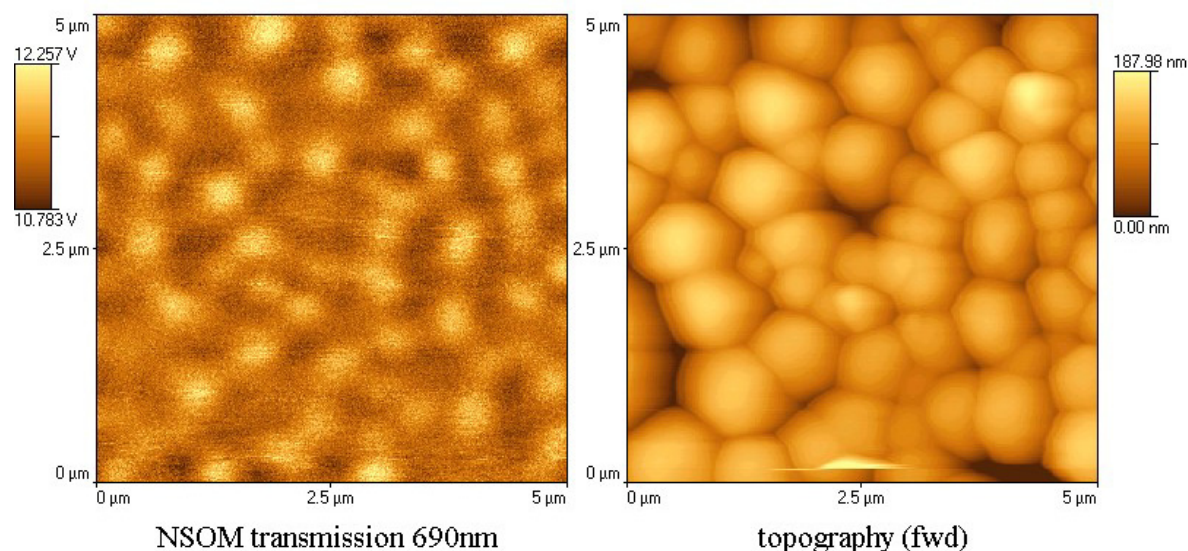


Fig. 3.3: NSOM transmission at 690 nm (left) and topography (right) of films of MDMO-PPV:PCBM 1:4 (1.5wt.-%) blends spin cast from toluene.

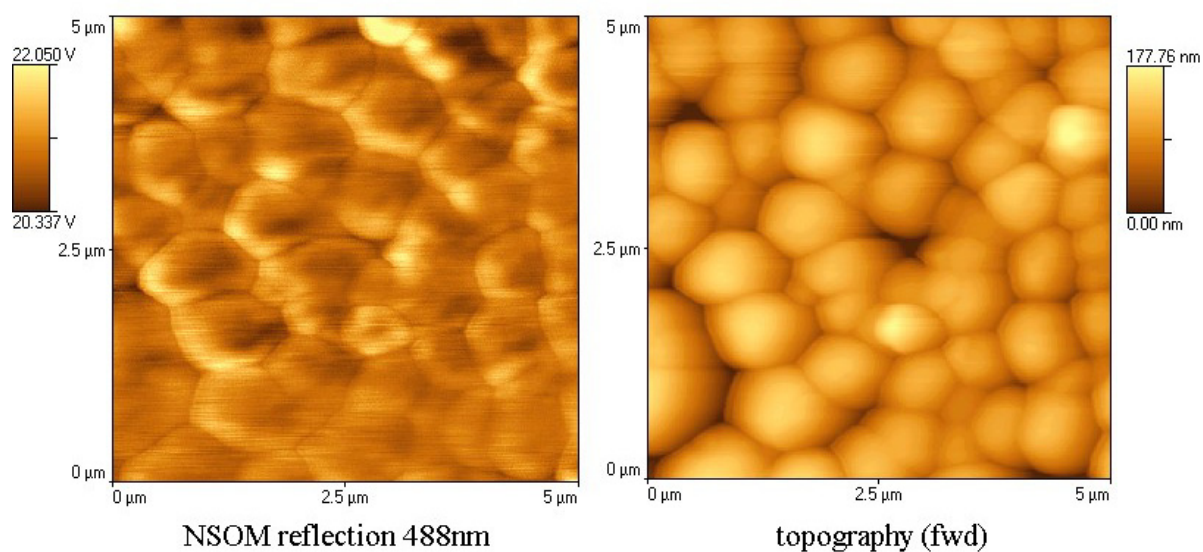


Fig. 3.4: NSOM reflection at 488 nm (left) and topography (right) of films of MDMO-PPV:PCBM 1:4 (1.5wt.-%) blends spin cast from toluene.

3.1. Solar Cell Devices

Bulk-heterojunction solar cells were prepared with different weight ratios between MDMO-PPV and PCBM ranging from 1:1 up to 1:6 using toluene and chlorobenzene as solvents. The devices were characterized by current-voltage and spectral photocurrent measurements. The results for the basic device parameters at 80 mW/cm² white light from solar simulator are shown in table 1 (toluene) and table 2 (chlorobenzene).

Ratio	I _{SC} [mA/cm ²]	FF	V _{OC} [V]	η [%]
1:1	0.93	0.36	0.87	0.36
1:2	1.46	0.46	0.84	0.68
1:3	1.49	0.48	0.82	0.72
1:4	1.49	0.49	0.82	0.74

Table 1: Device parameters for toluene cast active layers at 80 mW/cm² white light. Solutions are of different PCBM content but of equal polymer concentration of 0.33wt.-%.

Ratio	I _{SC} [mA/cm ²]	FF	V _{OC} [V]	η [%]
1:2	1.89	0.44	0.85	0.86
1:4	3.03	0.5	0.84	1.59
1:6	2.54	0.36	0.78	0.89

Table 2: Device parameters for chlorobenzene cast active layers at 80 mW/cm² white light. Solutions are of different PCBM content but of equal polymer concentration of 0.35wt.-%.

In the case of toluene cast films generally lower photocurrents are observed, resulting in lower power conversion efficiencies as compared with chlorobenzene based devices. On the other hand the open circuit voltage and the filling factors are of comparable magnitude. Upon increasing the PCBM concentration in toluene blends the photocurrent becomes saturated.

For chlorobenzene cast films, the short circuit current reaches a maximum around 80wt.-% PCBM. Once the PCBM concentration is increased beyond that to about 86wt.-%, the photocurrent decreases again. This may be a result of decreasing the interfacial D/A area and of losing percolation for hole transport through the bulk of the active layer (compare with Fig. 3.1.8, 1:6).

The results from spectral photocurrent measurements are presented in Fig. 3.1.1. They reconfirm, that the currents from chlorobenzene cast films are generally higher than those from toluene cast films. In addition the signature of the PCBM absorption (compare 206) becomes more visible for increasing PCBM contents between 600 and 650 nm, clearly demonstrating the contribution of PCBM absorption to the photocurrent.

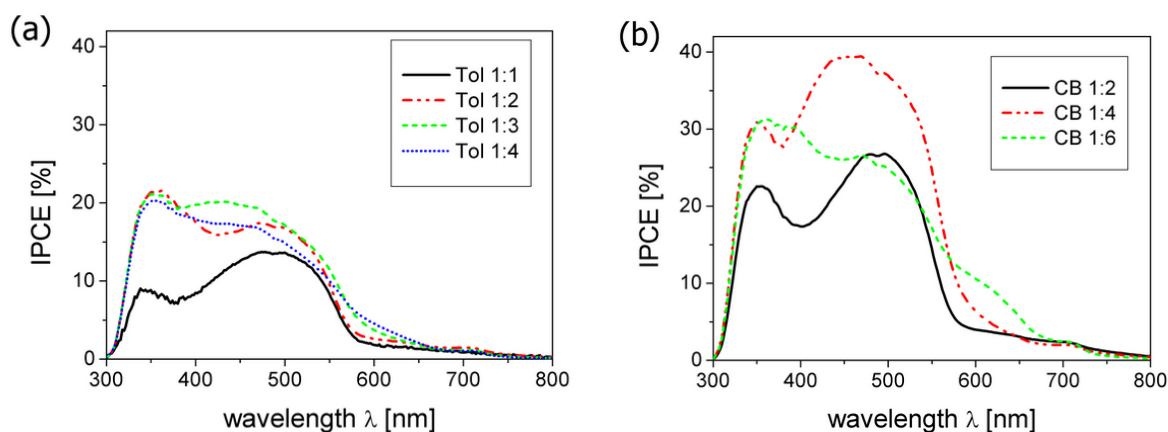


Fig. 3.1.1: Incident photon to collect electron (IPCE) spectra of solar cell devices with active layers of different MDMO-PPV:PCBM mixing ratios (a) cast from toluene (compare with Fig. 3.1.2) and (b) cast from chlorobenzene (compare with Fig. 3.1.8).

The constant polymer concentration in the respective toluene or chlorobenzene solutions in combination with the constant spinning frequency should result in the deposition of very comparable amounts of MDMO-PPV in the films. Therefore the signature of the MDMO-PPV absorption in the IPCE spectra should reflect the ability of the present device to charge separate and transport the current through the active layer. Note that the IPCE spectra of toluene cast blends are lower throughout the measurement range than chlorobenzene cast blends.

3.2. Nanomorphology

To investigate the nanomorphology of the active layer of the solar cells, a series of films spin cast from different weight ratios of polymer to fullerene content in toluene solutions were studied with SEM. The solutions were the same as used for the solar cell devices and the MDMO-PPV concentration in the different solutions was kept constant at 0.33wt.-%. In Fig. 3.2.1 the top views of toluene cast films, having mixing ratios of 1:1, 1:2, 1:3 and 1:4 of

polymer to fullerene content (by weight) are shown. With decreasing PCBM content, the nanoclusters become smaller until they are no longer observable in the case of the 1:1 blend.

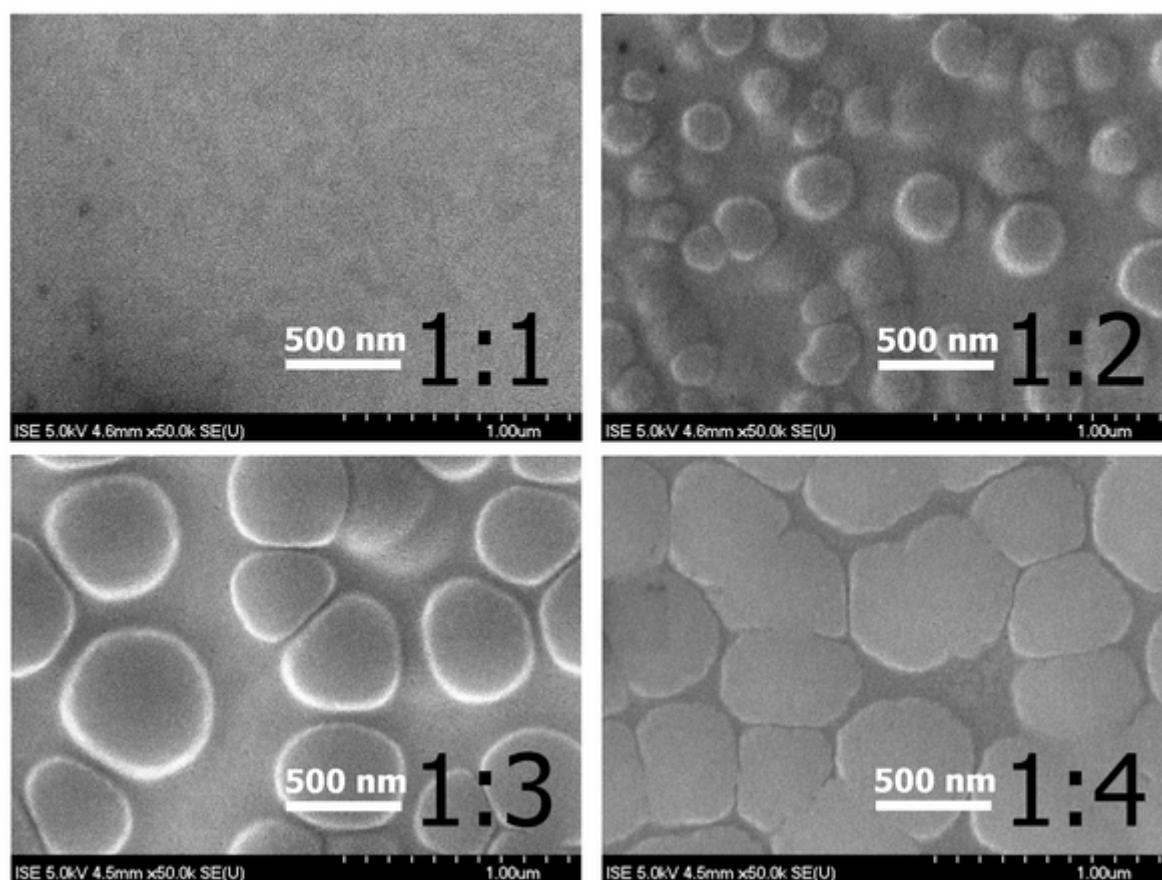


Fig. 3.2.1: Top view of toluene based films with varying mixing ratios of MDMO-PPV and PCBM (by weight) contents measured by SEM. The magnification chosen is 50 000 for all images. The surface of the film with 1:1 mixture looks flat and shows no features any more. For the films with larger PCBM-content round shaped domains i.e. “nanoclusters” are visible, increasing in size for increased PCBM content. Due to the high PCBM content in the film having the 1:4 ratio, the clusters loose their round shape as they touch each other on several borders.

To gain insight into the nanostructure within the films, the samples were broken, covered with a thin layer of platinum and then the cross sections were imaged by SEM. In Fig. 3.2.2 the cross sections of the same films as in Fig. 3.2.1 are shown. Here it becomes clearly observable, that in heavily PCBM loaded films the nanoclusters are generally covered by another “skin” layer of approximately 20 – 40 nm thickness. The shape of the nanoclusters is somewhat flattened, forming a kind of discs, as their radius exceeds the film thickness. For the 1:1 blend little nanospheres are embedded within a rather homogeneous matrix. They have

a much smaller diameter (about 20-30 nm) than the film thickness and hence do not affect the top view scans. These little nanospheres are also found around the bigger nanoclusters within the skin layer.

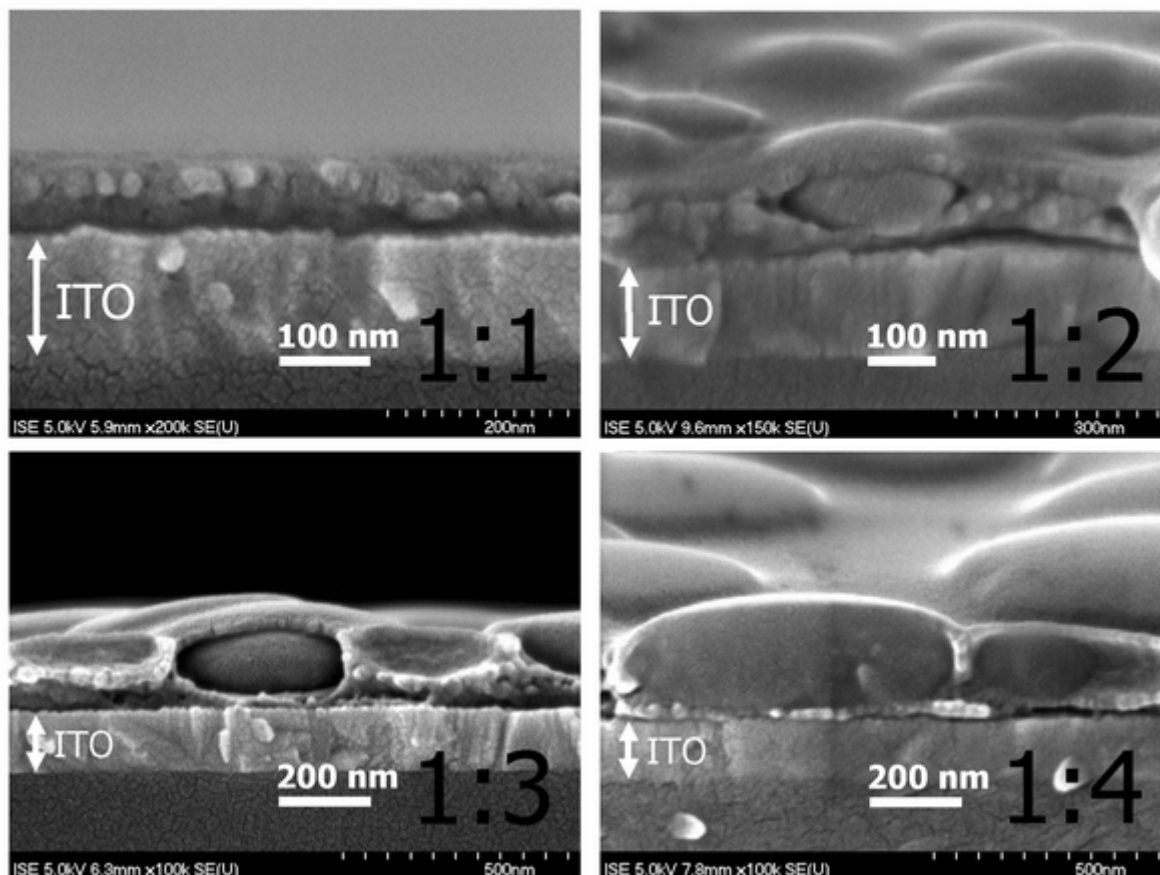


Fig. 3.2.2: Side view of the cross section of MDMO-PPV:PCBM blended films cast from toluene with varying mixing ratios (by weight). For the ratios 1:4, 1:3 and 1:2 the nanoclusters in the form of discs are surrounded by another phase, i.e. skin, that contains smaller spheres of about 20-30 nm in size. For the 1:1 mixing ratio only these smaller spheres are found. The magnifications used are 100 000 (1:4 and 1:3), 150 000 (1:2) and 200 000 (1:1).

To investigate the effect of drying time onto the evolving film morphology, spin cast and drop cast samples from toluene solution are compared (Fig. 3.2.3). Larger and coalesced structures are found for the case of drop cast samples (Fig. 3.2.3b), clearly demonstrating the dynamic process of phase separation under the presence of solvent.

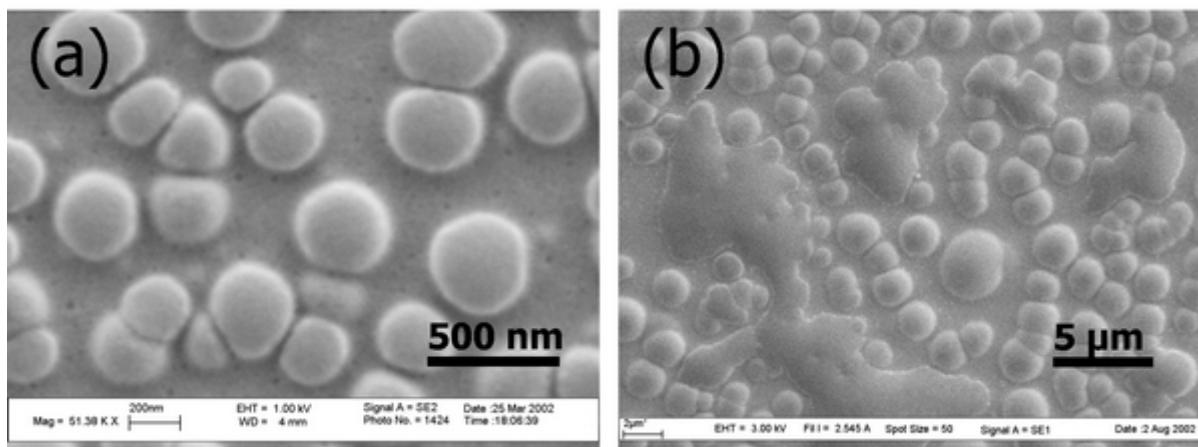


Fig. 3.2.3: Comparison between a spin-cast (a) (1:3, 1wt.-% in solution) and a drop-cast (b) (1:4, 1.5wt.-% in solution) film of MDMO-PPV mixed with PCBM in toluene solution. The clusters in the spin-cast film do not coalesce, while for the drop-cast film extended coalescence is visible. Note that the magnification of (a) is about one order of magnitude larger than that of (b).

Solutions of different concentrations, but with constant mixing ratios of 1:4 of MDMO-PPV and PCBM, have been prepared and spin cast under standard conditions. Here the summated polymer and fullerene content in the solutions are ranging from 0.50wt.-% up to 1.50wt.-%, which corresponds to 0.10wt.-% to 0.30wt.-% concentrations of MDMO-PPV in the solution. AFM scans reveal that the fullerene cluster size (Fig. 3.1.4) as well as the average film thickness is increased on increasing total concentration.

Therefore the extent of phase separation does not only scale with increasing fullerene fractions but also with an increasing total concentration of the fullerene in solution. The observed increase in phase separation allows two possible explanations: either the clusters are already present in the casting solution or they are developed dynamically during the film formation. To investigate this, a study with a more extended concentration regime was carried out. The results from AFM tapping mode measurements and optical microscopy are summarized in Figs. 3.2.5 and 3.2.7.

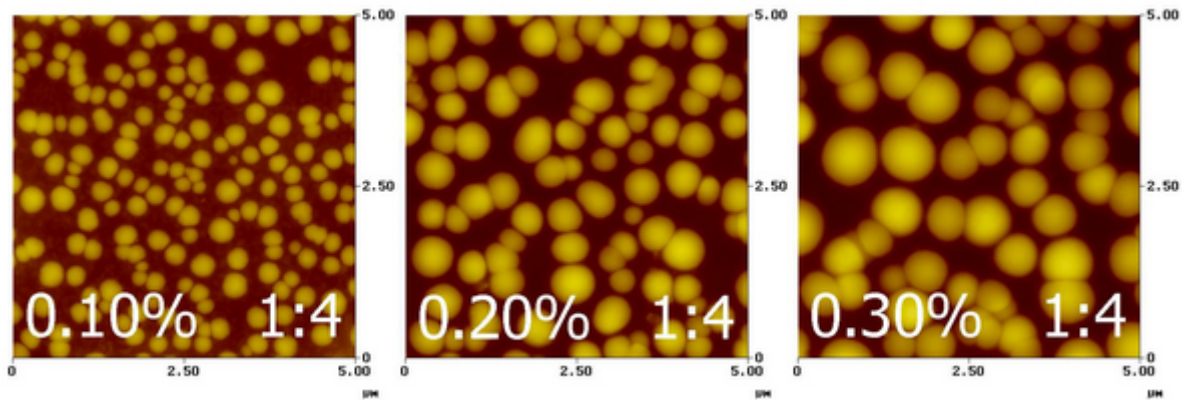


Fig. 3.2.4: AFM-scans of spin cast films with the same mixing ratio between MDMO-PPV and PCBM (1:4 by weight), but with different total concentrations in the precursor toluene solution. Increasing the total concentration from 0.50wt.-% up to 1.50wt.-% (corresponding MDMO-PPV conc. of 0.10wt.-% to 0.30wt.-%) results in a strong increase of the PCBM cluster sizes. Scan size is $5\ \mu\text{m} \times 5\ \mu\text{m}$, z-ranges are 100nm, 150nm and 200nm (left to right).

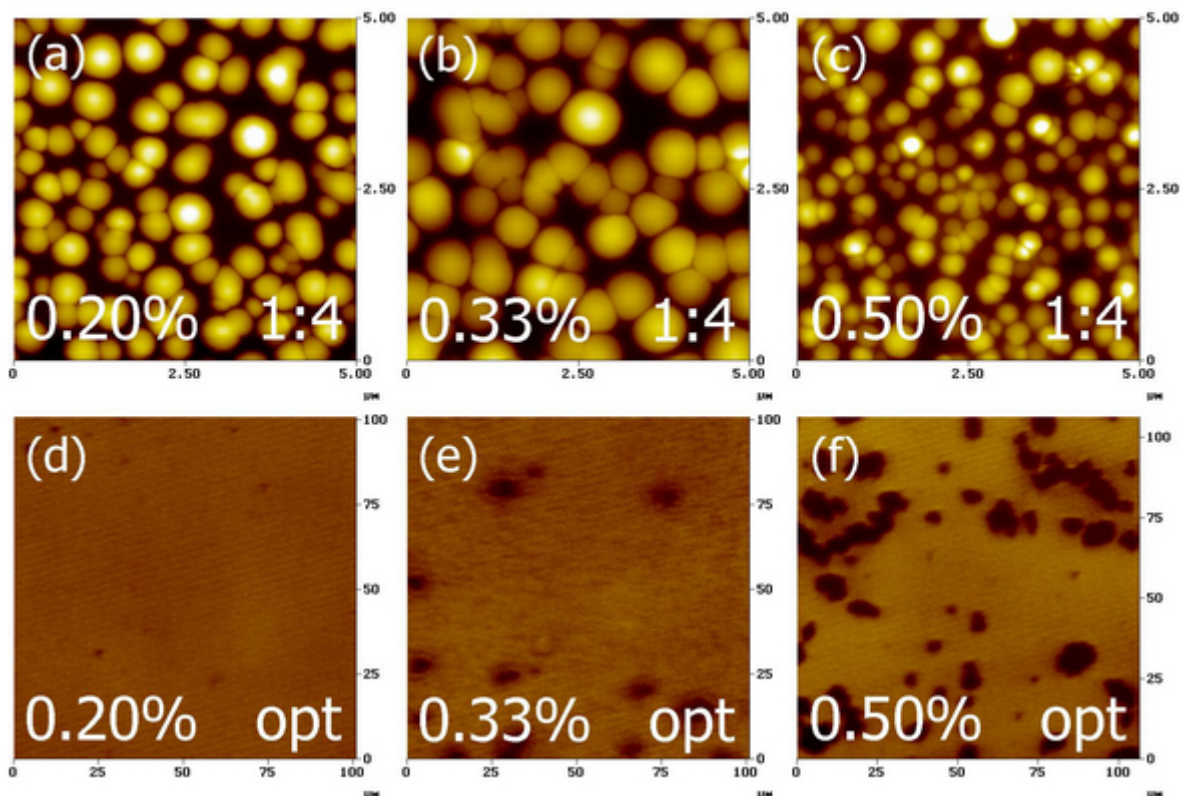


Fig. 3.2.5: Study as in Fig. 3.1.4, but with an extended range of concentrations in precursor toluene solutions, (a-c) AFM and (d-f) optical images. Whereas 1.00wt.-% and 1.66wt.-% compare well to earlier results, a total 2.50wt.-% results in a reduced dimension of phase separation. Scan sizes are in all cases $5\ \mu\text{m} \times 5\ \mu\text{m}$, z-ranges are 100nm, 150nm and 100nm (from (a) to (c)). The corresponding optical images (d-f) give information about the amount of precipitated PCBM. (Concentration shown in the image corresponds to MDMO-PPV.)

Interestingly the trend of increasing cluster sizes, observed in the concentration regime between 0.5wt.-% and 1.5wt.-%, is reversed for concentrations as high as 2.5wt.-%. Here it should be noted that for this high concentration corresponding to 0.5wt.-% MDMO-PPV in toluene, the solution becomes notably viscous. From the optical images in Fig. 3.2.5 the amount of precipitated PCBM can be estimated. At higher concentrations there is a larger amount of precipitated PCBM observed, according to the independently determined solubility of 1wt.-% PCBM in toluene (see below). It should be noted that for all studies performed no filtering of solutions was applied, to guarantee the authenticity of the solution concentration quoted. For example in the case of 2.5wt.-% total concentration it can be expected that the mixing ratio in the solution would be altered considerably due to filtering. However, since the precipitated fullerene is visible in the optical images it is clear that the mixing ratio in the film is different from that prepared.

From independent optical measurements on PCBM solutions, the solubility of PCBM was determined to be roughly 1% in toluene and 4.2% in chlorobenzene. This result was achieved by setting up solutions of roughly 8wt.-% and 4wt.-% in chlorobenzene and toluene respectively. Then the solutions were stirred for several days, which was followed either by an idle period of the solution in the shelf or by the application of a centrifuge. Thereby the non-dissolved PCBM could precipitate. The resulting saturated PCBM solutions were diluted in a series and compared to independently prepared solutions of 1wt.-% PCBM. The different solubility of PCBM in toluene and chlorobenzene is illustrated by a photographic image of diluted (1:50) saturated solutions in Fig. 3.2.6.

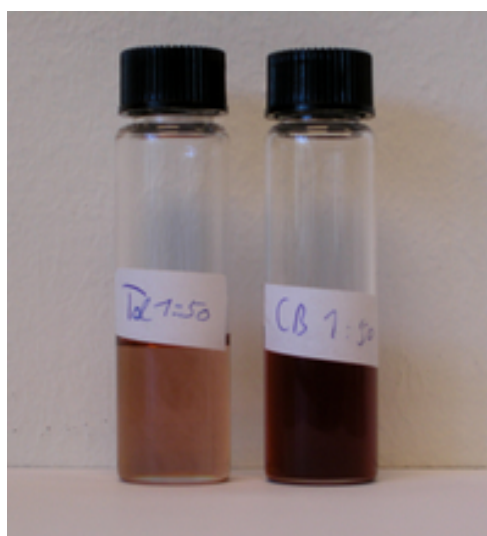


Fig. 3.2.6: Dilutions (1:50) of saturated PCBM solutions in toluene and chlorobenzene.

According to the supplier¹⁸⁸ MDMO-PPV is not limited in the solubility over the range studied here, but rather the solution viscosity will limit the application of concentrations beyond 1wt.-%.

To investigate the influence of spinning frequency on the resulting morphology, films were spin cast at a high spin frequency of 6000 rpm (compare Fig. 3.2.7 (c, f)). Clearly the mean size of the observed clusters is reduced, and the homogeneity in cluster size seemed to be similar or even better. Therefore it is reasonable to assume that the phase separation is not present in the solution, but develops during film deposition. To affirm this argument, films were prepared from the same solutions, but the solutions have not been stirred for several hours (Fig. 3.2.7 (b, e)). The sizes of clusters compare well with those obtained in films cast from stirred solutions (Fig. 3.2.7 (a, d)).

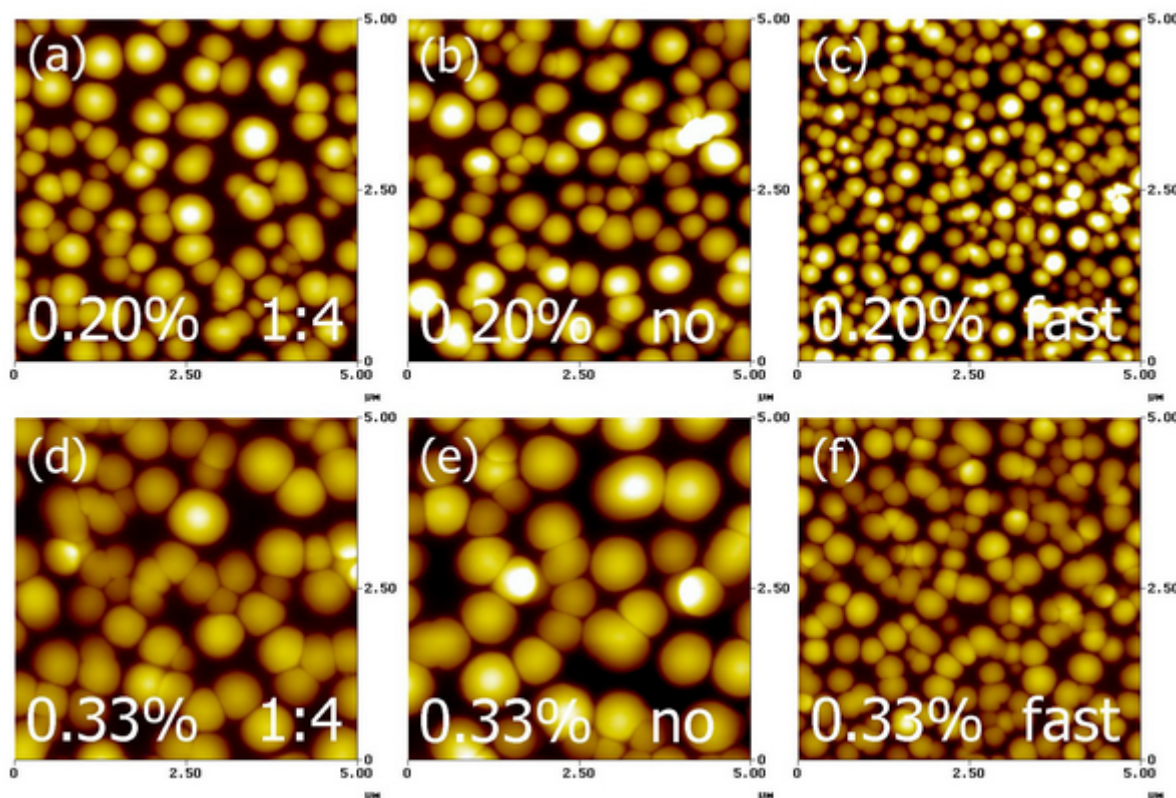


Fig. 3.2.7: Same solutions as in Fig. 3.2.5, but different treatment of the solution (no) or different spinning frequency (fast). Films in images (a-c) were spin cast from 1.00wt.-% solutions, (d-f) were spin cast from 1.66wt.-% solutions. The films shown in (b) and (c) were produced without stirring the solution for several hours prior to casting, whereas the films in scans (c) and (f) were spin cast at 6000 rpm. Scan sizes are in all cases $5 \mu\text{m} \times 5 \mu\text{m}$, z-ranges are 100nm, 100nm and 50nm for (a-c), and 150nm, 150nm and 100nm for (d-f).

As expected, the film thicknesses were smaller for the films spin cast at higher spinning frequency: blends films from 1wt.-% yielded ~95 nm at 1500 rpm and ~66 nm at 6000 rpm, films from 1.66wt.-% resulted in 180 nm and 110 nm, respectively. Hence the observed cluster sizes roughly correlate with the film thickness determined.

Similar to the case of toluene, several chlorobenzene solutions with varying blending ratios of MDMO-PPV and PCBM were prepared. There the polymer concentration was again kept constant at a value of 0.35wt.-%. All films exhibited a flat surface topography, so that SEM images from top views of the films are omitted and only cross-sections of the solar cell devices are shown.

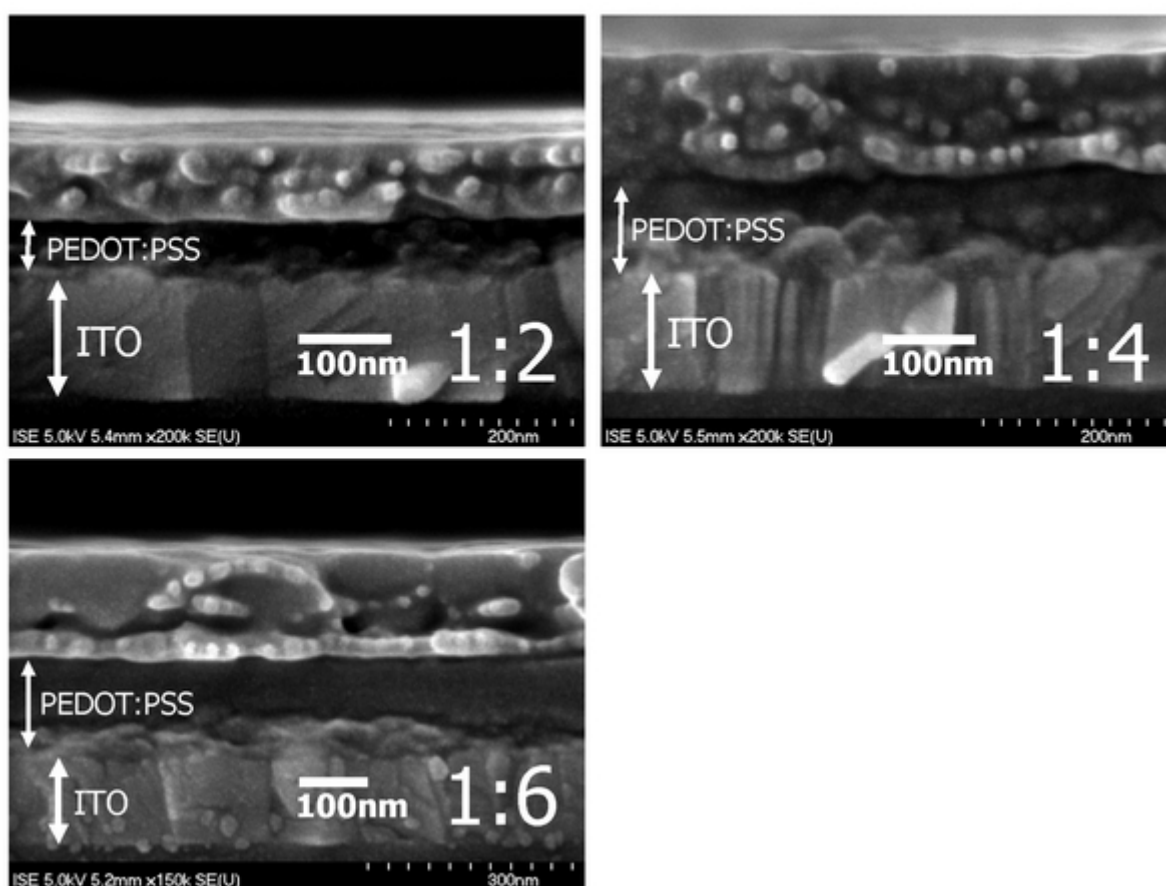


Fig. 3.2.8: Side view of the cross section of MDMO-PPV:PCBM blended films spin cast from chlorobenzene solutions with varying mixing ratios (by weight) of the MDMO-PPV to PCBM on top of PEDOT:PSS coated ITO-glass. In all samples nanospheres of about the same size (~20 nm) are found. The magnifications used are 200 000 (1:2 and 1:4) and 150 000 (1:6).

In Fig. 3.2.8, side view cross sections of the chlorobenzene cast films are shown for mixing ratios of 1:2, 1:4 and 1:6 of MDMO-PPV with PCBM. All of these films appear to be

homogeneous except for some smaller (~20 nm in size) nanospheres, which are dispersed throughout the films. The size of these nanospheres does not change with the PCBM content, but is comparable with those small nanospheres observed also in the toluene cast composite films. Possible cluster sizes have to be much smaller than for toluene cast films. However, for the 1:6 blend larger clusters become observable, while the nanospheres surround them – like in the case of toluene cast films – in a skin layer. Interestingly to mention that also a preferential adsorption of the nanospheres on top of the PEDOT:PSS (poly[3,4-(ethylenedioxy) thiophene] : poly(styrene sulfonate)) anode-layer is found.

It shall be pointed out here that the observed morphology is not unique for the case of MDMO-PPV:PCBM blends, but has also been found for regioregular-P3HT:PCBM blends. A comparison between both cases is shown in Fig. 3.2.9, where both films exhibit mixing ratios of 1:2 conjugated polymer to PCBM.

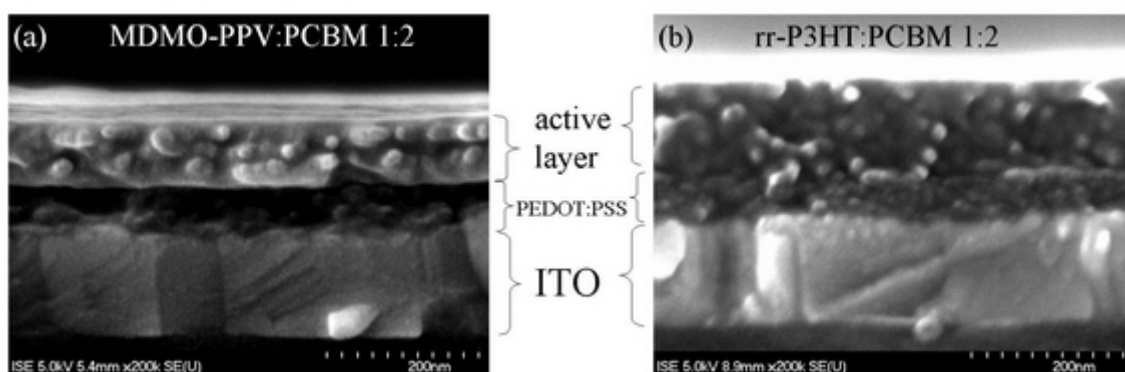


Fig. 3.2.9: Comparison between cross-sections of active layers spin cast from chlorobenzene onto PEDOT:PSS covered ITO-glasses. The active layers based on MDMO-PPV (left) and on regioregular P3HT (right) exhibit similar features. Especially the nanospheres of roughly 20 nm in diameter are clearly visible in both cases.

On a closer inspection of Fig. 3.2.9b, even a granular structure of the PEDOT:PSS layer can be seen. In this case the granules have a diameter that is ≤ 10 nm only (compare ²⁰⁴).

3.3. Identification of Phases

In the previous section it has been shown that with increasing PCBM content in the blends the observed clusters in the toluene cast blends become larger. Thus one can reason that these clusters must presumably consist mainly out of PCBM. Also for chlorobenzene cast films some clustering for high PCBM content (1:6 blend) has been observed. The combination of annealing, AFM, TEM and PL measurements allows for the unambiguous assignment of the clusters to consist out of PCBM, whereas the nanospheres will be identified as MDMO-PPV.

3.3.1. TEM and Electron Diffraction

Thin films of MDMO-PPV, PCBM and blends of both were imaged using transmission electron microscopy (TEM), and selected area electron diffraction (SAED) was used to gain information on the local state of crystallinity. In the following, diffraction images have been inverted, which means that dark regions in the image reflect bright regions on the TEM screen. Also, the central intensity maximum had to be blocked during exposure to protect the CCD camera of the TEM system. This results in a white bar in the inverted diffraction image. Figure 3.3.1.1 shows TEM images of pristine MDMO-PPV and PCBM films.

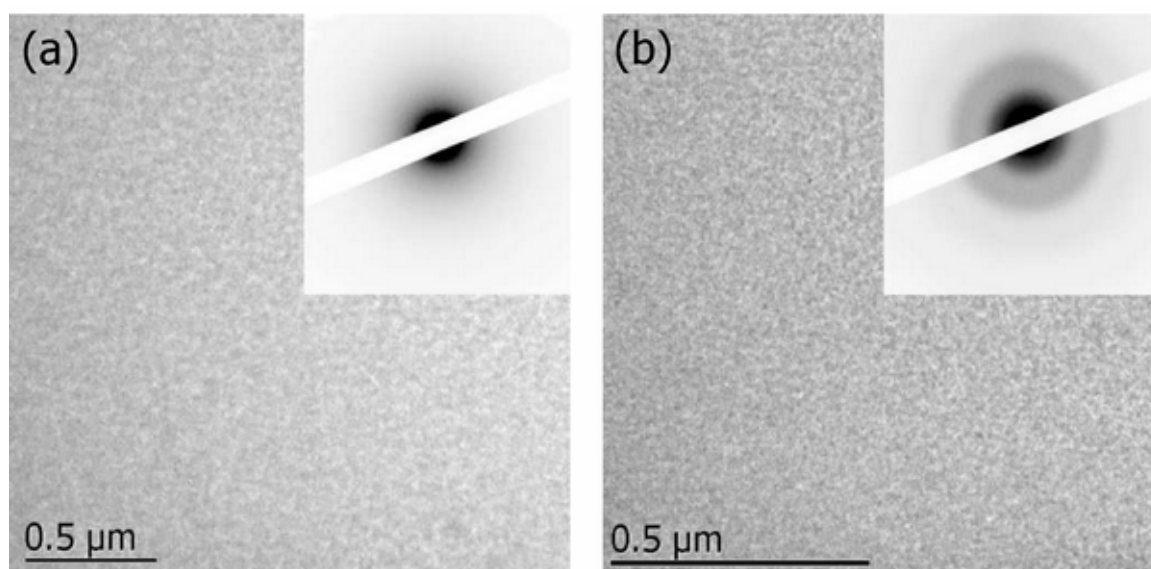


Fig. 3.3.1.1: The MDMO-PPV film spin cast from chlorobenzene (0.25%wt) in (a) exhibits no order and is completely amorphous. The PCBM films (b) spin cast from chlorobenzene (3%wt) yield some fringes in the electron diffraction pattern, thus indicating a multi-crystalline order in the film on the nanometer scale.

Both of the films in Fig. 3.3.1.1 look homogeneous and there are no different phases that can be distinguished. The grainy background is caused by the noise of the CCD camera. The insets show the diffraction pattern of the respective investigated areas. For MDMO-PPV only the central maximum together with the amorphous halo is observed, there are no fringes (Debye-Scherrer rings) or reflexes caused by crystalline order in the material. From this it can be concluded that (within the resolution of the SEAD) the pristine MDMO-PPV film is amorphous. In contrast to MDMO-PPV the diffraction pattern of pristine PCBM film shows regular fringes (inset of Fig. 3.3.1.1b). This is a clear sign of a polycrystalline material. Since TEM allows investigating small areas on the order of 100 nm in diameter of the film, it is clear that the PCBM crystals have to be much smaller than 100 nm.

Blend films spin cast from 1wt.-% chlorobenzene solution (again with the weight ratio of 1:4 between MDMO-PPV and PCBM) are rather homogeneous and exhibit some weak features on the sub 100 nm scale, in agreement with the AFM results. Clearly some fringes are visible in the diffraction image, but the underlying order in the film must be smaller than that of the pristine PCBM films, since the fringes are less pronounced. However, there is some local order of the PCBM molecules (compare Fig. 3.3.1.2).

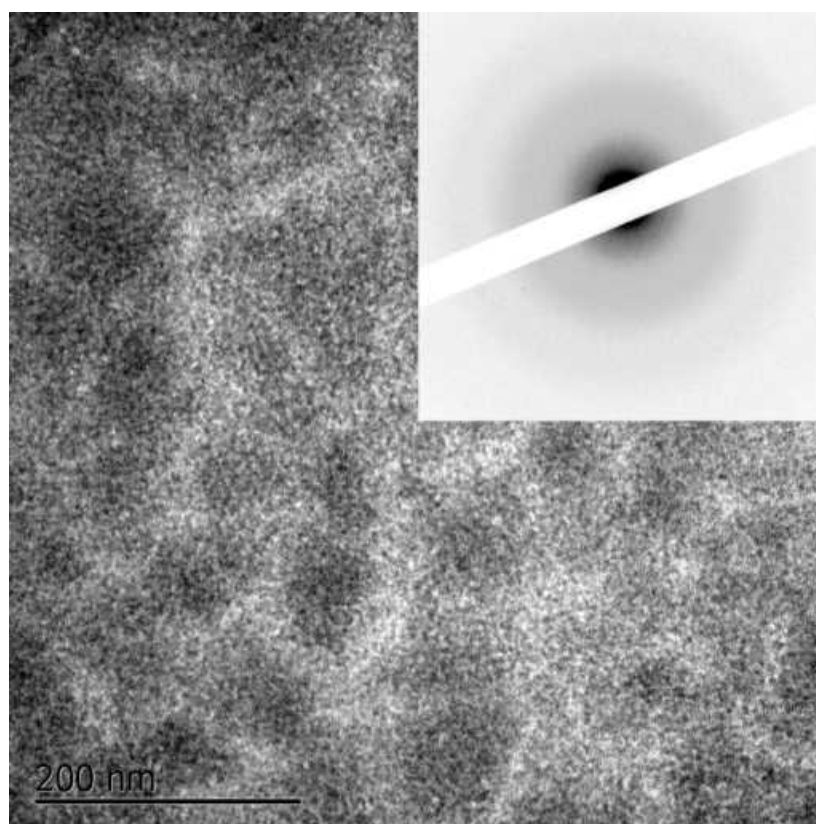


Fig. 3.3.1.2: A blend film of MDMO-PPV:PCBM 1:4 spin cast from chlorobenzene (1wt.-%) yields similar diffraction pattern as found for pristine PCBM films.

Upon casting the blend with the same concentration and composition using toluene as a solvent, again a large-scale phase separation is observed. The round shaped clusters appear dark and are of up to several hundred nm in diameter (Fig. 3.3.1.3). Selected area electron diffraction (SAED) yields fringes for clusters and the surrounding matrix. Thus nanocrystalline PCBM is present in both of the phases observed. There cannot exist a bare MDMO-PPV phase, since bare MDMO-PPV does not exhibit any order in our studies (SAED image in Fig. 3.3.1.1). The diffraction signal in (a) might be weaker than that in (b), since the local film thickness is larger at the cluster sites.

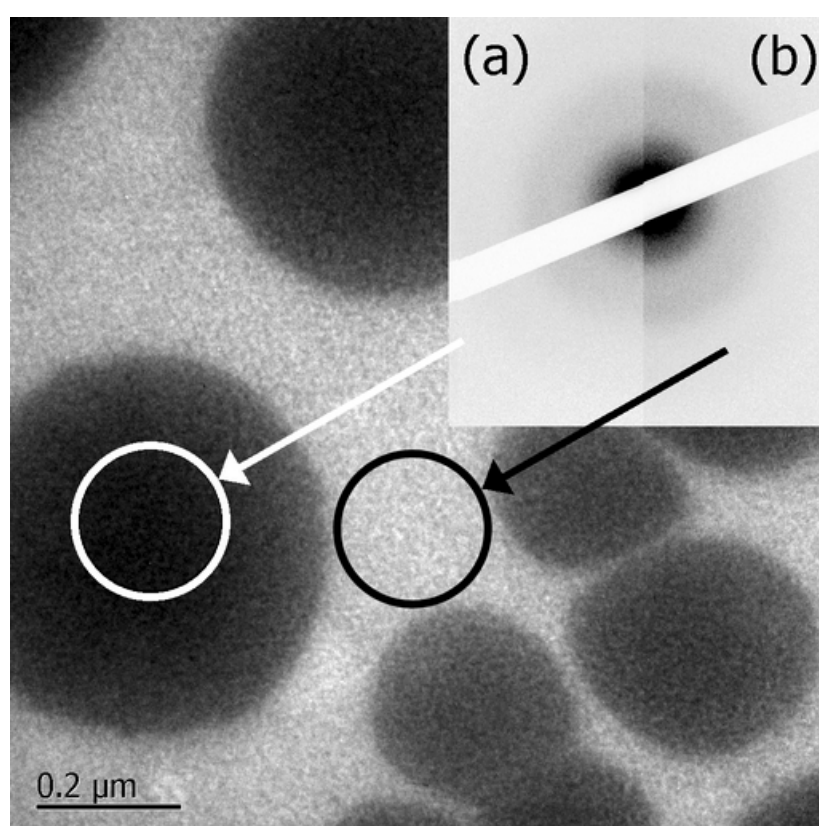


Fig. 3.3.1.3: Blend films MDMO-PPV:PCBM 1:4 spin cast from toluene (1wt.-%) exhibit a larger scale phase separation. Both, the clusters (a) and the area in between (b) the clusters yield fringes in the electron diffraction pattern (inset) for the indicated areas (circles).

3.3.2. Annealing of MDMO-PPV:PCBM Blends

On annealing the toluene cast blend film at about 150°C for 4 hours, larger micron sized aggregates are yielded (compare Fig. 3.3.2.1b). Single crystalline diffraction images could be obtained at places on these aggregates (compare Fig. 3.3.2.1c). Therefore these crystallites

consist out of PCBM. Since they were built by depleting the round clusters, one can conclude further that the clusters are predominantly consisting of PCBM. Now the phase between these crystallites exhibits no sign of any order anymore (Fig. 3.3.2.1d), and it can be concluded that the remnant consists out of MDMO-PPV. Therefore the annealing process results in a true phase separation between MDMO-PPV and PCBM.

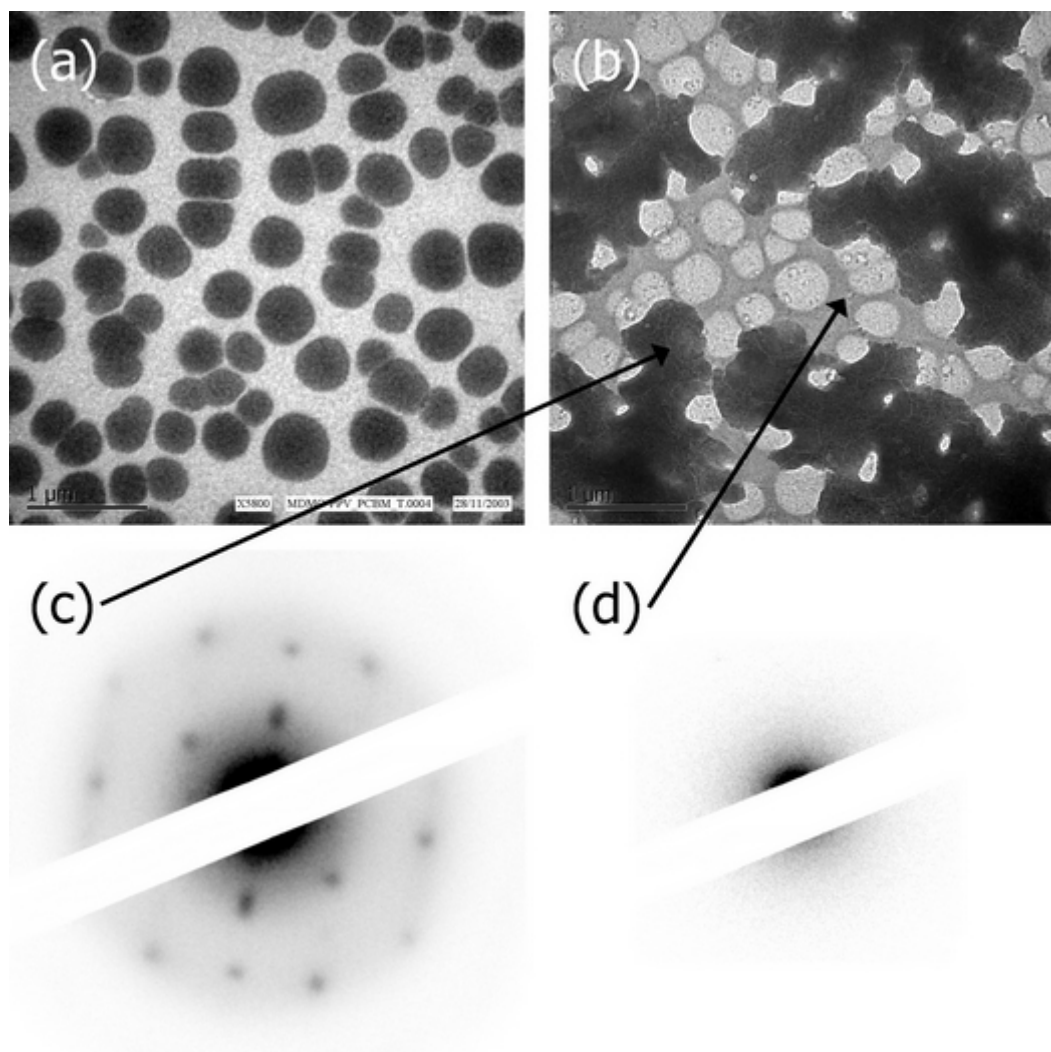


Fig. 3.3.2.1: As cast (a) and annealed (b) blend film of MDMO-PPV:PCBM 1:4 spin cast from toluene (1wt.-%). Large aggregates have formed on the surface of the film during the annealing and thereby the dark PCBM clusters observed in the unheated film were depleted. The large aggregates can produce a single crystalline diffraction image (c), whereas the phase between those crystallites appears to be completely amorphous (d), thus being attributed to the polymer. Therefore the annealing promotes complete phase separation in the film.

Comparison of the diffraction image of the thermally aggregated crystallites with the fringes obtained in the blend films yields good agreement of the radii (Fig. 3.3.2.2). This is a strong

indication that the PCBM in the blend is in form of nano-crystallites that form relatively large crystals during the heat treatment.

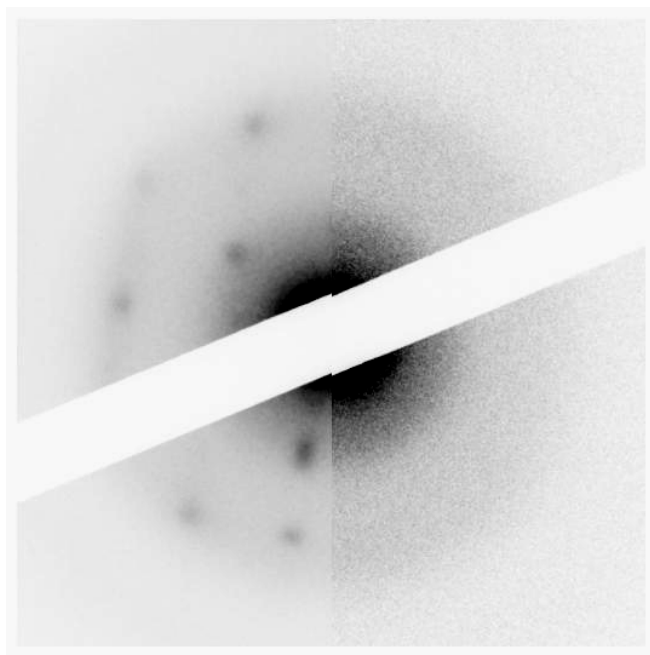


Fig. 3.3.2.2: Comparison of the TEM-diffraction pattern of single crystalline PCBM (left) and multi crystalline PCBM found in the blend films (right) yield good agreement.

For C_{60} single-crystals a face centred cubic (fcc) structure was obtained earlier.²⁰⁵ The unit cell had a lattice constant of $a_0=14.2 \text{ \AA}$, and the center-to-center distance between the C_{60} molecules with a diameter of 7.1 \AA was exactly 10 \AA . If we as well assume an fcc structure for the PCBM crystallites, the fit with the experimental data is satisfactory well and we calculate a lattice constant of about 14 \AA , which is very similar to the C_{60} data of Heiney et al..²⁰⁵ This result is intriguing, since PCBM exhibits some side groups, that don't seem to hinder close crystal packing.

To analyze the evolving structure due to the annealing process in more detail, tapping mode AFM measurements were performed. Spin cast thin films from total 0.50wt.-% toluene solutions and from total 1.40wt.-% chlorobenzene solutions (both with the ratio 1:4) have been studied in combination with annealing at temperatures around $145(\pm 5)^\circ\text{C}$. In Fig. 3.3.2.3, AFM images for different annealing times, ranging from several minutes to a few hours, are depicted for toluene and for chlorobenzene cast films.

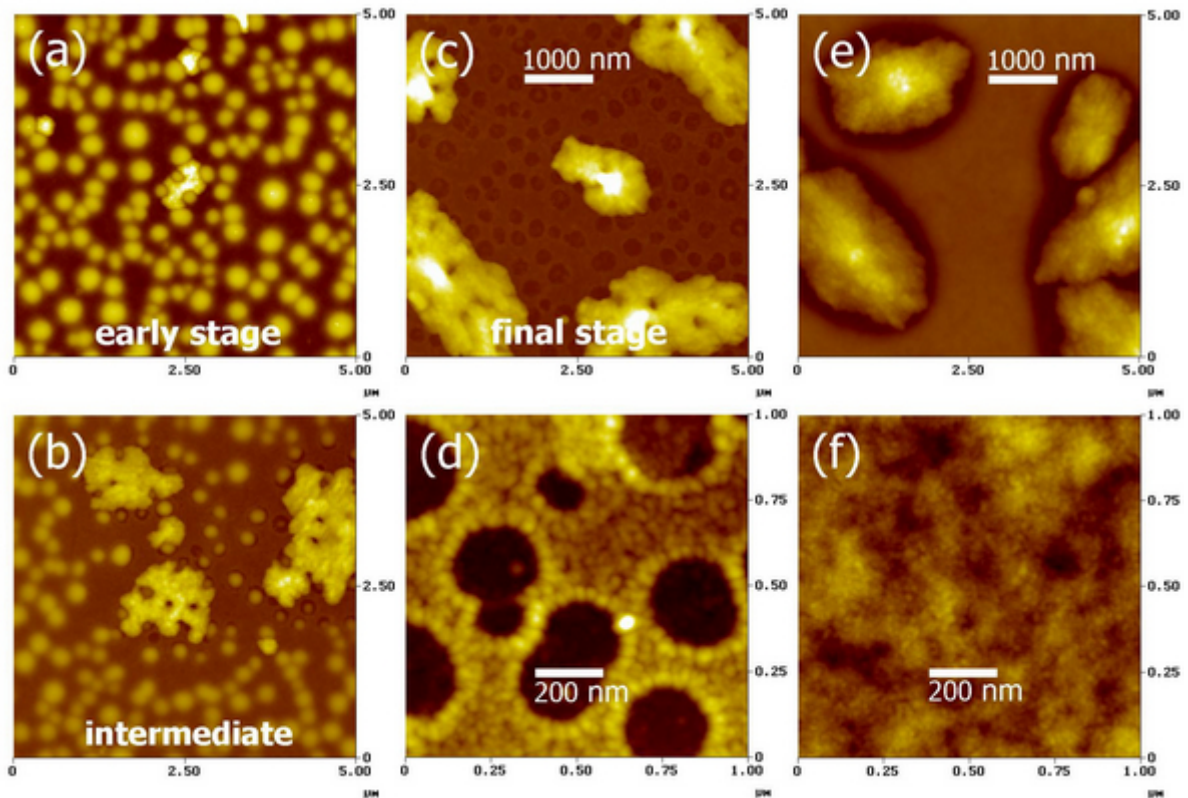


Fig. 3.3.2.3: Topography of 0.50wt.-% 1:4 toluene (a-d) and 1.40wt.-% 1:4 chlorobenzene (e-f) based annealed films. For increasing annealing times (a-c), larger and larger crystalline aggregates are formed depleting surrounding clusters. In magnification (d) at the end of that annealing process, holes are left over where PCBM-clusters have been before. For the blend spin cast from chlorobenzene, the same crystallites appear, but they seem to be grown more continuously in comparison with the toluene case. Note that the process in (e) is not completed, since in (f) (magnification of (e)) the originally flat film topography between the large crystallites is quite preserved. In (d) the framework consists of about 30-40 nm large spheres in close agreement with the nanospheres found in the SEM-images of the cross sections. Scan sizes are $1 \mu\text{m} \times 1 \mu\text{m}$ for (d) and (f), else $5 \mu\text{m} \times 5 \mu\text{m}$. Z-ranges are 100nm, 200nm, 300nm, 25nm, 300nm and 15nm for (a) to (f) respectively.

Due to the annealing process, the PCBM-phase forms evolving microstructures, i.e. crystalline aggregates. The different stages in annealing of the toluene based films reveal how the crystallites are formed. First, after a few minutes, the whole film shows some surface roughening, which results in a kind of blurred AFM image. This may correspond to some local reorganization of the polymer-rich phase or some release of therein-embedded PCBM. As next, some little crystallites are formed and grow at the expense of the surrounding round clusters (Fig. 3.3.2.3a). At an intermediate stage the crystallites are continuously growing at

the expense of the closest PCBM nanoclusters (Fig. 3.3.2.3b). Finally, after roughly 4 hours (Fig. 3.3.2.3c), most of the round PCBM nanoclusters are emptied and have left some circular holes behind (Fig. 3.3.2.3d). The continuous matrix framework around these holes consists of small nanospheres of about 30-40 nm in size, which is comparable to the results of the SEM-measurements obtained for cross-sections of the toluene cast films, taking a finite radius of curvature (5 – 10 nm) for the AFM-tip into account (compare Fig. 2.4.1.9). As the annealing has caused most of the PCBM to diffuse and organize in crystallites, these nanospheres are safely attributed to polymeric nanostructures.

The same annealing was performed for about half an hour on a film cast from chlorobenzene solution (compare Fig. 3.3.2.3e and 3.3.2.3f). The crystallites that evolved here seem to be smoother, which refers to a more homogenous growth process. Between these crystallites (magnification (f)) the originally flat film was almost unchanged and just closely around the crystallites the film morphology had altered considerably due to the depletion of the PCBM-phase. However, the topographic image reveals some granular structure (≤ 20 nm), reminding of the nanospheres observed by SEM.

To validate the observed nanomorphology of the polymer MDMO-PPV, the same annealing of toluene spin cast blends has been performed at different temperatures (compare with Fig. 3.3.2.4) ranging roughly 20 °C around 150 °C. If the temperature is chosen as low as 130 °C, the granular structure of the polymer matrix is also visible, but the fullerene clusters are not depleted fully (Fig. 3.3.2.4a). In the case of 150 °C the holes are almost empty (Fig. 3.3.2.4b) and as shown above the nanospheres are well visible. However, if the temperature exceeds a certain value (>165 °C), the nanospheres are no longer observed (Fig. 3.3.2.4c).

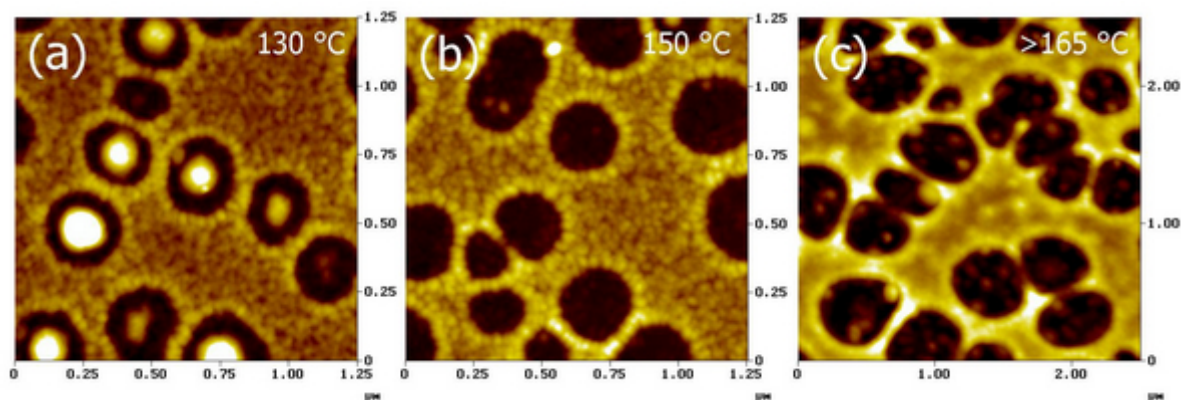


Fig. 3.3.2.4: Morphology of toluene cast blend films after annealing for four hours at several temperatures. For temperatures higher than 165 °C a change in the polymer morphology is observed. Note that in (c) the structures are larger, due to a higher solution concentration.

Instead the polymer matrix appears to be molten together. Since inside the holes still little granular particles are visible, the experimental resolution appears to be adequate. Therefore one can reason that in contrast to the literature, the relevant glass transition temperature of MDMO-PPV might be even larger than 150 °C, since only for higher temperatures larger changes in the polymer nanomorphology are observed by AFM.

To verify, whether MDMO-PPV exhibits the same spherical structure within its pristine phase, bare MDMO-PPV films were spin cast from chlorobenzene solution and imaged consequently at cross-sections with SEM. Though naturally (due to the missing darker fullerene signal) the contrast in pristine polymer films has to be lower than in the blends, similar nanospheres were found in these films (Fig. 3.3.2.5).

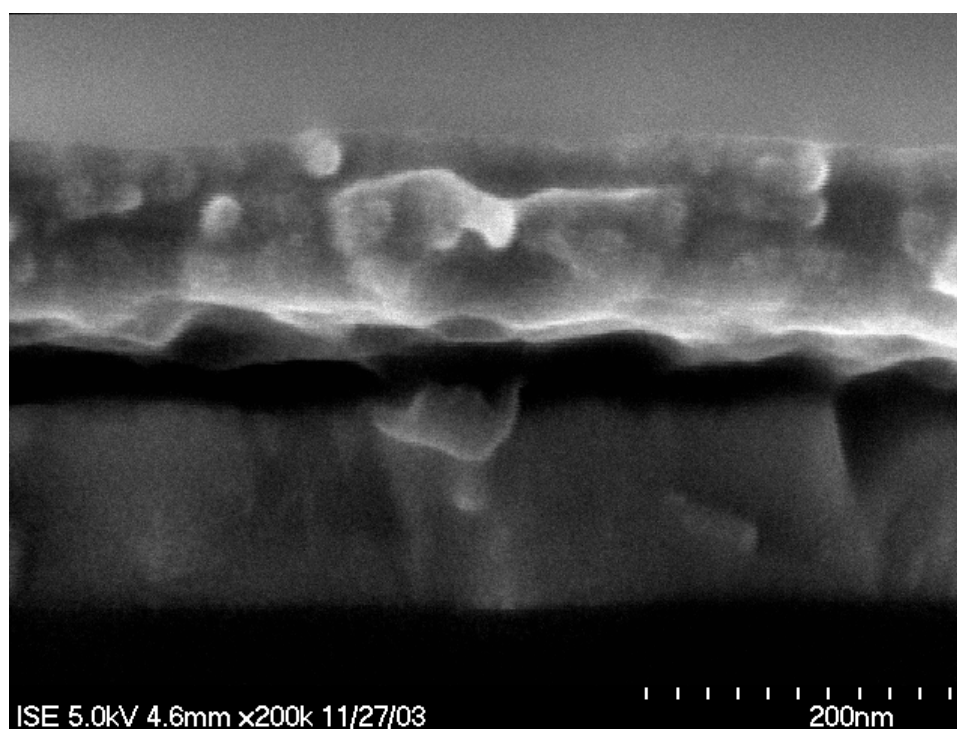


Fig. 3.3.2.5: Pristine MDMO-PPV film spin cast from chlorobenzene solution and imaged via cross-section SEM. Likewise in the blend with fullerenes, the film contains nanospheres.

Therefore it is indicated, that the nanosphere-morphology of MDMO-PPV is of universal character. Due to the limited contrast and resolution it cannot be excluded, that in pristine MDMO-PPV films different polymer morphologies are present. However, this is unlikely since the polymer-polymer and polymer-solvent interactions within the casting solution should result rather in one possible population of polymer chain conformation, when the

system has been brought into equilibrium (that is the complete dissolution of the polymer in the non-saturation regime).

3.3.3. Photoluminescence

Room temperature photoluminescence (PL) spectra of films of pristine MDMO-PPV, PCBM and blends (1:4) of the two have been obtained using an Argon-ion laser at 476 nm as excitation light source (see Fig. 3.3.3.1). After annealing the spectral shape of the photoluminescence of MDMO-PPV changes slightly. This is addressed to an ordering effect during annealing of MDMO-PPV. Compared to the polymer the PCBM film showed a much weaker photoluminescence, which is mainly attributed to a less efficient emission due to symmetry forbidden singlet radiative recombination as well as due to efficient intersystem crossing to the triplet state.¹¹⁰ For the chlorobenzene cast blend film there is no clear luminescence signal detectable, which indicates a rather complete exciton dissociation at the polymer-fullerene bulk interface. In fact the PL-signal is quenched by roughly three orders of magnitude (compare Fig. 3.3.3.1). In contrast, the corresponding films spin cast from toluene solution exhibit some residual photoluminescence of PCBM. This is attributed to the radiative recombination of excitons within the pretty large PCBM-nanoclusters, before they can reach the phase interface. As a result, for increasing PCBM cluster sizes (compare Figs. 3.2.4 and 3.3.3.1), the PL-signal of PCBM was likewise increased. In addition, the observation of the PL indicates the PCBM nanoclusters to be rather pure, since charge transfer to possibly embedded MDMO-PPV would quench this photoluminescence otherwise. Upon annealing of the blend films the MDMO-PPV photoluminescence reoccurs again due to the depletion of the PCBM phase within the polymer matrix upon crystallization of the PCBM. This effect has been found for both, toluene and chlorobenzene cast blend films.

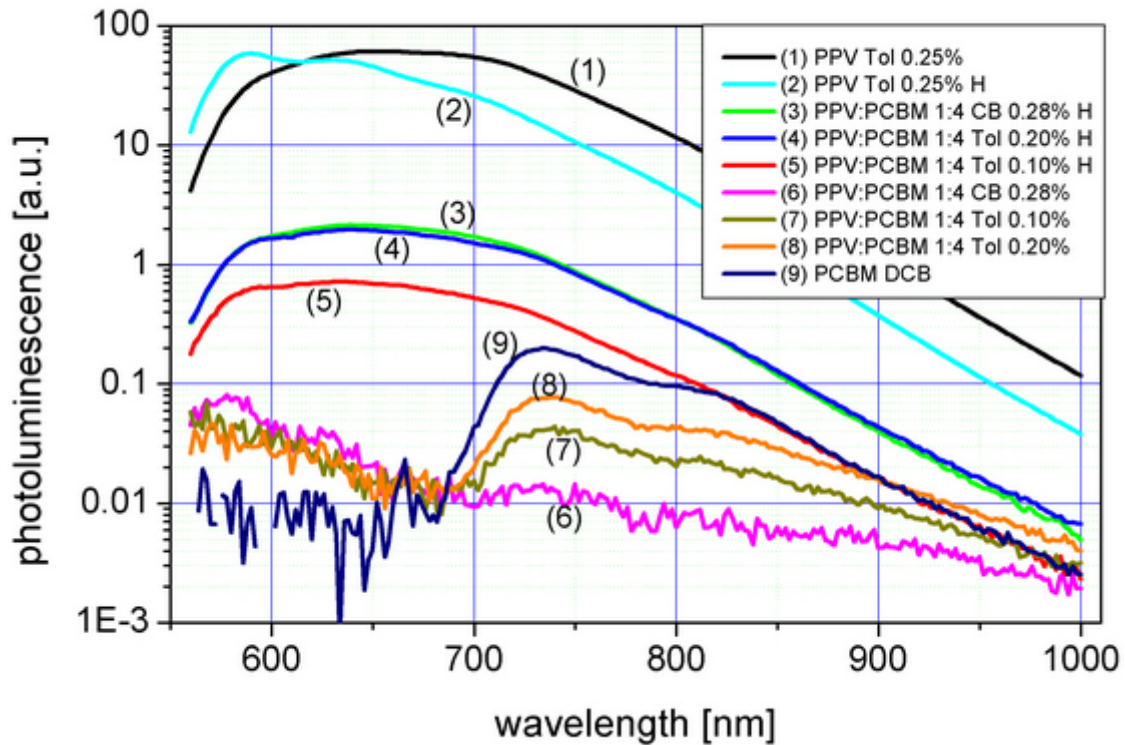


Fig. 3.3.3.1: Photoluminescence spectra of films of pristine MDMO-PPV (peak between 580 – 700 nm), pristine PCBM (peak at ~735 nm) and blends (1:4) of both cast from either toluene or chlorobenzene solution. While the non-heated blend film from chlorobenzene shows almost no detectable luminescence anymore, the blends spin cast from toluene clearly exhibit luminescence of PCBM. This is attributed to the radiative recombination of excitons within the PCBM nanoclusters that do not reach the interface to the MDMO-PPV-rich phase. The labels specify the material, the solvent (Tol=toluene, CB=chlorobenzene, DCB=di-chlorobenzene), the polymer concentration (by weight) and whether the film was heated (noted with H).

Because of the strong polymer PL the PL-signal of the PCBM was not distinguished any longer for the annealed films. Therefore, the PCBM was selectively excited by using a 664nm diode laser. At this wavelength the polymer is almost not absorbing clearly the PL of PCBM for the annealed film could be detected (see Fig. 3.3.3.2).

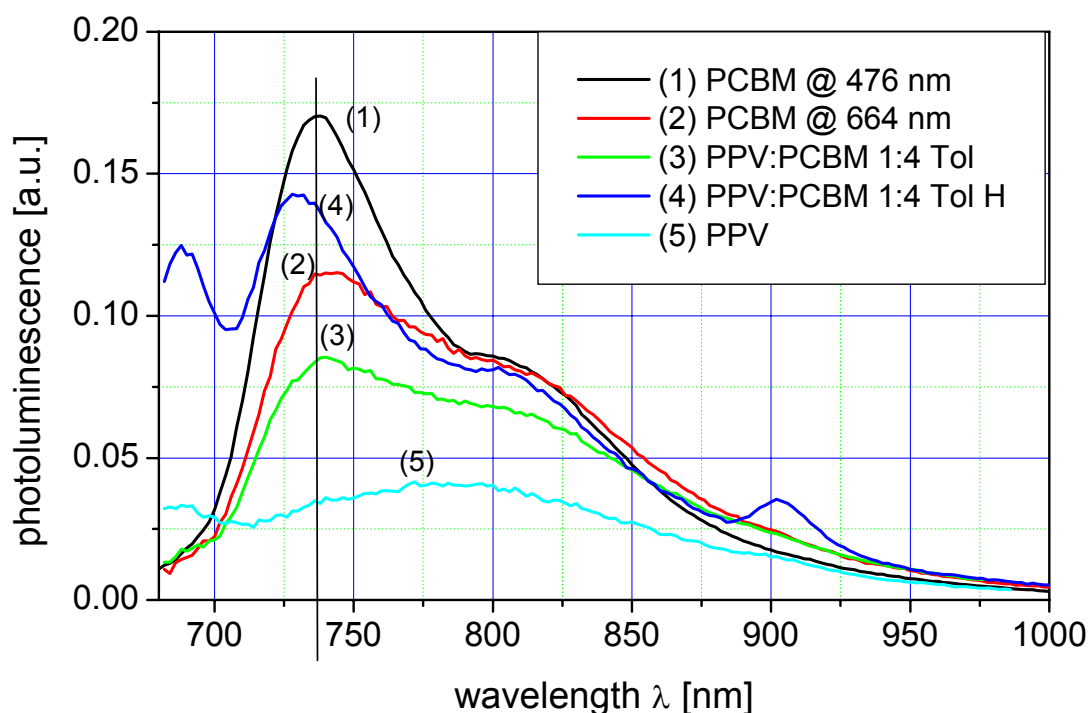


Fig. 3.3.3.2: Photoluminescence spectra obtained with excitation light at 664 nm, except for spectrum (1), which was excited with 476 nm and added for comparison. The PL of the pristine PCBM film changed slightly upon changed excitation wavelength (compare (1) and (2)). Spectra (3) and (4) are from a toluene based blend, (4) after annealing. (5) corresponds to the signal of a MDMO-PPV film.

There are two vibronic progressions present in the PL-spectrum of the annealed film, one at about 810 nm and the other slightly above 900 nm, which might be resulting from the higher crystallinity of the PCBM in the heated film. In addition there is a small blue shift of the main peak towards 730 nm observed. The peak below 700 nm is also weakly present for the MDMO-PPV film and might originate from the polymer.

3.3.4. Percolation and Connectivity

To discriminate further between toluene and chlorobenzene spin cast MDMO-PPV:PCBM blends, Kelvin Probe Force Microscopy was applied and the results were interpreted in combination with high resolution scanning electron microscopy. At first the pristine materials were investigated, both under cw-laser illumination and in the dark. In Fig. 3.3.4.1 the topography and the local work function are shown for an MDMO-PPV film spin cast on ITO.

Interestingly the topography exhibits the same features as for ITO alone (structure of platelets), which is expected to result from a thin film thickness of MDMO-PPV due to low (0.25wt.-%) solution concentration in chlorobenzene. However the work function is mostly unaffected by the platelet structure and an average value of 4.4 eV is found. Under illumination there is a shift of the work function towards slightly smaller values, yielding an average value around 4.34 eV.

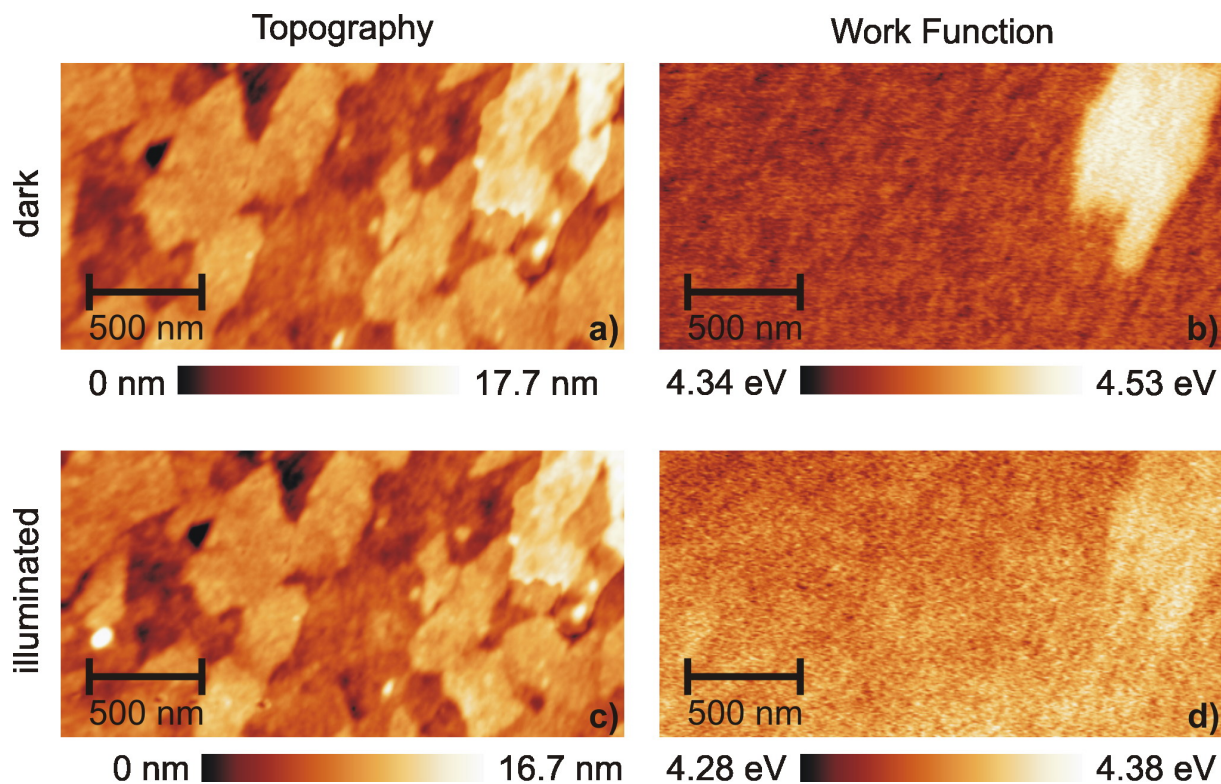


Fig. 3.3.4.1: Topography (a, c) and work function (b, d) of a pristine MDMO-PPV film, measured in the dark (a, b) and under 442 nm cw-laser illumination (c, d).

In the case of pristine PCBM films (compare Fig. 3.3.4.2) we find a more homogeneous and smoother surface topography as a result of spin casting the PCBM from the highly concentrated (3wt.-%) chlorobenzene solution. Also here the work function does not vary much and it is centered on 4.35 eV in the dark and very similar under illumination.

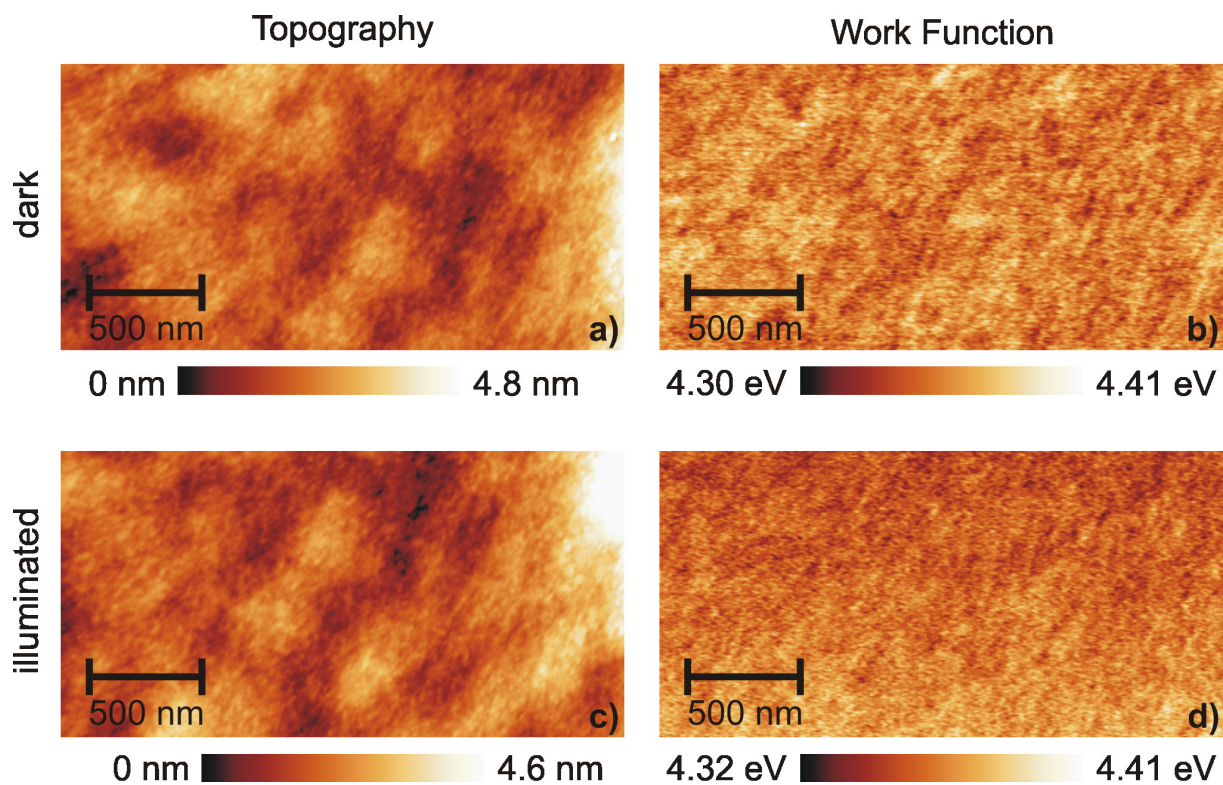


Fig. 3.3.4.2: Topography (a, c) and work function (b, d) of a pristine PCBM film, measured in the dark (a, b) and under 442 nm cw-laser illumination (c, d).

Figure 3.3.4.3 displays the measurements obtained on the blend film of MDMO-PPV and PCBM spin cast from chlorobenzene, both under light and in the dark. The average value of the work function in the dark is about 4.54 eV. Upon illumination the work function is shifted strongly down to 4.21 eV.

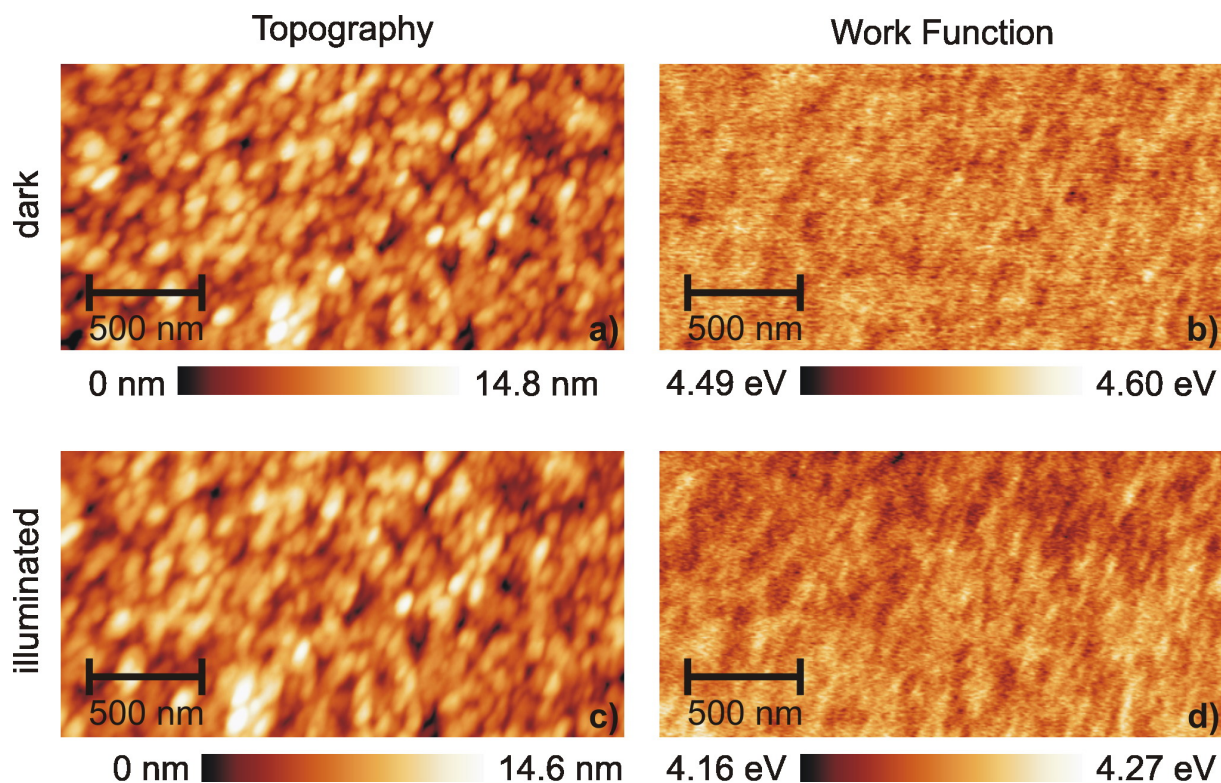


Fig. 3.3.4.3: Topography (a, c) and work function (b, d) of a chlorobenzene cast blend film of MDMO-PPV:PCBM with a mass ratio of 1:4, measured in the dark (a, b) and under 442 nm cw-laser illumination (c, d).

For toluene cast MDMO-PPV:PCBM blends the situation is different (compare Fig. 3.3.4.4). Firstly there is a broad range of values of the work function, depending on the place on the sample. In the dark the work function is ranging between 4.36 and 4.57 eV, whereas under illumination the spread is almost doubled. We illuminated the toluene cast sample with both, 442 nm and 675 nm cw-laser light, but the results are very similar. Note that the absorption of MDMO-PPV around 442 nm is almost 3 times stronger than that of PCBM. At 675 nm the situation is turned around and PCBM absorbs stronger than MDMO-PPV, where however the absolute values are much smaller.²⁰⁶

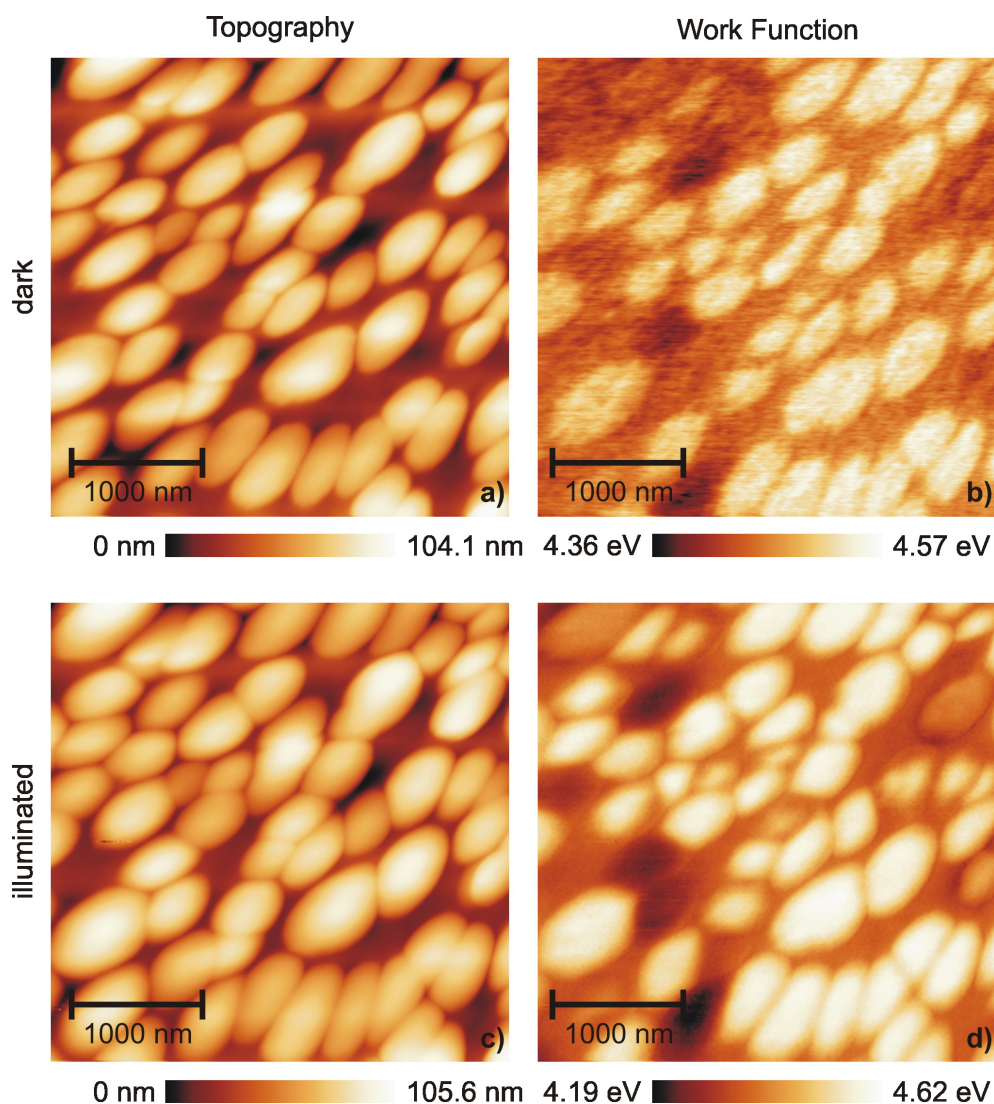


Fig. 3.3.4.4: Topography and work function of a toluene cast blend film of MDMO-PPV:PCBM with a mass ratio of 1:4, measured in the dark and under 675 nm cw-laser illumination. Note that some of the topographical hills lead to dark areas and thus low work functions, whereas the majority of the hills result in bright areas with high work functions.

In general the largest work function is observed on top of the elevations caused by the PCBM clusters. Recalling that a larger work function represents a larger barrier for electron extraction, this would mean a reduction in the electron density, and correspondingly an increase in the hole density, compared to the pristine films. While for the blend cast from chlorobenzene (Fig. 3.3.4.3) the work function in the dark has similar high or larger values (~ 4.55 eV) as the work function of the toluene cast blend, the situation under illumination is reversed. In the case of chlorobenzene cast blend films the work function shifts towards a lower value around 4.2 eV, whereas medium values of roughly 4.4 eV are generally found

between the elevations of PCBM clusters, whereas on top of these clusters the work function is increasing considerably beyond 4.6 eV (compare Fig. 3.3.4.4).

From SEM measurements it follows that polymeric nanospheres are generally located on top of the PCBM clusters, as shown above. On the other hand the blend films cast from chlorobenzene exhibit both phases, the polymer and the fullerene, towards the surface of the film. This can be clearly seen in Fig. 3.3.4.5, where chlorobenzene and toluene cast blends are compared with each other. Here the polymer nanospheres form percolating pathways and are distributed almost evenly throughout the bulk of the film, whereas a so-called skin layer, incorporating polymer nanospheres, surrounds the big PCBM clusters in toluene cast films.

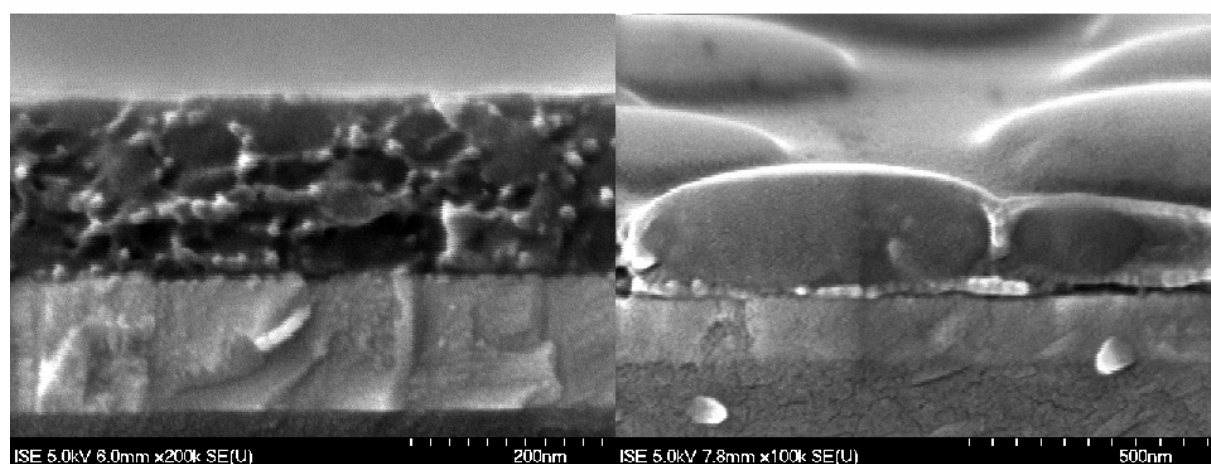


Fig. 3.3.4.5: SEM measurements on cross sections of MDMO-PPV:PCBM 1:4 blends. On the left a chlorobenzene and on the right a toluene cast film is shown for comparison. Polymer nanospheres are rather evenly distributed in the film on the left, while they surround the large PCBM clusters as a “skin-layer” in the right.

However, in Fig. 3.3.4.4 there are some remarkable exceptions where on top of the PCBM elevations the minimum value of ~ 4.2 eV is obtained for the work function. Also Martens et al.¹⁸³ reported a similar behavior for a single KPFM measurement on one particular PCBM cluster. This finding can be understood again with the help of high-resolution SEM measurements: in some cases the PCBM clusters are not surrounded by polymer nanospheres, but they are exposed freely to the film surface. Some examples of that are shown in Fig. 3.3.4.6 for illustration. Since according to the photoinduced charge transfer we expect the highest electron concentration within the bare PCBM phase, it is obvious that the extraction of electrons from these locations is energetically much more favorable than extraction through a hole enriched polymer barrier layer. Actually the increased contrast on the illuminated toluene

blend reflects therefore the increased local concentrations of holes and electrons due to the photoinduced charge transfer. Thus the skin layer around the PCBM clusters in the toluene cast blends may cause a severe limitation for electron transport towards the cathode. As a result in addition to an incomplete charge separation due to too small exciton diffusion lengths (compare PL measurements) in these largely phase separated structures, this electron transfer barrier will be another reason for the smaller photocurrent and power conversion efficiencies observed in toluene cast blends.

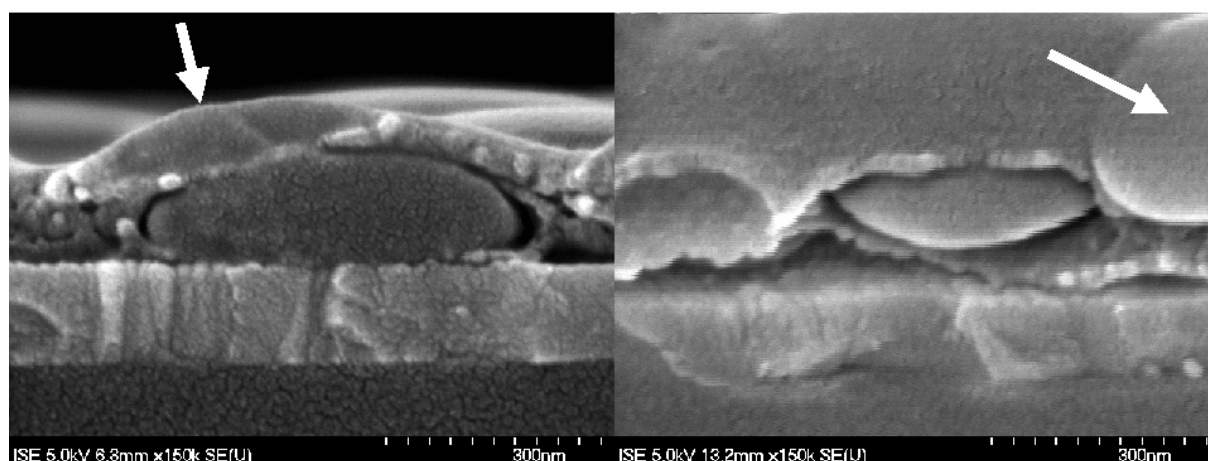


Fig. 3.3.4.6: Cross section SEM images of toluene cast MDMO-PPV:PCBM blend films. The white arrows point to regions, where PCBM clusters are exposed freely to the surface of the film.

4. Discussion

The smaller PCBM solubility in toluene (1wt.-%) as compared to chlorobenzene (4.2wt.-%) limits the concentration of 1:4 MDMO-PPV:PCBM blends to about 1.25wt.-%. Additional PCBM in the solution will precipitate, as demonstrated by the optical microscope images in Fig. 3.2.5. Therefore the reversal of trend for PCBM cluster sizes in films spin cast from 1:4 ratio 2.5wt.-% toluene blend solutions can be understood. The ratio between MDMO-PPV and PCBM dissolved in the solution should be around 1:2, since the solution contained a total 2wt.-% of PCBM.

When oil is dispersed as droplets into water, it requires constant stirring or the application of surfactants to achieve stable oil-in-water emulsions. Else the oil droplets will coalesce and increase in size to minimize the interfacial energy between the water and the oil phase.

Similarly, if immersed PCBM fullerene clusters would be present with a certain mean size in solution, they would require stabilization against coalescence. Since films spin cast from only heated and not stirred solutions show comparable PCBM cluster sizes as the stirred ones no such stabilization of a certain mean size due to the stirring is probable. Furthermore as films spin cast at higher spinning frequencies exhibit homogeneously smaller mean cluster sizes, PCBM clusters in toluene blend solutions are not likely to be present. Thus the large-scale phase separation and PCBM cluster evolution has to take place during the film formation under the presence of solvent molecules, which provide the mobility for fullerene diffusion.¹⁸³ The increased scale of demixing observed in films prepared by drop casting (compare Fig. 3.2.3) confirms this.

In both, chlorobenzene and toluene cast blends nanospheres were detected and assigned to the polymer phase. On a closer inspection of the nanosphere sizes it becomes evident, that the diameter is generally smaller than 20 nm (compare Fig. 4.1). The nanospheres appear to be slightly larger in the case of toluene cast blends, however this increase can at least partially be explained by the deposition of a thicker platinum layer when compared to chlorobenzene cast films. In addition causes noise the nanospheres to appear larger in the SEM images than they actually are (Fig. 4.1).

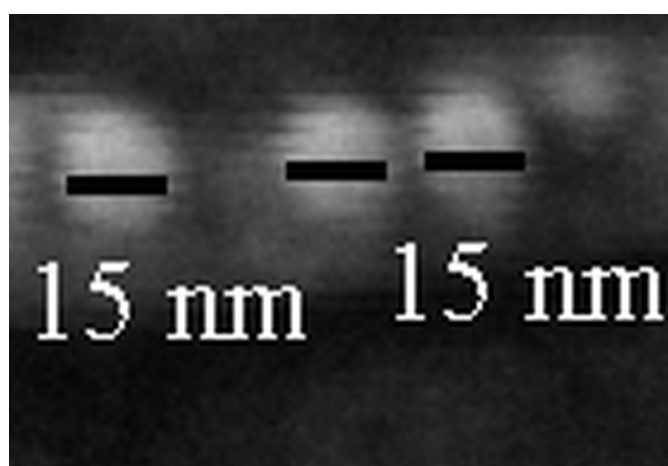


Fig. 4.1: Zoom of an SEM cross section image, allows to identify the correct size of polymer nanospheres to be about 15 nm. Noise can cause an apparent increase of the nanosphere size.

These nanospheres have to be indeed pristine single MDMO-PPV polymers, which can be shown by a simple calculation: taking the molecular mass of $m = 10^6$ u,¹⁸⁸ and a density of $\rho = 910$ kg/m³ ²⁰⁷ for MDMO-PPV into account, the volume V_c of one particular polymer chain readily calculates as:

$$V_c = \frac{m}{\rho} = \frac{10^6 \cdot 1.66 \cdot 10^{-21} \text{ kg}}{910 \text{ kg/m}^3} = 1.824 \cdot 10^{-24} \text{ m}^3.$$

With the volume V_s of a sphere $V_s = \frac{4}{3}\pi r_s^3$,

the radius r_s can be obtained, by equalizing $V_c = V_s$:

$$V_s = \frac{4}{3}\pi r^3 = V_c \Leftrightarrow r = \sqrt[3]{\frac{3}{4\pi} V_c} = \sqrt[3]{\frac{3}{4\pi} 1.824 \cdot 10^{-24} \text{ m}^3} = 7.57 \cdot 10^{-9} \text{ m}.$$

Thus the sphere diameter is determined to be ~ 15 nm, and an astonishing well agreement between the size of one nanosphere and the calculated volume taken up by a single MDMO-PPV chain is found. Since the polymer conformation within the blend films appeared rather similar for toluene and chlorobenzene, the difference in the morphology of the films may arise from different interactions of the respective solvent with the fullerene. Furthermore it can be concluded that the PCBM clusters are indeed pristine, since the polymer spheres are not found within the fullerene clusters. In addition it will be very unlikely for single polymer chains to extend into the fullerene phase due to the repulsive interaction, demonstrated by the observed phase separation upon annealing of the blends. The PCBM phase itself exhibits a nanocrystalline order, as demonstrated by TEM-SAED experiments. This close packing of even the substituted fullerene PCBM into crystalline organization might thus be the origin for the exceptionally high mobilities found for PCBM.²⁰⁸⁻²¹⁰

As a main result of the present findings, the conformation of MDMO-PPV as well as the crystalline order in the PCBM phase is illustrated in Fig. 4.2. As a conclusion for the charge transport in bulk heterojunction devices it should be noted, that actually the holes have to “hopp” between adjacent polymer nanospheres, but the electrons may be transported much better through percolated PCBM nanocrystals. In combination with this result, the schematic image of the bulk heterojunction was changed to account for the polymer and fullerene phases (Fig. 4.3).

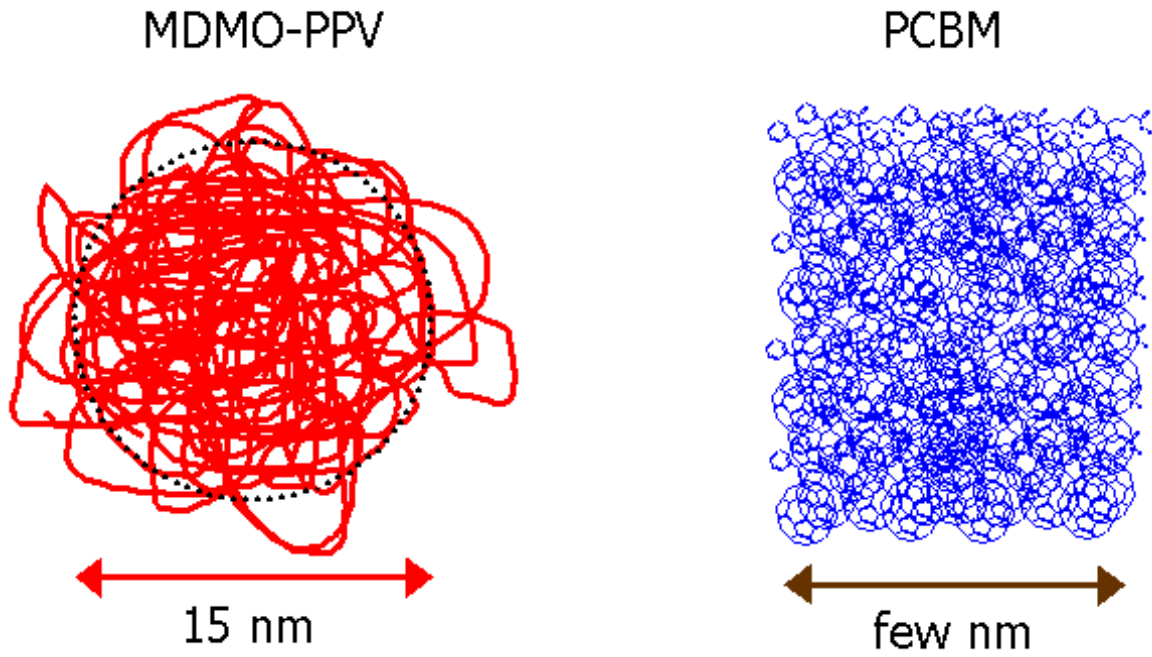


Fig. 4.2: A center finding of the present study for the molecular conformation in solid-state blends or pristine films. The MDMO-PPV organizes in single chains into nanospheres, whereas the PCBM molecules built up small nanocrystals.

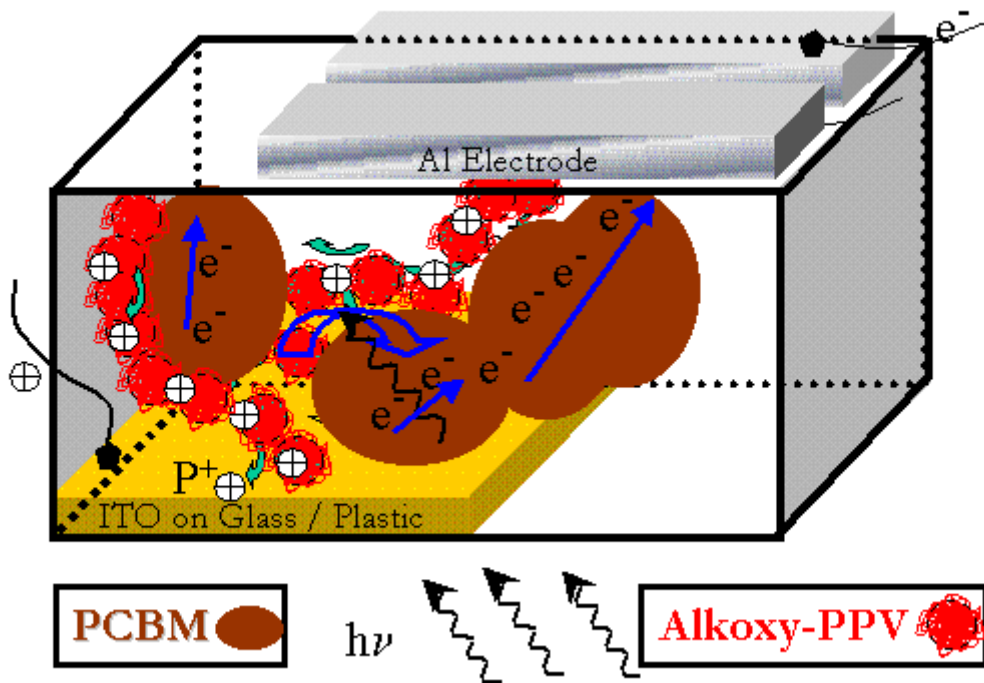


Fig. 4.3: Revised image of the polymer/fullerene bulk heterojunction: polymer nanosphere-coils and rather homogeneous fullerene phases incorporating PCBM nanocrystals.

Reviewing the photoluminescence spectra in Fig. 3.3.3.1 reveals the existence of a weak residual MDMO-PPV signal. Several spectra from Fig. 3.3.3.1 thus have been normalized and re-plotted (Fig. 4.4). Comparing the PL spectrum of the pristine MDMO-PPV films spin cast from toluene and subsequent annealing causes a blue shift of the emission spectra accompanied with a more refined phonon structure. This change is attributed to an ordering effect within MDMO-PPV. Though the spectra from the nanospheres in the blends are weak, it can be clearly seen that their maximum emission is even more blue shifted than that of the annealed polymer film. This has been observed earlier and was assigned to the bleaching of the π - π^* interband transition due to the photoinduced charge transfer.⁵ On the other hand one may argue that the photoluminescence could originate from the center of a MDMO-PPV nanosphere: assuming that in the center of the sphere the polymer will exhibit the smallest conjugation lengths due to the strongest coiling there. This would be in agreement with the fact that smaller conjugation lengths result in blue shifted PL-spectra.²¹¹

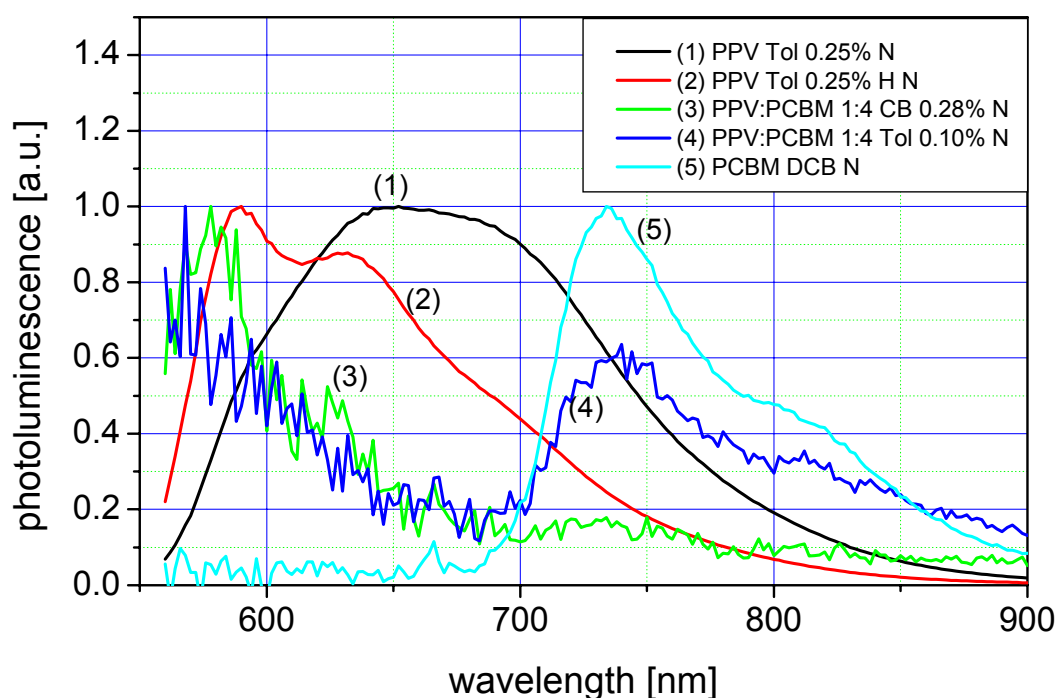


Fig. 4.4: Normalized (N) photoluminescence spectra. The residual PL signal of MDMO-PPV in blends with PCBM could yield information about the state of local order inside of the nanospheres.

Furthermore it is clear from the pristine PCBM film, that indeed the PL signal observed has to originate from MDMO-PPV alone. That the same conformation of MDMO-PPV in both

blends cast from different solvents is present is confirmed by very similar emission spectra. Since photoexcitations are known to migrate towards longer conjugation lengths,²¹¹ the excited state would have to relax automatically towards the surface of the polymer nanosphere, were the coiling should be less strong and thus the conjugation length longer. Therefore, based on the above-mentioned assumption on different coiling lengths, the geometry of a polymer nanosphere may be favorable for high charge transfer efficiency.

A spherical shape of conjugated polymer particles has been suggested and promoted already earlier by Wessling (compare e.g. 204).

Finally it became evident by the KPFM measurements that the different solvents result in a different phase structure at the film surface and thus the interface to the electron extracting cathode. This situation is illustrated in Fig. 4.5. Thus the photogenerated electrons in toluene cast blends experience a barrier towards the aluminum cathode due to the presence of hole-rich polymer nanospheres (Fig. 4.5a), whereas for chlorobenzene cast films the electron transfer to the electrode is morphologically not hindered (Fig. 4.5b).

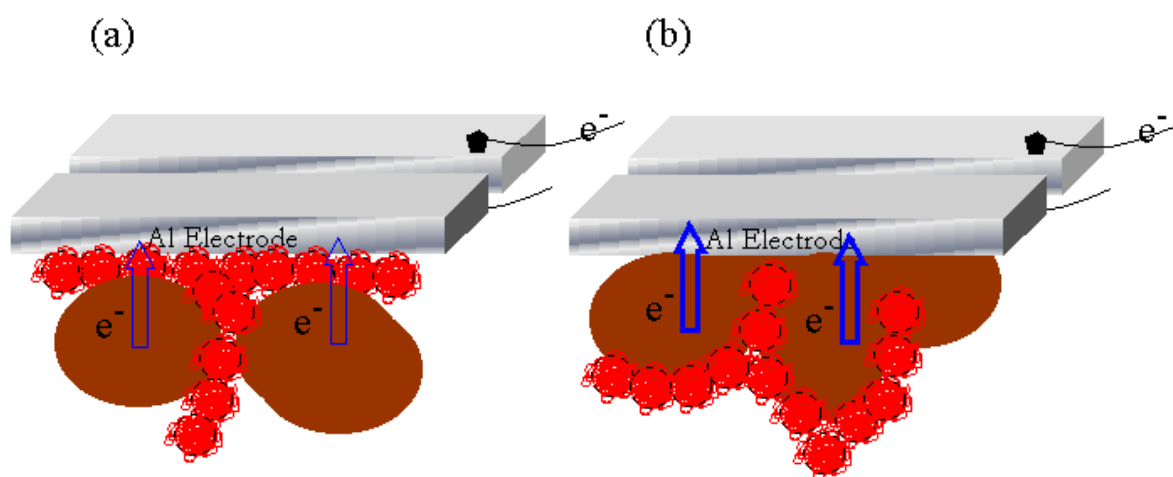


Fig. 4.5: The ease of electron transfer from the PCBM phase towards the cathode is schematically illustrated. In toluene cast films the electron transfer is hampered due to the presence of the hole conducting polymer nanospheres (a), whereas in chlorobenzene cast films electrons have free access to the aluminum electrode (b).

It should be pointed out again, that MDMO-PPV and PCBM never show the tendency to intimate blending. The in the literature previously assigned homogenous blend phase exhibits fullerene nanocrystals, which is in contrast to a molecular mixing. This tendency to form the

nanocrystals clearly demonstrates the direction of lowering the free energy in the blend. Also the coiled conformation of the polymer cannot be a product of attractive interaction with the fullerenes, rather the opposite, the polymer is retracted from the close interaction with the PCBM and forms nanospheres to minimize the surface-to-volume ratio and thus the interfacial energy with the fullerene phase.

The less phase separated chlorobenzene cast blends are thus dynamically hindered to complete the phase separation, in other words the mobility of the PCBM molecules times the time of film formation (respectively solvent evaporation) in chlorobenzene based spin cast blend films is too small, to lead to the creation of larger domains. Consequently the application of longer drying times promoted also in chlorobenzene based blends large scale demixing.^{183,186} However, the reason for the improved diffusion mobility of PCBM molecules in toluene cast blend films, yielding the coarser phase separation, remains to be answered.

5. Conclusions

The nanostructure of MDMO-PPV:PCBM bulk heterojunctions was successfully revealed at molecular resolution by the combination of several “nanoscopy” techniques as SEM, AFM and TEM. PL and KPFM experiments were useful techniques for understanding the limits of charge carrier generation and transport. The central finding of the present study is that the polymer MDMO-PPV organizes in a coiled conformation as a “nanosphere”, which has not been resolved in previous reports. The spherical shape of the polymer allows a similar efficient electron transfer in both, the toluene and chlorobenzene cast blends. It was identified that in the toluene cast blend the large PCBM nanoclusters result in an inactive volume, since photoexcitations were not completely quenched by the adjacent polymer. This can be attributed to a limited exciton diffusion length. Furthermore resulted the inclusion of the PCBM clusters within surrounding polymer nanospheres in a barrier for electron transport towards the cathode. The photogenerated holes in these polymer nanospheres on the top of PCBM clusters need therefore to travel also much longer ways around them to reach the anode at the bottom. The latter three reasons will cause a limitation for the photocurrent generation in toluene cast blends. The optimum morphology in these conjugated polymer/fullerene bulk heterojunction devices requires therefore a good percolation of both phases to the respective electrodes. Whereas PCBM forms larger aggregates including nanocrystals for efficient charge transport, the polymer percolates via adjacent nanospheres.

6. References

1. A. Goetzberger, C. Hebling, and H.-W. Schock, Photovoltaic materials, history, status and outlook, *Materials Science and Engineering R* 40, 1 (2003).
2. D.M. Chapin, C.S. Fuller, and G.L. Pearson, A New Silicon p-n Junction Photocell for Converting Solar Radiation into Electrical Power, *J. Appl. Phys.* 25, 676 (1954).
3. H. Spanggaard and F.C. Krebs, A brief history of the development of organic and polymeric photovoltaics, *Sol. Energy Mater. Sol. Cells* 83, 125 (2004).
4. H. Hoppe and N.S. Sariciftci, Organic solar cells: an overview, *J. Mater. Res.* 19, 1924 (2004).
5. N.S. Sariciftci, L. Smilowitz, A.J. Heeger, and F. Wudl, Photoinduced electron transfer from a conducting polymer to buckminsterfullerene, *Science* 258, 1474 (1992).
6. G.A. Chamberlain, Organic Solar Cells: A Review, *Solar Cells* 8, 47 (1983).
7. D. Wöhrle and D. Meissner, Organic Solar Cells, *Adv. Mater.* 3, 129 (1991).
8. C.J. Brabec, N.S. Sariciftci, and J.C. Hummelen, Plastic Solar Cells, *Adv. Funct. Mater.* 11, 15 (2001).
9. J.J.M. Halls and R.H. Friend, in *Clean Electricity from Photovoltaics*, edited by M. D. Archer and R. Hill (Imperial College Press, London, 2001).
10. J. Nelson, Organic photovoltaic films, *Curr. Opin. Solid State Mater. Sci.* 6, 87 (2002).
11. J.-M. Nunzi, Organic photovoltaic materials and devices, *C. R. Physique* 3, 523 (2002).
12. *Organic Photovoltaics: Concepts and Realization; Vol. 60*, edited by C.J. Brabec, V. Dyakonov, J. Parisi, and N.S. Sariciftci (Springer, Berlin, 2003).
13. P. Peumans, A. Yakimov, and S.R. Forrest, Small molecular weight organic thin-film photodetectors and solar cells, *J. Appl. Phys.* 93, 3693 (2003).
14. B. Maennig, J. Drechsel, D. Gebeyehu, P. Simon, F. Kozlowski, A. Werner, F. Li, S. Grundmann, S. Sonntag, M. Koch, K. Leo, M. Pfeiffer, H. Hoppe, D. Meissner, S. Sariciftci, I. Riedel, V. Dyakonov, and J. Parisi, Organic p-i-n solar cells, *Appl. Phys. A* 79, 1 (2004).
15. *Handbook of Conducting Polymers; Vol. 1-2*, edited by T.A. Skotheim (Marcel Dekker, Inc., New York, 1986).
16. *Handbook of Organic Conductive Molecules and Polymers; Vol. 1-4*, edited by H.S. Nalwa (John Wiley & Sons Ltd., Chichester, 1997).
17. *Handbook of Conducting Polymers; Vol. ,* edited by T.A. Skotheim, R.L. Elsenbaumer, and J.R. Reynolds (Marcel Dekker, Inc., New York, 1998).
18. *Semiconducting Polymers; Vol. ,* edited by G. Hadziioannou and P.F. van Hutten (WILEY-VCH, Weinheim, 2000).

19. C. Winder and N.S. Sariciftci, Low Bandgap Polymers for Photon Harvesting in Bulk Heterojunction Solar Cells, *J. Mater. Chem.* 14, 1077 (2004).
20. C.D. Dimitrakopoulos and D.J. Mascaro, Organic thin-film transistors: A review of recent advances, *IBM J. Res. Dev.* 45, 11 (2001).
21. J.J.M. Halls, K. Pichler, R.H. Friend, S.C. Moratti, and A.B. Holmes, Exciton diffusion and dissociation in a poly(p-phenylenevinylene)/C60 heterojunction photovoltaic cell, *Appl. Phys. Lett.* 68, 3120 (1996).
22. J.J.M. Halls and R.H. Friend, The Photovoltaic Effect in a Poly(p-phenylenevinylene) / Perylene Heterojunction, *Synth. Met.* 85, 1307 (1997).
23. H.R. Kerp, H. Donker, R.B.M. Koehorst, T.J. Schaafsma, and E.E. van Faassen, Exciton transport in organic dye layers for photovoltaic applications, *Chem. Phys. Lett.* 298, 302 (1998).
24. T.J. Savanije, J.M. Warman, and A. Goossens, Visible light sensitisation of titanium dioxide using a phenylene vinylene polymer, *Chem. Phys. Lett.* 287, 148 (1998).
25. A. Haugeneder, M. Neges, C. Kallinger, W. Spirkl, U. Lemmer, J. Feldmann, U. Scherf, E. Harth, A. Gügel, and K. Müllen, Exciton diffusion and dissociation in conjugated polymer/fullerene blends and heterostructures, *Phys. Rev. B* 59, 15346 (1999).
26. L.A.A. Pettersson, L.S. Roman, and O. Inganäs, Modeling photocurrent action spectra of photovoltaic devices based on organic thin films, *J. Appl. Phys.* 86, 487 (1999).
27. M. Stoessel, G. Wittmann, J. Staudigel, F. Steuber, J. Blässing, W. Roth, H. Klausmann, W. Rogler, J. Simmerer, A. Winnacker, M. Inbasekaran, and E.P. Woo, Cathode-induced luminescence quenching in polyfluorenes, *J. Appl. Phys.* 87, 4467 (2000).
28. T. Stübinger and W. Brütting, Exciton diffusion and optical interference in organic donor–acceptor photovoltaic cells, *J. Appl. Phys.* 90, 3632 (2001).
29. J.E. Kroeze, T.J. Savanije, M.J.W. Vermeulen, and J.M. Warman, Contactless Determination of the Photoconductivity Action Spectrum, Exciton Diffusion Length, and Charge Separation Efficiency in Polythiophene-Sensitized TiO₂ Bilayers, *J. Phys. Chem. B* 107, 7696 (2003).
30. *Primary Photoexcitations in Conjugated Polymers: Molecular Exciton versus Semiconductor Band Model; Vol. 1*, edited by N.S. Sariciftci (World Scientific, 1997).
31. B.A. Gregg and M.C. Hanna, Comparing organic to inorganic photovoltaic cells: Theory, experiment, and simulation, *J. Appl. Phys.* 93, 3605 (2003).
32. I.D. Parker, Carrier tunneling and device characteristics in polymer light-emitting diodes, *J. Appl. Phys.* 75, 1656 (1994).

33. A.K. Gosh, D.L. Morel, T. Feng, R.F. Shaw, and C.A. Rowe(Jr.), Photovoltaic and rectification properties of Al/Mg phthalocyanine/Ag Schottky-barrier cells, *J. Appl. Phys.* 45, 230 (1974).
34. D. Meissner, S. Siebentritt, and S. Günster, "Charge carrier photogeneration in organic solar cells," presented at the Int. Symp. on Optical Materials Technol. for Energy Efficiency and Solar Energy Conversion XI: Photovoltaics, Photochemistry and Photoelectrochemistry, Toulouse, 1992.
35. S. Karg, W. Riess, V. Dyakonov, and M. Schwoerer, Electrical and optical characterization of poly(phenylene-vinylene) light emitting diodes, *Synth. Met.* 54, 427 (1993).
36. D.L. Morel, A.K. Gosh, T. Feng, E.L. Stogryn, P.E. Purwin, R.F. Shaw, and C. Fishman, High-efficiency organic solar cells, *Appl. Phys. Lett.* 32, 495 (1978).
37. A.K. Gosh and T. Feng, Merocyanine organic solar cells, *J. Appl. Phys.* 49, 5982 (1978).
38. S.M. Sze, *Physics of semiconductor devices* (J. Wiley & Sons, New York, 1981).
39. C.W. Tang, Two-layer organic photovoltaic cell, *Appl. Phys. Lett.* 48, 183 (1986).
40. J. Rostalski and D. Meissner, Monochromatic versus solar efficiencies of organic solar cells, *Sol. Energy Mater. Sol. Cells* 61, 87 (2000).
41. P. Peumans, V. Bulovic, and S.R. Forrest, Efficient photon harvesting at high optical intensities in ultrathin organic double-heterostructure photovoltaic diodes, *Appl. Phys. Lett.* 76, 2650 (2000).
42. M. Hiramoto, M. Suezaki, and M. Yokoyama, Effect of Thin Gold Interstitial-layer on the Photovoltaic Properties of Tandem Organic Solar Cells, *Chem. Lett.*, 327 (1990).
43. M. Hiramoto, H. Fujiwara, and M. Yokoyama, Three-layered organic solar cell with a photoactive interlayer of codeposited pigments, *Appl. Phys. Lett.* 58, 1062 (1991).
44. M. Hiramoto, H. Fujiwara, and M. Yokoyama, p-i-n like behavior in three-layered organic solar cells having a co-deposited interlayer of pigments, *J. Appl. Phys.* 72, 3781 (1992).
45. R.N. Marks, J.J.M. Halls, D.D.C. Bradley, R.H. Friend, and A.B. Holmes, The photovoltaic response in poly(p-phenylene vinylene) thin-film devices, *J. Phys.: Condens. Matter* 6, 1379 (1994).
46. G. Yu, C. Zhang, and A.J. Heeger, Dual-function semiconducting polymer devices: Light-emitting and photodetecting diodes, *Appl. Phys. Lett.* 64, 1540 (1994).
47. H. Antoniadis, B.R. Hsieh, M.A. Abkowitz, S.A. Jenekhe, and M. Stolka, Photovoltaic and photoconductive properties of aluminum/poly(p-phenylene vinylene) interfaces, *Synth. Met.* 62, 265 (1994).

48. L. Smilowitz, N.S. Sariciftci, R. Wu, C. Gettinger, A.J. Heeger, and F. Wudl, Photoexcitation spectroscopy of conducting-polymer-C60 composites: Photoinduced electron transfer, *Phys. Rev. B* 47, 13835 (1993).
49. C.H. Lee, G. Yu, D. Moses, K. Pakbaz, C. Zhang, N.S. Sariciftci, A.J. Heeger, and F. Wudl, Sensitization of the photoconductivity of conducting polymers by C60: Photoinduced electron transfer, *Phys. Rev. B* 48, 15425 (1993).
50. S. Morita, A.A. Zakhidov, and K. Yoshino, Doping effect of buckminsterfullerene in conducting polymer: Change of absorption spectrum and quenching of luminescence, *Solid State Commun.* 82, 249 (1992).
51. S. Morita, S. Kiyomatsu, X.H. Yin, A.A. Zakhidov, T. Noguchi, T. Ohnishi, and K. Yoshino, Doping effect of buckminsterfullerene in poly(2,5-dialkoxy-p-phenylene vinylene), *J. Appl. Phys.* 74, 2860 (1993).
52. N.S. Sariciftci, D. Braun, C. Zhang, V.I. Srdanov, A.J. Heeger, G. Stucky, and F. Wudl, Semiconducting polymer-buckminsterfullerene heterojunctions: Diodes, photodiodes, and photovoltaic cells, *Appl. Phys. Lett.* 62, 585 (1993).
53. L.S. Roman, W. Mammo, L.A.A. Petterson, M.R. Andersson, and O. Inganäs, High Quantum Efficiency Polythiophene/C60 Photodiodes, *Adv. Mater.* 10, 774 (1998).
54. G. Yu, J. Gao, J.C. Hummelen, F. Wudl, and A.J. Heeger, Polymer Photovoltaic Cells: Enhanced Efficiencies via a Network of Internal Donor-Acceptor Heterojunctions, *Science* 270, 1789 (1995).
55. C.Y. Yang and A.J. Heeger, Morphology of composites of semiconducting polymers mixed with C60, *Synth. Met.* 83, 85 (1996).
56. J.C. Hummelen, B.W. Knight, F. LePeq, F. Wudl, J. Yao, and C.L. Wilkins, Preparation and Characterization of Fulleroid and Methanofullerene Derivatives, *J. Org. Chem.* 60, 532 (1995).
57. G. Yu and A.J. Heeger, Charge separation and photovoltaic conversion in polymer composites with internal donor/acceptor heterojunctions, *J. Appl. Phys.* 78, 4510 (1995).
58. J.J.M. Halls, C.A. Walsh, N.C. Greenham, E.A. Marseglia, R.H. Friend, S.C. Moratti, and A.B. Holmes, Efficient photodiodes from interpenetrating polymer networks, *Nature* 376, 498 (1995).
59. K. Tada, K. Hosada, M. Hirohata, R. Hidayat, T. Kawai, M. Onoda, M. Teraguchi, T. Masuda, A.A. Zakhidov, and K. Yoshino, Donor polymer (PAT6) - acceptor polymer (CNPPV) fractal network photocells, *Synth. Met.* 85, 1305 (1997).

60. M. Granström, K. Petritsch, A.C. Arias, A. Lux, M.R. Andersson, and R.H. Friend, Laminated fabrication of polymeric photovoltaic diodes, *Nature* 395, 257 (1998).
61. P. Peumans and S.R. Forrest, Very-high-efficiency double-heterostructure copper phthalocyanine/C60 photovoltaic cells, *Appl. Phys. Lett.* 79, 126 (2001).
62. P. Peumans and S.R. Forrest, Erratum: "Very-high-efficiency double-heterostructure copper phthalocyanine/C60 photovoltaic cells" [*Appl. Phys. Lett.* 79, 126 (2001)], *Appl. Phys. Lett.* 80, 338 (2002).
63. S.E. Shaheen, C.J. Brabec, N.S. Sariciftci, F. Padinger, T. Fromherz, and J.C. Hummelen, 2.5% efficient organic plastic solar cells, *Appl. Phys. Lett.* 78, 841 (2001).
64. J.M. Kroon, M.M. Wienk, W.J.H. Verhees, and J.C. Hummelen, Accurate efficiency determination and stability studies of conjugated polymer/fullerene solar cells, *Thin Solid Films* 403-404, 223 (2002).
65. T. Munters, T. Martens, L. Goris, V. Vrindts, J. Manca, L. Lutsen, W.D. Ceunick, D. Vanderzande, L.D. Schepper, J. Gelan, N.S. Sariciftci, and C.J. Brabec, A comparison between state-of-the-art 'gilch' and 'sulphinyl' synthesised MDMO-PPV / PCBM bulk heterojunction solar cells, *Thin Solid Films* 403-404, 247 (2002).
66. T. Aernouts, W. Geens, J. Portmans, P. Heremans, S. Borghs, and R. Mertens, Extraction of bulk and contact components of the series resistance in organic bulk donor-acceptor-heterojunctions, *Thin Solid Films* 403-404, 297 (2002).
67. P. Schilinsky, C. Waldauf, and C.J. Brabec, Recombination and loss analysis in polythiophene based bulk heterojunction photodetectors, *Appl. Phys. Lett.* 81, 3885 (2002).
68. F. Padinger, R.S. Rittberger, and N.S. Sariciftci, Effects of Postproduction Treatment on Plastic Solar Cells, *Adv. Funct. Mater.* 13, 1 (2003).
69. M. Svensson, F. Zhang, S.C. Veenstra, W.J.H. Verhees, J.C. Hummelen, J.M. Kroon, O. Inganäs, and M.R. Andersson, High-Performance Polymer Solar Cells of an Alternating Polyfluorene Copolymer and a Fullerene Derivative, *Adv. Mater.* 15, 988 (2003).
70. M.M. Wienk, J.M. Kroon, W.J.H. Verhees, J. Knol, J.C. Hummelen, P.A. van Hall, and R.A.J. Janssen, Efficient Methano[70]fullerene/MDMO-PPV Bulk Heterojunction Photovoltaic Cells, *Angew. Chem. Int. Ed.* 42, 3371 (2003).
71. W. Geens, T. Aernouts, J. Poortmans, and G. Hadziioannou, Organic co-evaporated films of a PPV-pentamer and C60: model systems for donor/acceptor polymer blends, *Thin Solid Films* 403-404, 438 (2002).
72. P. Peumans, S. Uchida, and S.R. Forrest, Efficient bulk heterojunction photovoltaic cells using small-molecular-weight organic thin films, *Nature* 425, 158 (2003).

73. D. Gebeyehu, M. Pfeiffer, B. Maennig, J. Drechsel, A. Werner, and K. Leo, Highly efficient p-i-n type organic photovoltaic devices, *Thin Solid Films* 451-452, 29 (2004).
74. J. Krüger, R. Plass, L. Cevey, M. Piccirelli, M. Grätzel, and U. Bach, High efficiency solid-state photovoltaic device due to inhibition of interface charge recombination, *Appl. Phys. Lett.* 79, 2085 (2001).
75. J. Krüger, R. Plass, M. Grätzel, and H.-J. Matthieu, Improvement of the photovoltaic performance of solid-state dye-sensitized device by silver complexation of the sensitizer cis-bis(4,4-dicarboxy-2,2bipyridine)-bis(isothiocyanato) ruthenium(II), *Appl. Phys. Lett.* 81, 367 (2002).
76. W.U. Huynh, J.J. Dittmer, and A.P. Alivisato, Hybrid Nanorod-Polymer Solar Cells, *Science* 295, 2425 (2002).
77. H. Tributsch and M. Calvin, Electrochemistry of excited molecules. Photoelectrochemical reactions of chlorophylls, *Photochem. Photobiol.* 14, 95 (1971).
78. H. Tributsch, Reaction of excited chlorophyll molecules at electrodes and in photosynthesis, *Photochem. Photobiol.* 16, 261 (1972).
79. T. Osa and M. Fujihira, Photocell using covalently-bound dyes on semiconductor surfaces, *Nature* 264, 349 (1976).
80. M. Fujihira, N. Ohishi, and T. Osa, Photocell using covalently-bound dyes on semiconductor surfaces, *Nature* 268, 226 (1977).
81. H. Tsubomura, M. Matsumura, K. Nakatani, K. Yamamoto, and K. Maeda, 'Wet-type' solar cells with semiconductor electrodes, *Sol. Energy* 21, 93 (1978).
82. M. Matsumura, S. Matsudaira, H. Tsubomura, M. Takata, and H. Yanagida, Sintered ZnO electrode for dye-sensitized photocell, *Yogyo Kyokai Shi* 87, 167 (1979).
83. B. O'Regan and M. Grätzel, A low cost, high-efficiency solar cell based on dye-sensitized colloidal TiO₂ films, *Nature* 353, 737 (1991).
84. K. Kalyanasundaram and M. Grätzel, Applications of functionalized transition metal complexes in photonic and optoelectronic devices, *Coordin. Chem. Rev.* 77, 347 (1998).
85. M. Grätzel, Photoelectrochemical Cells, *Nature* 414, 338 (2001).
86. M. Grätzel, Dye-sensitized solar cells, *J. Photochem. Photobiol. C* 4, 145 (2003).
87. U. Bach, D. Lupo, P. Comte, J.E. Moser, F. Weissörtel, J. Salbeck, H. Spreitzer, and M. Grätzel, Solid-state dye-sensitized mesoporous TiO₂ solar cells with high photon-to-electron conversion efficiencies, *Nature* 395, 583 (1998).
88. J.S. Salafsky, Exciton dissociation, charge transport, and recombination in ultrathin, conjugated polymer-TiO₂ nanocrystal intermixed composites, *Phys. Rev. B* 59, 10885 (1999).

89. A.C. Arango, L.R. Johnson, V.N. Bliznyuk, Z. Schlesinger, S.A. Carter, and H.-H. Hörhold, Efficient Titanium Oxide/Conjugated Polymer Photovoltaics for Solar Energy Conversion, *Adv. Mater.* 89, 1689 (2000).
90. Q. Fan, B. McQuillin, D.D.C. Bradley, S. Whitelegg, and A.B. Seddon, A solid state solar cell using sol-gel processed material and a polymer, *Chem. Phys. Lett.* 347, 325 (2001).
91. D. Gebeyehu, C.J. Brabec, F. Padinger, T. Fromherz, S. Spiekermann, N. Vlachopoulos, F. Kienberger, H. Schindler, and N.S. Sariciftci, Solid state dye-sensitized TiO₂ solar cells with poly(3-octylthiophene) as hole transport layer, *Synth. Met.* 121, 1549 (2001).
92. Y. Saito, T. Kitamura, Y. Wada, and S. Yanagida, Poly(3,4-ethylenedioxythiophene) as a hole conductor in solid state dye sensitized solar cells, *Synth. Met.* 131, 185 (2002).
93. K.M. Coakley, Y. Liu, M.D. McGehee, K. Frindell, and G.D. Stucky, Infiltrating Semiconducting Polymers into Self-Assembled Mesoporous Titania Films for Photovoltaic Applications, *Adv. Funct. Mater.* 13, 301 (2003).
94. K.M. Coakley and M.D. McGehee, Photovoltaic cells made from conjugated polymers infiltrated into mesoporous titania, *Appl. Phys. Lett.* 83, 3380 (2003).
95. N.C. Greenham, X. Peng, and A.P. Alivisatos, Charge separation and transport in conjugated-polymer/semiconductor-nanocrystal composites studied by photoluminescence quenching and photoconductivity, *Phys. Rev. B* 54, 17628 (1996).
96. E. Arici, N.S. Sariciftci, and D. Meissner, Hybrid Solar Cells Based on Nanoparticles of CuInS₂ in Organic Matrices, *Adv. Funct. Mater.* 13, 165 (2003).
97. P.A. van Hal, M.M. Wienk, J.M. Kroon, W.J.H. Verhees, L.H. Slooff, W.J.H. van Gennip, P. Jonkheijm, and R.A.J. Janssen, Photoinduced Electron Transfer and Photovoltaic Response of a MDMO-PPV:TiO₂ Bulk-Heterojunction, *Adv. Mater.* 15, 118 (2003).
98. M. Pientka, V. Dyakonov, D. Meissner, A. Rogach, D. Talapin, H. Weller, L. Lutsen, and D. Vanderzande, Photoinduced charge transfer in composites of conjugated polymers and semiconductor nanocrystals, *Nanotechnology* 15, 163 (2004).
99. E. Arici, H. Hoppe, F. Schäffler, D. Meissner, M.A. Malik, and N.S. Sariciftci, Hybrid Solar Cells based on inorganic nanoclusters and semiconductive polymers, *Thin Solid Films* 451-452, 612 (2004).
100. E. Arici, N.S. Sariciftci, and D. Meissner, in *Encyclopedia of Nanoscience and Nanotechnology*, edited by H. S. Nalwa (American Scientific Publishers, Stevenson Ranch, 2004).

101. H. Neugebauer, C. Brabec, J.C. Hummelen, and N.S. Sariciftci, Stability and photodegradation mechanisms of conjugated polymer/fullerene plastic solar cells, *Sol. Energy Mater. Sol. Cells* 61, 35 (2000).
102. F. Padinger, T. Fromherz, P. Denk, C.J. Brabec, J. Zettner, T. Hierl, and N.S. Sariciftci, Degradation of Bulk Heterojunction Solar Cells Operated in an Inert Gas Atmosphere: A Systematic Study, *Synth. Met.* 121, 1605 (2001).
103. C.W. Tang and A.C. Albrecht, Photovoltaic effects of metal-chlorophyll-a-metal sandwich cells, *J. Chem. Phys.* 62, 2139 (1975).
104. M. Hiramoto, Y. Kishigami, and M. Yokoyama, Doping Effect on the Two-layer Organic Solar Cell, *Chem. Lett.*, 119 (1990).
105. P.A. Lane, J. Rostalski, C. Giebeler, S.J. Martin, D.D.C. Bradley, and D. Meissner, Electroabsorption studies of phthalocyanine/perylene solar cells, *Sol. Energy Mater. Sol. Cells* 63, 3 (2000).
106. J. Rostalski and D. Meissner, Photocurrent spectroscopy for the investigation of charge carrier generation and transport mechanisms in organic p/n-junction solar cells, *Sol. Energy Mater. Sol. Cells* 63, 37 (2000).
107. M. Pfeiffer, A. Beyer, B. Plönnigs, A. Nollau, T. Fritz, K. Leo, D. Schlettwein, S. Hiller, and D. Wöhrle, Controlled p-doping of pigment layers by cosublimation: Basic mechanisms and implication for their use in organic photovoltaic cells, *Sol. Energy Mater. Sol. Cells* 63, 83 (2000).
108. D. Gebeyehu, B. Maennig, J. Drechsel, K. Leo, and M. Pfeiffer, Bulk-heterojunction photovoltaic devices based on donor-acceptor organic small molecule blends, *Sol. Energy Mater. Sol. Cells* 79, 81 (2003).
109. J. Drechsel, B. Männig, F. Kozlowski, D. Gebeyehu, A. Werner, M. Koch, K. Leo, and M. Pfeiffer, High efficiency organic solar cells based on single or multiple PIN structures, *Thin Solid Films* 451-452, 515 (2004).
110. M.S. Dresselhaus, G. Dresselhaus, and P.C. Eklund, *Science of Fullerenes and Carbon Nanotubes* (Academic Press, Inc., San Diego, 1996).
111. N.S. Sariciftci and A.J. Heeger, in *Handbook of Organic Conductive Molecules and Polymers; Vol. 1*, edited by H. S. Nalwa (John Wiley & Sons Ltd., Chichester, 1997), p. 413.
112. J.H. Burroughes, D.D.C. Bradley, A.R. Brown, R.N. Marks, K. Mackay, R.H. Friend, P.L. Burns, and A.B. Holmes, Light-emitting diodes based on conjugated polymers, *Nature* 347, 539 (1990).

113. D. Braun and A.J. Heeger, Visible light emission from semiconducting polymer diodes, *Appl. Phys. Lett.* 58, 1982 (1991).
114. *Organic Light-Emitting Devices: A Survey; Vol. 1*, edited by J. Shinar (Springer, New York, 2004).
115. D. Adam, P. Schuhmacher, J. Simmerer, L. Häussling, K. Siemensmeyer, K.H. Etzbachi, H. Ringsdorf, and D. Haarer, Fast photoconduction in the highly ordered columnar phase of a discotic liquid crystal, *Nature* 371, 141 (1994).
116. F. Garnier, G. Horowitz, D. Fichou, and A. Yassar, Molecular order in organic-based field-effect transistors, *Synth. Met.* 81, 163 (1996).
117. M. Funahashi and J.-i. Hanna, Fast Hole Transport in a New Calamitic Liquid Crystal of 2-(4'-Heptyloxyphenyl)-6-Dodecylthiobenzothiazole, *Phys. Rev. Lett.* 78, 2184 (1997).
118. H. Sirringhaus, P.J. Brown, R.H. Friend, M.M. Nielsen, K. Bechgaard, B.M.W. Langeveld-Voss, A.J.H. Spiering, R.A.J. Janssen, E.W. Meijer, P. Herwig, and D.M. de Leeuw, Two-dimensional charge transport in self-organized, high-mobility conjugated polymers, *Nature* 401, 685 (1999).
119. H. Sirringhaus, R.J. Wilson, R.H. Friend, M. Inbasekaran, W. Wu, E.P. Woo, M. Grell, and D.D.C. Bradley, Mobility enhancement in conjugated polymer field-effect transistors through chain alignment in a liquid-crystalline phase, *Appl. Phys. Lett.* 77, 406 (2000).
120. K.E. Aasmundtveit, E.J. Samuelsen, M. Guldstein, C. Steinsland, O. Flornes, C. Fagermo, T.M. Seeberg, L.A.A. Pettersson, O. Inganäs, R. Feidenhans, and S. Ferrer, Structural Anisotropy of Poly(alkylthiophene) Films, *Macromolecules* 33, 3120 (2000).
121. U. Zhokhavets, G. Gobsch, H. Hoppe, and N.S. Sariciftci, Anisotropic optical properties of thin poly(3-octylthiophene)-films as a function of preparation conditions, *Synth. Met.* 143, 113 (2004).
122. W. Geens, S.E. Shaheen, C.J. Brabec, J. Poortmans, and N.S. Sariciftci, "Field-effect mobility measurements of conjugated polymer/fullerene photovoltaic blends," presented at the Electronic Properties of Novel Materials - Molecular Nanostructures, 14th International Winterschool/Euroconference, Kirchberg, Austria, 2000 (American Institute of Physics).
123. T. Aernouts, P. Vanlaeke, W. Geens, J. Poortmans, P. Heremans, S. Borghs, and R. Mertens, "The Influence of the Donor/Acceptor Ratio on the Performance of organic Bulk Heterojunction Solar Cells," presented at the E-MRS spring meeting, Strasbourg, 2003.
124. S.A. Choulis, J. Nelson, Y. Kim, D. Poplavskyy, T. Kreouzis, J.R. Durrant, and D.D.C. Bradley, Investigation of transport properties in polymer/fullerene blends using time-of-flight photocurrent measurements, *Appl. Phys. Lett.* 83, 3812 (2003).

125. R. Pacios, J. Nelson, D.D.C. Bradley, and C.J. Brabec, Composition dependence of electron and hole transport in polyfluorene:[6,6]-phenyl C61-butyric acid methyl ester blend films, *Appl. Phys. Lett.* 83, 4764 (2003).
126. S.C. Veenstra, G.G. Malliaras, H.J. Brouwer, F.J. Esselink, V.V. Krasnikov, P.F. van Hutten, J. Wildeman, H.T. Jonkman, G.A. Sawatzky, and G. Hadziioannou, Sexithiophene-C60 blends as model systems for photovoltaic devices, *Synth. Met.* 84, 971 (1997).
127. T. Tsuzuki, Y. Shirota, J. Rostalski, and D. Meissner, The effect of fullerene doping on photoelectric conversion using titanyl phthalocyanine and a perylene pigment, *Sol. Energy Mater. Sol. Cells* 61, 1 (2000).
128. S.E. Shaheen, R. Radspinner, N. Peyghambarian, and G.E. Jabbour, Fabrication of bulk heterojunction plastic solar cells by screen printing, *Appl. Phys. Lett.* 79, 2996 (2001).
129. B.A. Gregg, Excitonic Solar Cells, *J. Phys. Chem. B* 107, 4688 (2003).
130. M. Pope and C.E. Swenberg, *Electronic processes in organic crystals and polymers*, 2. edition ed. (Oxford University Press, New York, 1999).
131. M. Murgia, F. Biscarini, M. Cavallini, C. Taliani, and G. Ruani, Intedigitated p-n junction: a route to improve the efficiency in organic photovoltaic cells, *Synth. Met.* 121, 1533 (2001).
132. G. Ruani, C. Fontanini, M. Murgia, and C. Taliani, Weak intrinsic charge transfer complexes: A new route for developing wide spectrum organic photovoltaic cells, *J. Chem. Phys.* 116, 1713 (2002).
133. T. Toccoli, A. Boschetti, C. Corradi, L. Guerini, M. Mazzola, and S. Iannotta, Co-deposition of phthalocyanines and fullerene by SuMBE; characterization and prototype devices, *Synth. Met.* 138, 3 (2003).
134. V.I. Arkhipov, P. Heremans, and H. Bässler, Why is exciton dissociation so efficient at the interface between a conjugated polymer and an electron acceptor?, *Appl. Phys. Lett.* 82, 4605 (2003).
135. G. Zerza, C.J. Brabec, G. Cerullo, S.D. Silvestri, and N.S. Sariciftci, Ultrafast charge transfer in conjugated polymer-fullerene composites, *Synth. Met.* 119, 637 (2001).
136. A.F. Nogueira, I. Montari, J. Nelson, J.R. Durrant, C. Winder, N.S. Sariciftci, and C. Brabec, Charge Recombination in Conjugated Polymer/Fullerene Blended Films Studied by Transient Absorption Spectroscopy, *J. Phys. Chem. B* 107, 1567 (2003).
137. A.J. Breeze, A. Salomon, D.S. Ginley, B.A. Gregg, H. Tillmann, and H.-H. Hörhold, Polymer-perylene diimide heterojunction solar cells, *Appl. Phys. Lett.* 81, 3085 (2002).

138. S.A. Jenekhe and S. Yi, Efficient photovoltaic cells from semiconducting polymer heterojunctions, *Appl. Phys. Lett.* 77, 2635 (2000).
139. T. Yohannes, F. Zhang, M. Svensson, J.C. Hummelen, M.R. Andersson, and O. Inganäs, Polyfluorene copolymer based bulk heterojunction solar cells, *Thin Solid Films* 449, 152 (2004).
140. E.A. Katz, D. Faiman, S.M. Tuladhar, J.M. Kroon, M.M. Wienk, T. Fromherz, F. Padinger, C.J. Brabec, and N.S. Sariciftci, Temperature dependence for the photovoltaic device parameters of polymer-fullerene solar cells under operating conditions, *J. Appl. Phys.* 90, 5343 (2001).
141. V. Dyakonov, The polymer-fullerene interpenetrating network: one route to a solar cell approach, *Physica E* 14, 53 (2002).
142. J.J. Dittmer, R. Lazzaroni, P. Leclere, P. Moretti, M. Granström, K. Petritsch, E.A. Marseglia, R.H. Friend, J.L. Bredas, H. Rost, and A.B. Holmes, Crystal network formation in organic solar cells, *Sol. Energy Mater. Sol. Cells* 61, 53 (2000).
143. J.J. Dittmer, E.A. Marseglia, and R.H. Friend, Electron Trapping in Dye/Polymer Blend Photovoltaic Cells, *Adv. Mater.* 12, 1270 (2000).
144. K. Petritsch, J.J. Dittmer, E.A. Marseglia, R.H. Friend, A. Lux, G.G. Rozenberg, S.C. Moratti, and A.B. Holmes, Dye-based donor/acceptor solar cells, *Sol. Energy Mater. Sol. Cells* 61, 63 (2000).
145. L. Schmidt-Mende, A. Fechtenkötter, K. Müllen, E. Moons, R.H. Friend, and J.D. MacKenzie, Self-Organized Discotic Liquid Crystals for High-Efficiency Organic Photovoltaics, *Science* 293, 1119 (2001).
146. L. Chen, D. Godovsky, O. Inganäs, J.C. Hummelen, R.A.J. Janssens, M. Svensson, and M.R. Andersson, Polymer Photovoltaic Devices from Stratified Multilayers of Donor-Acceptor Blends, *Adv. Mater.* 12, 1367 (2000).
147. C.J. Brabec, A. Cravino, D. Meissner, N.S. Sariciftci, M.T. Rispens, L. Sanchez, J.C. Hummelen, and T. Fromherz, The influence of materials work function on the open circuit voltage of plastic solar cells, *Thin Solid Films* 403-404, 368 (2002).
148. M. Drees, K. Premaratne, W. Graupner, J.R. Heflin, R.M. Davis, D. Marciu, and M. Miller, Creation of a gradient polymer-fullerene interface in photovoltaic devices by thermally controlled interdiffusion, *Appl. Phys. Lett.* 81, 1 (2002).
149. A.W. Snow and W.R. Barger, in *Phthalocyanines: Properties and Applications*, edited by C. C. Leznoff and B. B. Lever (Wiley VCH, New York, 1989).

150. K.N. Baker, A.V. Fratini, T. Resch, H.C. Knachel, W.W. Adams, E.P. Socci, and B.L. Farmer, Crystal structures, phase transitions and energy calculations of poly(p-phenylene) oligomers, *Polymer* 34, 1571 (1993).
151. *Handbook of Oligo- and Polythiophenes; Vol.* , edited by D. Fichou (Wiley VCH, Weinheim, 1999).
152. N. Karl and C. Günter, Structure and Ordering Principles of Ultrathin Organic Molecular Films on Surfaces of Layered Semiconductors. *Organic on Inorganic MBE, Cryst. Res. Technol.* 34, 243 (1999).
153. D.E. Hooks, T. Fritz, and M.D. Ward, Epitaxy and Molecular Organization on Solid Substrates, *Adv. Mater.* 13, 227 (2001).
154. A. Andreev, G. Matt, C.J. Brabec, H. Sitter, D. Badt, H. Seyringer, and N.S. Sariciftci, Highly Anisotropically Self-Assembled Structures of para-Sexiphenyl Grown by Hot Wall Epitaxy, *Adv. Mater.* 12, 629 (2000).
155. H. Plank, R. Resel, S. Purger, J. Keckes, A. Thierry, B. Lotz, A. Andreev, N.S. Sariciftci, and H. Sitter, Heteroepitaxial growth of self-assembled highly ordered para-sexiphenyl films: A crystallographic study, *Phys. Rev. B* 64, 235423 (2001).
156. R. Resel, N. Koch, F. Meghdadi, G. Leising, W. Unzog, and K. Reichmann, Growth and preferred crystallographic orientation of hexaphenyl thin films, *Thin Solid Films* 305, 232 (1997).
157. A. Ulman, *An introduction to ultrathin organic films: from Langmuir-Blodgett to self-assembly* (Academic Press, Boston, 1991).
158. B. Romagnoli and W. Hayes, Chiral dendrimers—from architecturally interesting hyperbranched macromolecules to functional materials, *J. Mater. Chem.* 12, 767 (2002).
159. H. Ma, S. Liu, J. Luo, S. Suresh, L. Liu, S.H. Kang, M. Haller, T. Sassa, L.R. Dalton, and A.K.-Y. Jen, Highly Efficient and Thermally Stable Electro-Optical Dendrimers for Photonics, *Adv. Funct. Mater.* 12, 565 (2002).
160. T. Hasobe, Y. Kashiwagi, M.A. Absalom, J. Sly, K. Hosomizu, M.J. Crossley, H. Imahori, P.V. Kamat, and S. Fukuzumi, Supramolecular Photovoltaic Cells Using Porphyrin Dendrimers and Fullerene, *Adv. Mater.* 16, 975 (2004).
161. M. Kemerink, J.K.J. van Duren, P. Jonkheijm, W.F. Pasveer, P.M. Koenraad, R.A.J. Janssen, H.W.M. Salemink, and J.H. Wolter, Relating Substitution to Single-Chain Conformation and Aggregation in Poly(p-phenylene Vinylene) Films, *Nano Lett.* 3, 1191 (2003).
162. P.J. Flory, *Principles of Polymer Chemistry* (Cornell University Press, Ithaca, 1953).

163. P.G. de Gennes, *Scaling Concepts in Polymer Physics* (Cornell University Press, Ithaca, 1979).
164. M. Doi, *Introduction to Polymer Physics* (Clarendon Press, Oxford, 1996).
165. T.-Q. Nguyen, V. Doan, and B.J. Schwartz, Conjugated polymer aggregates in solution: Control of interchain interactions, *J. Chem. Phys.* 110, 4068 (1999).
166. T.-Q. Nguyen, I.B. Martini, J. Liu, and B.J. Schwartz, Controlling Interchain Interactions in Conjugated Polymers: The Effects of Chain Morphology on Exciton-Exciton Annihilation and Aggregation in MEH-PPV Films, *J. Phys. Chem. B* 104, 237 (2000).
167. T.-Q. Nguyen, R.C. Kwong, M.E. Thompson, and B.J. Schwartz, Improving the performance of conjugated polymer-based devices by control of interchain interactions and polymer film morphology, *Appl. Phys. Lett.* 76, 2454 (2000).
168. Y. Shi, J. Liu, and Y. Yang, Device performance and polymer morphology in polymer light emitting diodes: The control of thin film morphology and device quantum efficiency, *J. Appl. Phys.* 87, 4254 (2000).
169. K.E. Aasmundtveit, E.J. Samuelsen, K. Hoffmann, E. Bakken, and P.H.J. Carlsen, Structural studies of polyalkylthiophenes with alternating sidechain positioning, *Synth. Met.* 113, 7 (2000).
170. F.C. Krebs, S.V. Hoffmannb, and M. Jørgensena, Orientation effects in self-organized, highly conducting regioregular poly(3-hexylthiophene) determined by vacuum ultraviolet spectroscopy, *Synth. Met.* 138, 471 (2002).
171. A. Salleo, M.L. Chabinyc, M.S. Yang, and R.A. Street, Polymer thin-film transistors with chemically modified dielectric interfaces, *Appl. Phys. Lett.* 81, 4383 (2002).
172. R.J.O.M. Hoofman, M.P. de Haas, L.D.A. Siebbeles, and J.M. Warman, Highly mobile electrons and holes on isolated chains of the semiconducting polymer poly(phenylene vinylene), *Nature* 392, 54 (1998).
173. K.R. Amundson, B.J. Sapjeta, A.J. Lovinger, and Z. Bao, An in-plane anisotropic organic semiconductor based upon poly(3-hexyl thiophene), *Thin Solid Films* 414, 143 (2002).
174. L. Kinder, J. Kanicki, and P. Petroff, Structural ordering and enhanced carrier mobility in organic polymer thin film transistors, *Synth. Met.* 146, 181 (2004).
175. H. Hoppe, M. Heuberger, and J. Klein, Self-Similarity and Pattern Selection in the Roughening of Binary Liquid Films, *Physical Review Letters* 86, 4863 (2001).
176. E. Moons, Conjugated polymer blends: linking film morphology to performance of light emitting diodes and photodiodes, *J. Phys.: Condens. Matter* 14, 12235–12260 (2002).

177. F. Wudl, P.-M. Allemand, G. Srdanov, Z. Ni, and D. McBranch, in *Materials for Nonlinear Optics: Chemical Perspectives*, edited by S. R. Marder, J. E. Sohn, and G. D. Stucky (American Chemical Society, Washington, DC, 1991), p. 683.
178. J. Gao, F. Hide, and H. Wang, Efficient photodetectors and photovoltaic cells from composites of fullerenes and conjugated polymers: photoinduced electron transfer, *Synth. Met.* 84, 979 (1997).
179. D. Gebeyehu, C.J. Brabec, F. Padinger, T. Fromherz, J.C. Hummelen, D. Badt, H. Schindler, and N.S. Sariciftci, The interplay of efficiency and morphology in photovoltaic devices based on interpenetrating networks of conjugated polymers with fullerenes, *Synth. Met.* 118, 1 (2001).
180. N. Camaioni, M. Catellani, S. Luzzati, and A. Migliori, Morphological characterization of poly(3-octylthiophene):plasticizer:C60 blends, *Thin Solid Films* 403-404, 489 (2002).
181. M.T. Rispens, A. Meetsma, R. Rittberger, C.J. Brabec, N.S. Sariciftci, and J.C. Hummelen, Influence of the solvent on the crystal structure of PCBM and the efficiency of MDMO-PPV:PCBM 'plastic' solar cells, *Chem. Commun.* 17, 2116 (2003).
182. T. Martens, J. D'Haen, T. Munters, L. Goris, Z. Beelen, J. Manca, M. D'Olieslaeger, D. Vanderzande, L.D. Schepper, and R. Andriessen, "The influence of the microstructure upon the photovoltaic performance of MDMOPPV:PCBM bulk hetero-junction organic solar cells," presented at the MRS Spring Meeting, San Francisco, 2002 (Materials Research Society), p. P7.11.1.
183. T. Martens, Z. Beelen, J. D'Haen, T. Munters, L. Goris, J. Manca, M. D'Olieslaeger, D. Vanderzande, L.D. Schepper, and R. Andriessen, "Morphology of MDMO-PPV:PCBM bulk hetero-junction organic solar cells studied by AFM, KFM and TEM," presented at the Proceedings of the SPIE The International Society for Optical Engineering, San Diego, CA, 2003 (SPIE The International Society for Optical Engineering), p. 40.
184. T. Martens, J. D'Haen, T. Munters, Z. Beelen, L. Goris, J. Manca, M. D'Olieslaeger, D. Vanderzande, L.D. Schepper, and R. Andriessen, Disclosure of the nanostructure of MDMO-PPV:PCBM bulk heterojunction organic solar cells by a combination of SPM and TEM, *Synth. Met.* 138, 243 (2003).
185. X. Yang, J.K.J. van Duren, M.T. Rispens, J.C. Hummelen, R.A.J. Janssen, M.A.J. Michels, and J. Loos, Crystalline Organization of a Methanofullerene as Used for Plastic Solar-Cell Applications, *Adv. Mater.* 16, 802 (2004).

186. X. Yang, J.K.J. van Duren, R.A.J. Janssen, M.A.J. Michels, and J. Loos, Morphology and Thermal Stability of the Active Layer in Poly(*p*-phenylenevinylene)/Methanofullerene Plastic Photovoltaic Devices, *Macromolecules* 37, 2151 (2004).
187. J.K.J. van Duren, X. Yang, J. Loos, C.W.T. Bulle-Lieuwma, A.B. Sieval, J.C. Hummelen, and R.A.J. Janssen, Relating the Morphology of Poly(*p*-phenylene vinylene)/Methanofullerene Blends to Solar-Cell Performance, *Adv. Funct. Mater.* 14, 425 (2004).
188. H. Becker, (Frankfurt, Germany, 2004).
189. G. Binnig, C. F. Quate, and C. Gerber, Atomic Force Microscope, *Phys. Rev. Lett.* 56, 930 (1986).
190. G. Binnig and H. Rohrer, , *Helvetica Physica Acta* 55, 726 (1982).
191. G. Binnig, H. Rohrer, C. Gerber, and E. Weibel, Tunneling through a controllable vacuum gap, *Appl. Phys. Lett.* 40, 178 (1982).
192. G. Binnig, H. Rohrer, C. Gerber, and E. Weibel, Surface Studies by Scanning Tunneling Microscopy, *Phys. Rev. Lett.* 49, 57 (1982).
193. M. Knoll and E. Ruska, Das Elektronenmikroskop, *Zeitschrift für Physik* 78, 318 (1932).
194. C. Sommerhalter, T.W. Matthes, T. Glatzel, A. Jäger-Waldau, and M.C. Lux-Steiner, High-sensitivity quantitative Kelvin probe microscopy by noncontact ultra-high-vacuum atomic force microscopy, *Appl. Phys. Lett.* 75, 286 (1999).
195. C. Sommerhalter, T. Glatzel, T.W. Matthes, A. Jäger-Waldau, and M.C. Lux-Steiner, Kelvin probe force microscopy in ultra high vacuum using amplitude modulation detection of the electrostatic forces, *Appl. Surf. Sci.* 157, 263 (2000).
196. C. Sommerhalter, S. Sadewasser, T. Glatzel, T.W. Matthes, A. Jäger-Waldau, and M.C. Lux-Steiner, Kelvin probe force microscopy for the characterization of semiconductor surfaces in chalcopyrite solar cells, *Surface Science* 482-485, 1362 (2001).
197. A. Kikukawa, S. Hosaka, and R. Imura, Vacuum compatible high-sensitive Kelvin probe force microscopy, *Review of Scientific Instruments* 67, 1463 (1996).
198. F.J. Giessibl, Forces and frequency shifts in atomic-resolution dynamic-force microscopy, *Phys. Rev. B* 54, 16010 (1997).
199. T. Glatzel, Dissertation Thesis, Freie Universität Berlin, 2003.
200. Y. Martin, D.W. Abraham, and H.K. Wickramasinghe, High-resolution capacitance measurement and potentiometry by force microscopy, *Appl. Phys. Lett.* 52, 1103 (1988).

201. A. Kikukawa, S. Hosaka, and R. Imura, Silicon *pn* junction imaging and characterizations using sensitivity enhanced Kelvin probe force microscopy, *Appl. Phys. Lett.* 66, 3510 (1995).
202. C. Sommerhalter, Dissertation Thesis, Freie Universität Berlin, 1999.
203. T. Glatzel, S. Sadewasser, and M.C. Lux-Steiner, Amplitude or frequency modulation-detection in Kelvin probe force microscopy, *Appl. Surf. Sci.* 210, 84 (2003).
204. B. Wessling, Progress in Science and Technology of Polyaniline and Polyethylenedioxythiophene, *Synth. Met.* 135-136, 265 (2003).
205. P.A. Heiney, J.E. Fischer, A.R. McGhie, W.J. Romanow, A.M. Denenstien, J.P. McCauley Jr., A.B. Smith, and D.E. Cox, Orientational ordering transition in solid C₆₀, *Phys. Rev. Lett.* 66, 2911 (1991).
206. H. Hoppe, N. Arnold, D. Meissner, and N.S. Sariciftci, Modelling the optical absorption within conjugated polymer/fullerene-based bulk-heterojunction organic solar cells, *Sol. Energy Mater. Sol. Cells* 80, 105 (2003).
207. C.W.T. Bulle-Lieuwma, W.J.H. van Gennip, J.K.J. van Duren, P. Jonkheijm, R.A.J. Janssen, and J.W. Niemantsverdriet, Characterization of polymer solar cells by TOF-SIMS depth profiling, *Appl. Surf. Sci.* 203-204, 547 (2003).
208. V.D. Mihailetschi, J.K.J. van Duren, P.W.M. Bloom, J.C. Hummelen, R.A.J. Janssen, J.M. Kroon, M.T. Rispens, W.J.H. Verhees, and M.M. Wienk, Electron Transport in a Methanofullerene, *Adv. Funct. Mater.* 13, 43 (2003).
209. C. Waldauf, P. Schilinsky, M. Perisutti, J. Hauch, and C.J. Brabec, Solution-Processed Organic n-Type Thin-Film Transistors, *Adv. Mater.* 15, 2084 (2003).
210. G.J. Matt, N.S. Sariciftci, and T. Fromherz, Anomalous charge transport behavior of Fullerene based diodes, *Appl. Phys. Lett.* 84, 1570 (2004).
211. R. Kersting, U. Lemmer, R.F. Mahrt, K. Leo, H. Kurz, H. Bässler, and E.O. Göbel, Femtosecond energy relaxation in *pi*-conjugated polymers, *Phys. Rev. Lett.* 70, 3820–3823 (1993).

Eidesstattliche Erklärung

Ich erkläre an Eides statt, dass ich die vorliegende Dissertation selbstständig und ohne fremde Hilfe verfasst, andere als die angegebenen Quellen und Hilfsmittel nicht benutzt bzw. die wörtlich oder sinngemäß entnommenen Stellen als solche kenntlich gemacht habe.

7. Acknowledgements

This work would not have been possible without the help and support of many persons, therefore I would like to thank:

– my supervisor Niyazi Serdar Sariciftci, it was a great honor and pleasure to work with him and in his group. He gave me many opportunities to explore the scientific world around plastic solar cells. I enjoyed a lot the scientific freedom that he provided, and that I was never without his good advice and encouragement.

– Dieter Meissner especially for his stimulating impact on my optical modeling studies.
– Helmut Neugebauer especially for the valuable scientific discussions and advices.

– all the present and former members of LIOS:

Andrei Andreev, Assefa S. Asemahegne, Elif Arici, Eugen Baumgartner, Elke Bradt, Antonio Cravino, Gilles Dennler, Martin Drees, Bernd Ebner, Martin Egginger, Anita Fuchsbauer, Serap Günes, Alexander Gusenbauer, Sandra Hofer, Robert Koeppel, Christopher Kopecny, Manfred Lipp, Maria Antonietta Loi, Christoph Lungenschmied, Nenad Marjanovic, Gebhard Matt, Farideh Meghdadi, Attila Mozer, Petra Neumaier, LeHuong Nguyen, Franz Padinger, Birgit Paulik, Gabriele Prager, Birendra Singh, Daniela Stoenescu, Teketel Yohannes, Christoph Winder, Gerald Zerza.

– all present and former members of Konarka Austria (formerly QSEL):

Christoph Brabec, Patrick Denk, Markus Koppe, David Mühlbacher, Roman Rittberger, Markus Scharber, Christoph Topf, Christoph Waldauff, Elisabeth Wirtl– my coworkers for the fruitful collaborations:

Nikita Arnold, Jens Drechsel, Daniel A. M. Egbe, Thilo Glatzel, Gerhard Gobsch, Renate Hiesgen, Andreas Hinsch, Jürgen Kraut, Karl Leo, Martha Ch. Lux-Steiner, Bert Männig, Michael Niggemann, Martin Pfeiffer, W. Schwinger, F. Schaeffler, Helmut Sitter, Uladzimir Zhokhavets

– my parents and my sister for their faithfulness in any kind of support and help.

– my friends, brothers and sisters for their fellowship and prayers.

– my Lord Jesus, who carried me through. Him be the honor and glory alone!

8. Appendix

8.1. Curriculum Vitae

Harald Hoppe

Nationality

28th of September 1973

German

Born in Rotenburg, Germany

January 2001 – November 2004

PhD studies in Physics at the Johannes Kepler University Linz, Physical Chemistry

May 1999 – August 2000

Diploma studies at the Weizmann Institute of Science, Rehovot, Israel
Title: “Thermodynamics of binary polymer blends in thin films via depth-profiling using Nuclear Reaction Analysis”

Oktober 1994 – August 2000

Studies in Physics at the University of Konstanz, Germany
Degree: Diplom Physiker

July 1993 – June 1994

Military service

May 1993

Graduated at comprehensive secondary school Eichenschule Scheeßel, Germany

Practicals:

1998

Silicon solar cells, Prof. Bucher, University of Konstanz, Germany

1997

Cavity ring down spectroscopy, Prof. Hogervorst
Frije Universiteit Amsterdam, Holland
Characterization of linear oscillators from high- T_C superconductors, Bosch, Stuttgart, Germany

8.2. List of Publications

8.2.1. Conference Proceedings

1. H. Hoppe, M. Niggemann, C. Winder, M. Drees, W. Schwinger, F. Schaeffler, A. Hinsch, D. Meissner, and N.S. Sariciftci, "Nanoscale morphology and its effects on efficiency of conjugated polymer/fullerene based bulk-heterojunction solar cells," presented at the Technologies for Polymer Electronics TPE 04, Rudolstadt, Germany, 2004 (TITK), p. 51.
2. H. Hoppe, M. Drees, W. Schwinger, F. Schäffler, and N.S. Sariciftci, "Nano-Crystalline Fullerene Phases in Polymer/Fullerene Bulk-Heterojunction Solar Cells: A Transmission Electron Microscopy Study," presented at the ICSM, Wollongong, Australia, 2004 (Synthetic Metals), p. submitted.
3. H. Hoppe, D.A.M. Egbe, D. Mühlbacher, M. Koppe, and N.S. Sariciftci, "Plastic Solar Cells based on novel PPE-PPV-copolymers," presented at the ICEPOM-5, Kiev, 2004 (Molecular Crystals & Liquid Crystals), p. submitted.
4. U. Zhokhavets, G. Gobsch, H. Hoppe, and N.S. Sariciftci, A systematic study of the anisotropic optical properties of thin poly(3-octylthiophene)-films in dependence on growth parameters, *Thin Solid Films* 451-452, 69 (2004).
5. E. Arici, H. Hoppe, F. Schäffler, D. Meissner, M.A. Malik, and N.S. Sariciftci, Hybrid Solar Cells based on inorganic nanoclusters and semiconductive polymers, *Thin Solid Films* 451-452, 612 (2004).
6. H. Hoppe, N. Arnold, D. Meissner, and N.S. Sariciftci, Modeling of optical absorption in conjugated polymer / fullerene bulk-heterojunction plastic solar cells, *Thin Solid Films* 451-452, 589 (2004).
7. A. Andreev, R. Resel, D.-M. Smilgies, H. Hoppe, G. Matt, H. Sitter, N.S. Sariciftci, D. Meissner, H. Plank, and O. Zrzavecka, Oriented organic semiconductor thin films, *Synth. Met.* 138, 59 (2003).
8. M. Loi, P. Denk, H. Hoppe, H. Neugebauer, D. Meissner, C. Winder, C. Brabec, N.S. Sariciftci, A. Gouloumis, P. Vazquez, and T. Torres, A Fulleropyrrolidine-phthalocyanine dyad for photovoltaic applications, *Synth. Met.* 137, 1491 (2003).
9. H. Hoppe, N.S. Sariciftci, and D. Meissner, Optical constants of conjugated polymer/fullerene based bulk-heterojunction organic solar cells, *Molecular Crystals & Liquid Crystals* 385, 113 (2002).
10. A. Andreev, R. Resel, D.-M. Smilgies, H. Hoppe, G. Matt, H. Sitter, N.S. Sariciftci, D. Meissner, D. Lysacek, and L. Valek, Highly aligned organic semiconductor thin films grown by hot wall epitaxy, *Molecular Crystals & Liquid Crystals* 385, 61 (2002).
11. E. Arici, H. Hoppe, A. Reuning, N.S. Sariciftci, and D. Meissner, CIS Plastic Solar Cells, 17th European Photovoltaic Solar Energy Conference Proceedings, 61 (2002).
12. M. Niggemann, B. Bläsi, A. Gombert, A. Hinsch, H. Hoppe, P. Lalanne, D. Meissner, and V. Wittwer, "Trapping Light in Organic Plastic Solar Cells with integrated Diffraction Gratings," presented at the Proceedings of 17th European Photovoltaic Solar Energy Conference, Munich, 2002.

8.2.2. Articles

1. H. Hoppe and N.S. Sariciftci, in *Organic Photovoltaics*, edited by S.-S. Sun and N.S. Sariciftci (2005), p. 217.
2. H. Hoppe, T. Glatzel, M. Niggemann, M.C. Lux-Steiner, and N.S. Sariciftci, Kelvin Probe Force Microscopy Study on Conjugated Polymer/Fullerene Bulk Heterojunction Organic Solar Cells, in preparation (2004).
3. M. Drees, H. Hoppe, C. Winder, H. Neugebauer, N.S. Sariciftci, W. Schwinger, F. Schäffler, C. Topf, M.C. Scharber, Z. Zhu, and R. Gaudiana, Stabilization of the nanomorphology of polymer/fullerene "bulk heterojunction" blends using a novel polymerizable fullerene derivative, *Adv. Funct. Mater.* submitted (2004).
4. J. Drechsel, B. Männig, F. Kozlowski, M. Pfeiffer, K. Leo, and H. Hoppe, Efficient organic solar cells based on a multiple p-i-n architecture using doped wide-gap transport layers, *Appl. Phys. Lett.* submitted (2004).
5. H. Hoppe, D.A.M. Egbe, D. Mühlbacher, and N.S. Sariciftci, Photovoltaic action of conjugated polymer/fullerene bulk heterojunction solar cells using novel PPE-PPV-copolymers, *J. Mater. Chem.*, in print (2004).
6. H. Hoppe, M. Niggemann, C. Winder, J. Kraut, R. Hiesgen, A. Hinsch, D. Meissner, and N.S. Sariciftci, Nanoscale morphology of conjugated polymer/fullerene based bulk-heterojunction solar cells, *Adv. Funct. Mater.* 14, 1005 (2004).
7. A. Andreev, F. Quochi, A. Kadashchuk, H. Sitter, C. Winder, H. Hoppe, N.S. Sariciftci, A. Mura, and G. Bongiovanni, Blue emitting self-assembled nano-fibers of para-sexiphenyl grown by hot wall epitaxy, *physica status solidi (a)* 201, 2288 (2004).
8. E. Arici, H. Hoppe, F. Schäffler, D. Meissner, M.A. Malik, and N.S. Sariciftci, Morphology effects in nanocrystalline CuInSe₂-conjugated polymer hybrid systems, *Appl. Phys. A* 79, 59 (2004).
9. B. Maennig, J. Drechsel, D. Gebeyehu, P. Simon, F. Kozlowski, A. Werner, F. Li, S. Grundmann, S. Sonntag, M. Koch, K. Leo, M. Pfeiffer, H. Hoppe, D. Meissner, N.S. Sariciftci, I. Riedel, V. Dyakonov, and J. Parisi, Organic p-i-n solar cells, *Appl. Phys. A* 79, 1 (2004).
10. H. Hoppe and N.S. Sariciftci, Organic solar cells: an overview, *J. Mater. Res.* 19, 1924 (2004).
11. A. Andreev, C. Teichert, G. Hlawacek, H. Hoppe, R. Resel, D.-M. Smilgies, H. Sitter, and N.S. Sariciftci, Morphology and growth kinetics of organic thin films deposited by hot wall epitaxy, *Org. Electron.* 5, 23 (2004).
12. U. Zhokhavets, G. Gobsch, H. Hoppe, and N.S. Sariciftci, Anisotropic optical properties of thin poly(3-octylthiophene)-films as a function of preparation conditions, *Synth. Met.* 143, 113 (2004).
13. J. Drechsel, B. Maennig, D. Gebeyehu, M. Pfeiffer, K. Leo, and H. Hoppe, MIP-type organic solar cells incorporating phthalocyanine/fullerene mixed layers and doped wide-gap transport layers, *Org. Electron.* 5, 175 (2004).
14. H. Hoppe, N. Arnold, D. Meissner, and N.S. Sariciftci, Modelling the optical absorption within conjugated polymer/fullerene-based bulk-heterojunction organic solar cells, *Sol. Energy Mater. Sol. Cells* 80, 105 (2003).
15. M.A. Loi, P. Denk, H. Hoppe, H. Neugebauer, C. Winder, D. Meissner, C. Brabec, N.S. Sariciftci, A. Gouloumis, P. Vazquez, and T. Torres, Long-lived photoinduced charge separation for solar cell applications in phthalocyanine-fulleropyrrolidine dyad thin films, *J. Mater. Chem.* 13, 700 (2003).
16. H. Hoppe, M. Heuberger, and J. Klein, Self-Similarity and Pattern Selection in the Roughening of Binary Liquid Films, *Physical Review Letters* 86, 4863 (2001).